

Subwavelength Metallic Structures for Sensing: Modeling & Characterization

THÈSE N° 5328 (2012)

PRÉSENTÉE LE 25 AVRIL 2012

À LA FACULTÉ DES SCIENCES ET TECHNIQUES DE L'INGÉNIEUR

INSTITUT DE MICROTECHNIQUE

PROGRAMME DOCTORAL EN PHOTONIQUE

ÉCOLE POLYTECHNIQUE FÉDÉRALE DE LAUSANNE

POUR L'OBTENTION DU GRADE DE DOCTEUR ÈS SCIENCES

PAR

Qing TAN

acceptée sur proposition du jury:

Prof. P.-A. Farine, président du jury

Prof. H. P. Herzig, directeur de thèse

Prof. O. Martin, rapporteur

Dr E. Murphy, rapporteur

Prof. W. Nakagawa, rapporteur



ÉCOLE POLYTECHNIQUE
FÉDÉRALE DE LAUSANNE

Suisse
2012

Résumé

Les capteurs optiques basés sur la mesure de l'indice de réfraction sont des outils importants pour le contrôle et l'analyse directe des propriétés physico-chimiques de substances. Parmi différents dispositifs développés pour la mesure de l'indice de réfraction, les systèmes plasmoniques intégrant des nanostructures métalliques sont particulièrement prometteurs. Celles-ci possèdent un intérêt particulier de par leur aptitude à confiner et exalter le champ électromagnétique dans des volumes très faibles, bien inférieurs à ceux imposés par la limite de diffraction. De plus, ces structures offrent la possibilité de miniaturiser les systèmes actuels et de multiplexer les capteurs sur un même substrat.

Cette thèse est dédiée à l'exploration de capteurs combinant nano-cavités métalliques et guides d'ondes diélectriques. Structurations périodiques de couches minces d'or ont été étudiées pour mesurer localement des variations d'indice de réfraction. Deux structures sont ici considérées : les Slot Waveguide Cavity (SWC) et les Annular Aperture Array (AAA).

Le SWC est un réseau périodique de fentes réalisé sur un film d'or, étant déposé sur un guide d'onde en silicium. Le couplage évanescent entre le mode résonant des fentes métalliques et la structure guidante résulte en une profonde modification du spectre de transmission du guide d'onde. L'étude théorique, la fabrication ainsi que la caractérisation ont été effectuées dans le but de déterminer et vérifier la sensibilité de ces nanostructures aux variations d'indice de réfraction. Les dimensions de la cavité sont de 30 nm pour la largeur des fentes, 700 nm pour la longueur et 20 nm pour l'épaisseur. Une sensibilité de 730 ± 10 nm/RIU (Refractive Index Unit - Unité de l'Indice de Réfraction) a été mesurée expérimentalement, ce qui confirme les prédictions théoriques. La résolution théorique du capteur a par ailleurs été estimée à 5.8×10^{-5} RIU.

Dans le cas de la seconde structure, le AAA est implanté dans un guide d'onde en nitrure de silicium. Une résonance Fabry-Pérot provoque une variation de la réponse spectrale, que nous observons dans ce cas en réflexion. La forte localisation du champ dans la cavité rend la structure AAA particulièrement adapté à la mesure de variation d'indice de réfraction. Dans le

cas des liquides, une sensibilité de 764 nm/RIU a été théoriquement prévue, pour des longueurs d'ondes appartenant au proche infrarouge.

Bien que ces deux structures possèdent une sensibilité à l'indice de réfraction comparable à celle d'autres capteurs optiques basés sur des effets résonants, elles offrent plusieurs avantages. D'une part, les cavités métalliques, dont le volume d'interaction est de l'ordre de grandeur du femtolitre, permettent une détection locale à l'échelle de nanomètre. De plus, leur architecture planaire facilite leur intégration avec d'autres dispositifs photoniques. Des mesures parallèles incluant plusieurs capteurs sur le même substrat sont de ce fait prévues pour l'élaboration d'un système de détection miniature et low-cost.

Mots-clés:

capteur optique; capteur à indice de réfraction; nanostructure métalliques; modélisation; caractérisation; résonance Fabry-Pérot; Finite Difference Time Domain (FDTD); cavité

Abstract

Following rapid developments in biotechnology and medicine, optical sensing promises to be extremely important in various applications such as drug discovery, environmental monitoring, *etc.* Refractive index (RI) based optical sensing is straightforward to monitor or analyze the physical and chemical properties of substances. Among diverse configurations developed for RI detection, plasmonics devices using nanoscale patterned metals are particularly promising. Nano-structured metallic devices enable field confinement in a volume smaller than the diffraction limit. Moreover, they present possibilities for device miniaturization and sensor multiplexing on the same substrate.

This thesis is dedicated to investigating a sensing platform combining nano-structured metallic cavities and dielectric waveguides. Periodically structured Au films have been explored for their application in local RI sensing. Two structures are considered: the slot waveguide cavity (SWC) and the annular aperture array (AAA).

The SWC is composed of a Au film structured by a periodic slot array, which is deposited on a silicon (Si) waveguide. The evanescent field overlap correlates the resonant optical response of the cavity to the transmission spectrum of the Si waveguide. Theoretical studies, fabrication and characterization have been performed to verify the RI sensing ability for extremely subwavelength slot dimensions (30 nm slot width for 20 nm-thick Au film and 700 nm cavity length). The experimental sensitivity, 730 ± 10 nm/RIU, corresponds to the theory and an optimum resolution of 5.8×10^{-5} RIU is anticipated for RI detection.

For the AAA device, the patterned Au film is directly embedded in a Si_3N_4 waveguide. The Fabry-Pérot-like resonance of the Au cavity results in a resonant reflection, enabling a device sensitive to RI variations. For a wide range of analytes, the theoretical sensitivity is 764 nm/RIU in the near-infrared wavelength range.

Compared with other resonance based photonic sensors, the two devices exhibit comparable sensitivities to the RI variation. The small metallic

cavity implies a local detection on nano scale and the sample volume can be on the order of a femtolitre. Furthermore, the planar configuration permits easy integration with other photonic devices. Parallel sensing using compatible sensors on the same substrate is anticipated for the realization of portable and low-cost sensor systems.

Keywords:

optical sensor; refractive index based sensor; lab-on-a-chip sensing; metallic nanostructure; modeling; characterization; Fabry-Pérot resonance; finite difference time domain (FDTD); cavity

Contents

1	Introduction	1
2	State of art	5
2.1	Optical Sensors	5
2.1.1	Sensor characteristic	6
2.1.2	Sensitivity and resolution	9
2.1.3	Optical refractive index sensors	11
2.1.3.1	SPR and SPR-like sensors	12
2.1.3.2	Optical fiber based sensors	16
2.1.3.3	Ring resonator based sensors	19
2.1.3.4	Interferometer based sensors	20
2.1.3.5	Photonic crystal sensors	22
2.1.4	Optical biosensors	22
2.1.5	To nanostructure based sensors	24
2.2	Simulation Tools	25
2.2.1	Rigorous coupled wave analysis (RCWA)	26
2.2.2	Finite difference time domain (FDTD) method	28
3	Slot Waveguide Cavity	31
3.1	Introduction	31
3.2	Design & Principle	32
3.2.1	Spectrum analysis	34
3.2.2	Quantitative FP analysis	36
3.3	Parameters Study	43
3.3.1	Slot width w & Au thickness h	44
3.3.2	Cavity length l	47
3.3.3	Period p	49
3.3.4	Waveguide	49
3.3.5	Summary	54
3.3.6	Discussion of the finite structure	55

CONTENTS

3.4	Fabrication	57
3.5	Characterization and Results	58
3.5.1	Set-up	58
3.5.2	Results	60
3.6	Sensing Application	60
3.6.1	Theoretical expectation	62
3.6.2	Experiments	64
3.6.3	Performance evaluation	67
3.6.4	Discussions	70
3.7	Conclusion	71
4	Annular Aperture Array	73
4.1	Introduction	73
4.2	Design & Principle	74
4.3	Parameters Study	81
4.3.1	Periodicity	81
4.3.2	Radii difference	85
4.3.3	Radii sum	86
4.3.4	Cut distance	86
4.3.5	Summary	87
4.4	Sensing	89
4.5	3D Simulation for Fabrication Consideration	89
4.6	Conclusion	94
5	Conclusion	95
A	Standard deviation of amplitude noise	99
B	Drude model verification	101
	Bibliography	103

Chapter 1

Introduction

Optical sensors employ light to convert certain physical or chemical properties into optical signals. The light-matter interaction is the basis of this information conversion. Fundamentally, when light propagates through a sensor, a part or the whole amount of light penetrates into the sample and interacts with the analyte. Compared with the electrical or mechanical counterpart, optical sensors exhibit advantages like non physical contact during measurements and the structure diversity in the realization of sensing function. So far, optical sensors play a vital role in a large amount of technical applications [1]. Among them, optical biosensing is one of the most promising application domains following the enhanced set of requirements anticipated in biotechnology and medical developments.

Depending on the light-matter interaction process utilized, optical sensor systems differ tremendously. Physically, the interaction includes fluorescence, optical absorption, Raman scattering, photon emission, refractive index (RI), and so on. For chemical or biological sensing, fluorescence-based spectroscopy has been popularly applied due to its high sensitivity. This technique is especially suited for low-concentration measurement and even single molecule detection as reported in many studies [2]. Nevertheless, the molecule labeling with tags and the precise control of tag positions demand laborious work prior to taking measurements. Moreover, the labels themselves pose potential problems on the measurements, such as contamination and possible disruption of molecular activities. Thus label-free techniques thrive to be much more straightforward in signal analysis. Optical label-free methods contain Raman scattering based spectroscopy [3], absorption detection, and RI measurement [4]. The refractive index is one of the fundamental and inherent properties of materials. Any material modification or replacement induces RI variations. In this thesis, RI-based label-free techniques will be studied.

Chapter 2 presents the state-of-the-art of the thesis. Basic RI-based label-free optical sensors are crudely categorized based on their structures [4]: (1) surface plasmon

1. INTRODUCTION

resonance (SPR) and SPR-like sensors; (2) optical fiber based sensors; (3) ring resonator based sensors; (4) interferometer based sensors; (5) photonic crystal sensors. For each category, the working principles of the main structures are summarized and recent advances in sensing are discussed. Even though all the structures function to detect the RI variation, the signal conversion mechanism diversifies in different structures. Considering their performance evaluation and device comparison, sensor characteristics [5] are defined to be independent of the sensing configurations. Sensor characteristics represent the relationship between the output and the input. Performance evaluation has been established quantitatively with respect to two aspects: sensitivity and resolution. The sensitivity refers to the strength of interaction with the detected medium and the resolution is the minimum detectable RI variation of the system. Moreover, the sample volume, on-chip realization, and sensor multiplexing are other important factors to be discussed. From the resolution point of view, SPR sensors have been the most developed and commercialized devices due to their uncomplicated setup and their currently achieved high resolution [6, 7]. The surface plasmon wave is resulting from oscillation of free electrons on a metal surface with the electromagnetic wave. It localizes most of the energy in the medium to achieve a high sensitivity. Considering the development of compact and portable sensing systems, optical devices are pushed forward for the realization of complex and functional systems through device miniaturization, which follows the advancements of fabrication technologies. Nevertheless, the light control and manipulation is difficult due to light scattering when the size of devices is reduced from macro to nano scale. As a result of the surface plasmon wave, light can be squeezed into far subwavelength dimensions and nano-structured metal exhibits unforeseen optical properties. Therefore, the field confinement in nanoscale and the high sensitivity to environmental changes are interesting for local RI measurements. In this thesis, nano-structured metallic devices are chosen as a starting point for the design of optical sensing elements.

At the end of chapter 2, the modeling tools used are briefly described. Modeling tools are mathematical solutions for Maxwell's equations, which are physical laws for the light-matter interaction. They are essential to predict the optical properties of nanostructures. Among various modeling methods, the rigorous coupled wave analysis (RCWA) method and finite difference time domain (FDTD) method are briefly described.

In this thesis, we investigate the light interaction with metallic nanostructures for the RI detection. As metal is absorptive and thus penetration depth is short, the structured metallic thin film is integrated with a dielectric waveguide. The metallic part functions as a cavity and enables the field localization while dielectric waveguides profit from simple light injection and low-loss light propagation. The initial purpose is

to develop waveguide-based, on-chip and small volume sensors. Two specific structures are studied: slot waveguide cavity (SWC) and annular aperture array (AAA).

In chapter 3, the SWC device functions through a gold (Au) film structured by a periodic slot array, which is deposited directly above a Si waveguide. Herein the SWC is correlated to the Si waveguide via the evanescent wave overlap. The sensing mechanism for the RI detection is a Fabry-Pérot-like resonant coupling between the Si waveguide and the Au cavity. The resonant coupling is then analyzed from the transmission spectrum of the Si waveguide. Detailed theoretical study has been performed on the device parameters to evaluate their influence on the transmission spectrum. Finally, the device is fabricated and characterized in air and liquids, verifying the theoretical study. The fabrication work is carried out by my colleague Armando Cosentino and fabrication details can be referred to his doctoral thesis. The characterization part is a collaboration work between both of us.

Chapter 4 is devoted to the theoretical study of the AAA structure. The AAA patterned Au cavity is embedded in a Si_3N_4 waveguide for a resonant coupling with in-plane incidence. It has been shown that the resonance is accompanied by a high field confinement in the annular aperture and is thus suitable for small sample volume detection with a high sensitivity. In addition to the two-dimensional simulation, the three-dimensional consideration of the device realization is also taken into account in this chapter. The geometrical requirements of the fabricated device are calculated to preserve its sensing property.

Finally, a concise conclusion is presented in chapter 5.

1. INTRODUCTION

Chapter 2

State of art

This chapter reviews the background of optical sensors with respect to the interaction mechanism. Optical refractive index based label-free sensing is emphasized with a review of existing structures. In particular, the principle sensing schemes are illustrated and their most recent developments in laboratories. Sensor characteristics are discussed in addition to their performance improvement considerations. For the thesis work, the structured metallic film is selected for the sensor design, considering the field confinement property, the flexibility in device integration, and small sensing volume. The simulation tools employed in the thesis are briefly presented at the end of this chapter.

2.1 Optical Sensors

Optical sensors employ light to convert certain physical quantities into detectable optical signals (intensity, phase, spectrum, *etc.*). By measuring variations of the optical signal, the desired physical property is analyzed through the light-matter interaction process applied. Compared with their electrical or mechanical counterparts, optical sensors exhibit several advantages, such as, high-speed signal processing and the non-physical contact requirement during optical measurements, for example, during tissue sample measurements. Indeed, light propagation is much faster than electron transfer and the physical contact in electrical sensors may destroy the sample during measurements. At the same time, the strength of optical sensors depends on the availability of diverse optical properties which are employed to generate optical signals. Those properties include refractive index (RI), optical absorption, polarization rotation, fluorescence, and nonlinear optical process (lasing, Raman scattering, and multiphoton absorption and emission) [8]. Currently, optical sensors already play a significant role in a large range of technical applications: from basic light switches to complicated forms of interferometry, from spatial dimension detectors to near field optical microscopy.

2. STATE OF ART

The book *Optical Sensors: Basics and Applications* by J. Haus [1] covers all aspects in optical sensor design, including optical sensor construction kit consideration and introduction of different sensor applications. Optical sensors can be classified depending on the physical or chemical quantities they measure. Following developments in biotechnology and the medical field in the twenty-first century, biosensing flourishes to be one of the most important topics among sensor techniques. Optical biosensors are powerful and versatile tools in bio/chemical process analysis and monitoring. Thus they are adaptive in healthcare, biomedical research, drug discovery, environmental monitoring and protection [8].

This chapter concentrates on label-free sensor based on the RI detection. From the literature overview, the sensor characteristic section summarizes practical terminologies of sensors for performance consideration. Then, important results of the major sensor structures and their performance evaluation will be listed in the subsequent paragraphs.

2.1.1 Sensor characteristic

From the physical or chemical input to the output, sensors have various conversion processes which depend on the interaction applied in the system. In order to make a quantitative comparison of the performance of different sensors, a set of sensor characteristics [5] will be discussed regardless of their physical nature or signal conversion steps. Only relationships between the input and the output signal are taken into account.

General definitions of the important characteristics of sensors are given in the following paragraphs. For each parameter, the nanostructure based sensor studied in Chapter 3 will be taken as an example. The device is based on a slot waveguide cavity (SWC). The transmission spectrum of the nanostructure presents a resonant dip, which can shift depending on the refractive index (RI) of the material filling the cavity. In this particular case, we consider the RI of the analyte as the input signal and the wavelength shift of the dip as the output signal.

Transfer Function establishes an ideal relationship between the output and the input in a static configuration. This function declares the dependence of the output signal Y on the input stimulus s which can be represented by $Y = f(s)$. It can be a linear or a nonlinear function, determined by the signal conversion process. The simplest signal dependence is a linear function, represented by $Y = a + bs$, where a is the intercept, and b is the slope or sensitivity of the sensor. This linear transfer function is ideal or perfect for many sensors, which is not always the case in practise. A nonlinear relationship can be considered linear over a limited incidence range, where the sensitivity is the derivative of the nonlinear transfer curve. The sensitivity describes the reaction strength of the output to the stimulus change.

For the SWC device, the transfer function between the resonance position and the RI is linearly fitted from a theoretical study. The sensitivity is 726 nm/RIU (Refractive Index Unit) in a liquid environment.

Accuracy actually means inaccuracy of the detection, which is defined as the maximum deviation of the measured input signal from its real or true value. Due to manufacturing tolerances, material variations, and other limitations, the transfer function of real devices deviates from the ideal one. The inaccuracy reveals the largest error of the calculated input from the true input. The accuracy of the SWC device is not yet evaluated. Since the fabrication error can significantly affect the resonance position of the SWC device, the inaccuracy of the theoretical curve is large. The accuracy of the fabricated structure should be established from multi-point calibration.

Span also called full-scale input, represents the dynamic range of the input value that can be detected with an acceptable accuracy. In a RI based optical sensor, the span is the RI range that the sensor can measure. The definition of the counterpart for the output is the full-scale output, meaning the dynamic range of the output signal.

For the SWC device, it is designed to work for a wide RI range from 1.0 to 1.4. The full scale output of the SWC device is the range of the resonance position corresponding to the full RI range, which is 1.46 μm to 1.72 μm in theory.

Hysteresis shows the difference of the sensor's output when a fixed input approaches from the opposite direction. For some sensors, the output is different when the desired input is increased from a lower value or the input is decreased from a larger value. Hysteresis occurs in the deformation of some materials in response to varying forces. For optical sensors, hysteresis is not a common problem.

For the SWC device, the hysteresis is theoretically zero, since the RI variation will not deform the device.

Nonlinearity occurs for sensors with linear approximation of the transfer function. Nonlinearity is the maximum deviation of a real transfer function from its linear approximation.

In the SWC device, the transfer function is linearly approximated over a certain RI range. The characterization curve has demonstrated that this linear approximation is valid.

Repeatability estimates the ability of a sensor to conserve the same output under identical conditions. The repeatability error may be caused by thermal noise, buildup charge, and so on.

In the SWC device characterization, measurements have been taken on different days to ensure the repeatability.

2. STATE OF ART

Resolution describes the minimum increment of the input which can be accurately distinguished. Resolution has been considered to be one of the most important characteristics to evaluate the performance of a sensor. Resolution is linked to the entire measurement system, including source signal, transducer, and the detector. For RI based sensors, the resolution is defined to be the minimum detectable RI variation. Detailed discussion of resolution and its relation with the sensitivity, system noise, and so forth will be made in the next section.

In the case of the SWC sensor, we estimate an optimum resolution down to 5.8×10^{-5} RIU (See chapter 3).

Dynamic Characteristics are the time-dependent property of a sensor. Due to the fact that both a sensor and its coupling with the source of stimulus cannot always respond simultaneously, the sensor detection generally does not follow, with perfect fidelity, when the stimulus varies with time. The warm-up time, cutoff frequency, and so on have been used to characterize how quickly the sensor responds to the input. The warm-up time is the time required to achieve accurate output when the excitation signal is applied on the sensor. Optical sensors normally have an ignorable warm-up time. The cutoff frequency is the maximum frequency of the input signal when the sensor can respond to the input variation in an accurate way.

The dynamic characteristics have not been considered in the SWC device so far. The combination of micro- or nano-fluidics with sensors requires that the dynamic characteristic with respect to the response speed, depends on the sample delivery to the interaction place, the related absorption and desorption process, *etc.* The measurements with the SWC device demand a postprocessing analysis. The dynamic property then has no particular interest and significance in this case.

Environmental Factors describe the environmental conditions (temperature, humidity, *etc.*) required for proper functionality of a sensor. Environmental stability is a critical issue when a sensor becomes a product. Especially in space applications, sensors have to be adaptive to harsh environment and resistive to violent shock and vibrations. Among various environmental factors, temperature factors are crucial for the sensor performance due to their adverse effect on the sensor materials. For example, temperature induced structural change modifies the transfer function and even can destroy the proper functioning conditions of a sensor.

The SWC device is still in the initial stage of research, environmental factors are not yet considered.

Application Characteristics are concerns for a sensor taken from lab research and transferred to a practical application. Design, weight, and overall dimensions are always important aspects in certain application areas. Generally, a portable and multiplexing system is the product goal for consumer driven sensor applications. Cost is another

issue for commercialization and widespread distribution. However, in some fields such as space station, medical applications and some other fields, the accuracy and stability is the defining aspect as cost is not a limiting issue.

The standardized terminologies of a sensor have been defined in the above discussion. A more in-depth discussion can be found in other textbooks. The importance of each characteristic relies on the specific application. However, sensitivity, resolution, and lab-on-a-chip compatibility are first considered to evaluate the SWC device in this thesis. The sensitivity and resolution are to be investigated in detail considering all parameters of influence and taking the possibility for device improvements into consideration. For recent developments, system miniaturization and sensor multiplexing have achieved more attention for commercialization and portable system design. They are concerned with total sample quantity and detection cost. Another interesting trend is the integration of micro- or nano-fluidics with sensing elements. The integration enables dynamic measurement and thus activates real-time monitoring of the dynamic process.

2.1.2 Sensitivity and resolution

Refractive index (RI) based optical sensors will be discussed. Sensitivity is the ratio of the output signal change to the input signal variation, revealing physically the reaction strength during the signal conversion process. Mathematically, the sensitivity is the tangential slope of the input-output transfer curve. For the RI based optical sensor, the sensitivity S is defined as

$$S = \frac{\delta Y}{\delta n} \quad (2.1)$$

where δY is the output difference (e.g. resonance shift), and δn is the RI variation.

Depending on the working mechanism, the output signal can be light intensity, frequency, polarization, or the phase of the optical field. In most optical sensors, a supported optical mode interacts with the medium (surface plasmon resonance (SPR) sensor, Fabry-Pérot cavity sensor, *etc.*), for which the sensitivity can be decomposed into two terms in Eq. 2.2 [6].

$$S = \frac{\delta Y}{\delta n_{eff}} \frac{\delta n_{eff}}{\delta n} \quad (2.2)$$

where n_{eff} is the effective refractive index of the interacting optical mode.

The first term is the sensitivity of the output to the supported mode effective refractive index and it is related to the conversion principle of the device. The second term is the sensitivity of the mode effective index to the material index detected. It is independent of the signal conversion process and is associated with the energy

2. STATE OF ART

fraction of the field overlap in the detected material. Taking an RI based waveguide interferometer as an example, the phase φ is the output signal.

$$\varphi = k_0 n_{eff} l$$

where k_0 is the propagation constant in vacuum, n_{eff} is the mode effective index and l is the cavity length. The first term is determined by the interferometer working principle with $\delta\varphi/\delta n_{eff} = k_0 l$. The second term comes from the influence of the detected medium on the mode of the waveguide.

In general, the sensitivity enhancement is realized either by the improvement of the signal conversion method or by enhanced field energy in the medium. For example, the sensitivity of the waveguide interferometer can be enhanced either by elongation of the waveguide or by reducing the waveguide dimension to increase the field fraction in the detected material. Note that the sensitivity for the same signal detection differs tremendously in different structures. The sensitivity is one of the useful parameters to describe the performance of a sensor but alone is not sufficient.

One of the key characteristics of a sensor is the resolution, which is defined as the minimum change in the bulk refractive index that produces a detectable output signal. The resolution depends on both the sensitivity S and the output resolution r by

$$R = r/S \tag{2.3}$$

where the output resolution r is the smallest and accurately detectable output signal, which is determined by the noise level of the measurement system.

r is deduced from the transfer function perturbed by system noise, which then obscures the accurate determination of the output signal. Clearly, the improvement of the resolution R can be fulfilled by increasing the sensitivity S or by decreasing r through noise reduction. Since the output resolution is noise related, the noise source should be studied according to specific signal conversion and signal identification processes.

In a resonant RI optical sensor, the position of the extremum (minimum or maximum) is used in many cases to track the spectral shift, and then to decide the RI variation. r is conventionally established to be equal to three standard deviation (3σ) of the noise in the system [9]. The standard deviation is the square root of the statistical variance of the extremum position determination when certain distribution of noise is added to the measured signal. Studies in Ref. [9] discuss two classes of noise in the extremum position determination: amplitude variations, which presents the accumulative noise added on the spectrum, and spectral variations, which is referred to an undesired spectral shift or modifications. For amplitude noise, noise sources include thermal and shot noise in the detector, intensity noise of the signal source, signal conversion process induced noise. An approximate relationship between the quality factor (Q), the signal-to-noise-ratio (SNR), and the standard deviation of the extremum value (σ_{amp})

has been provided in Eq. 3.12. The detailed calculation process for σ_{amp} is described in Appendix A.

$$\sigma_{amp} \approx \frac{\lambda}{4.5Q(SNR^{0.25})} \quad (2.4)$$

The approximation shows the possibilities to improve the output resolution by improvements of the quality factor and SNR of the spectral resonance. In theory, σ_{amp} can be close to zero when sufficient measurements for the identical detection are averaged and the random amplitude noise is canceled finally.

For spectral variations, the noise factors are mainly induced from the non-zero thermo-optic coefficients and thermal expansion coefficients. Additionally, the spectral variation may also be limited by the spectral quantization of the source or the detector. Assuming the standard deviation of the amplitude noise σ_{amp} , the thermal induced noise σ_{therm} , and source and detector noise σ_{spec} , the output resolution r of the sensor can be approximated by

$$r = 3\sigma = 3\sqrt{\sigma_{amp}^2 + \sigma_{therm}^2 + \sigma_{spec}^2} \quad (2.5)$$

Note that the sensor with a high quality factor is limited by the thermal stabilization while the sensor with a low quality factor is limited mainly by the amplitude noise. The spectral resolution of the light source and detector is also important in some cases.

2.1.3 Optical refractive index sensors

Optical sensors correlate light properties to material information in time or frequency domains. By light-matter interaction, we have to understand here light scattering, light absorption and emission, refractive index (RI) controlling, and optical polarization rotation [8]. Among them, RI is one of the fundamental and inherent optical properties of materials. Any material replacement or material transformation induces RI variations. RI based optical sensors, which convert the RI change to an optical signal, have been considered to be a direct and label-free method. The transduction signal can be amplitude, frequency, polarization, decay time, and phase of the electromagnetic wave, relying on the mechanism and the modulation method used.

Those far, RI based optical sensors have been popularly applied in different fields such as biological and chemical sensing. In 2008 outstanding reviews have addressed various mechanisms for biosensing [4, 10]. The commercialized instrumentation of label-free detection are introduced [7, 11], for which the leading companies are listed. In Ref. [4], the basic optical RI sensor configurations or techniques are crudely categorized such as: (1) SPR and SPR-like sensors; (2) optical fiber based sensors; (3) ring resonator based sensors; (4) interferometer based sensors; (5) photonic crystal sensors. Emphasis will be given to the description of the working mechanism and their recent advances. As for sensor characteristics, sensitivity and resolution are principally considered for

2. STATE OF ART

performance evaluation, while device integration, miniaturization, and multiplexing are to be addressed as well. Although the integration of optical components including light source, transducer, and detector is the ultimate goal in sensor developments, the multiplexing of various devices onto a single substrate is a milestone for portable and low cost sensors.

2.1.3.1 SPR and SPR-like sensors

(a) SPR sensors

Since the first demonstration for gas sensing in the early 1980s [12], surface plasmon resonance (SPR) sensors have been extensively explored and developed as one of the most powerful label-free sensing techniques today. The principle, platforms, and applications of SPR sensors can be referred in excellent reviews [6, 13, 14].

Surface plasmon (SP) is a resonant coupling between the free electrons on the surface of a metal and the electromagnetic (EM) field, while most of the energy probes the medium in touch with the metal. The propagation constant of the SP is expressed in Eq. 2.6.

$$\beta_{sp} = \frac{2\pi}{\lambda} \sqrt{\frac{\varepsilon_d \varepsilon_m}{\varepsilon_d + \varepsilon_m}} \quad (2.6)$$

where λ is the wavelength in vacuum, ε_d and ε_m are the relative permittivity of the medium in contact and the metal, respectively. Due to the negative ε_m , β_{sp} is larger than the propagation constant in the medium $\beta = 2\pi\sqrt{\varepsilon_d}/\lambda$. Thereby the SP cannot be excited directly on a flat metal surface. Different excitation methods [6] including prism coupling, waveguide coupling, grating coupling, and optical fiber coupling are applied to fulfill the propagation constant matching condition by TM polarized light. SPR sensors are based on the resonant excitation of the SP. A change in the RI of the medium ($n_d = \sqrt{\varepsilon_d}$) modulates β_{sp} and then the properties of the light coupling to the SP. The modulated light properties can be the angle of incidence, the resonant wavelength, the intensity, or the phase.

Shown in Fig. 2.1(a), the prism coupled Kretschmann configuration is widely applied and commercialized for its convenience. Light is coupled to the SP when the propagation constant of the SP and the incidence are matched (Eq. 2.7), leading to a drop in light reflection.

$$\frac{2\pi}{\lambda} n_{prism} \sin(\theta) = \text{Re}(\beta_{sp}) \quad (2.7)$$

where n_{prism} is the RI of the prism, which is larger than n_d . When n_d changes, the coupling condition is tuned. A large amount of SPR sensors utilize either angular (θ) or spectral (λ) dependence of the reflection to perform the RI measurement. The primary difference between angular and spectral measurements is that angular detection focuses a monochromatic light beam on the surface while spectral detection fixes the incident

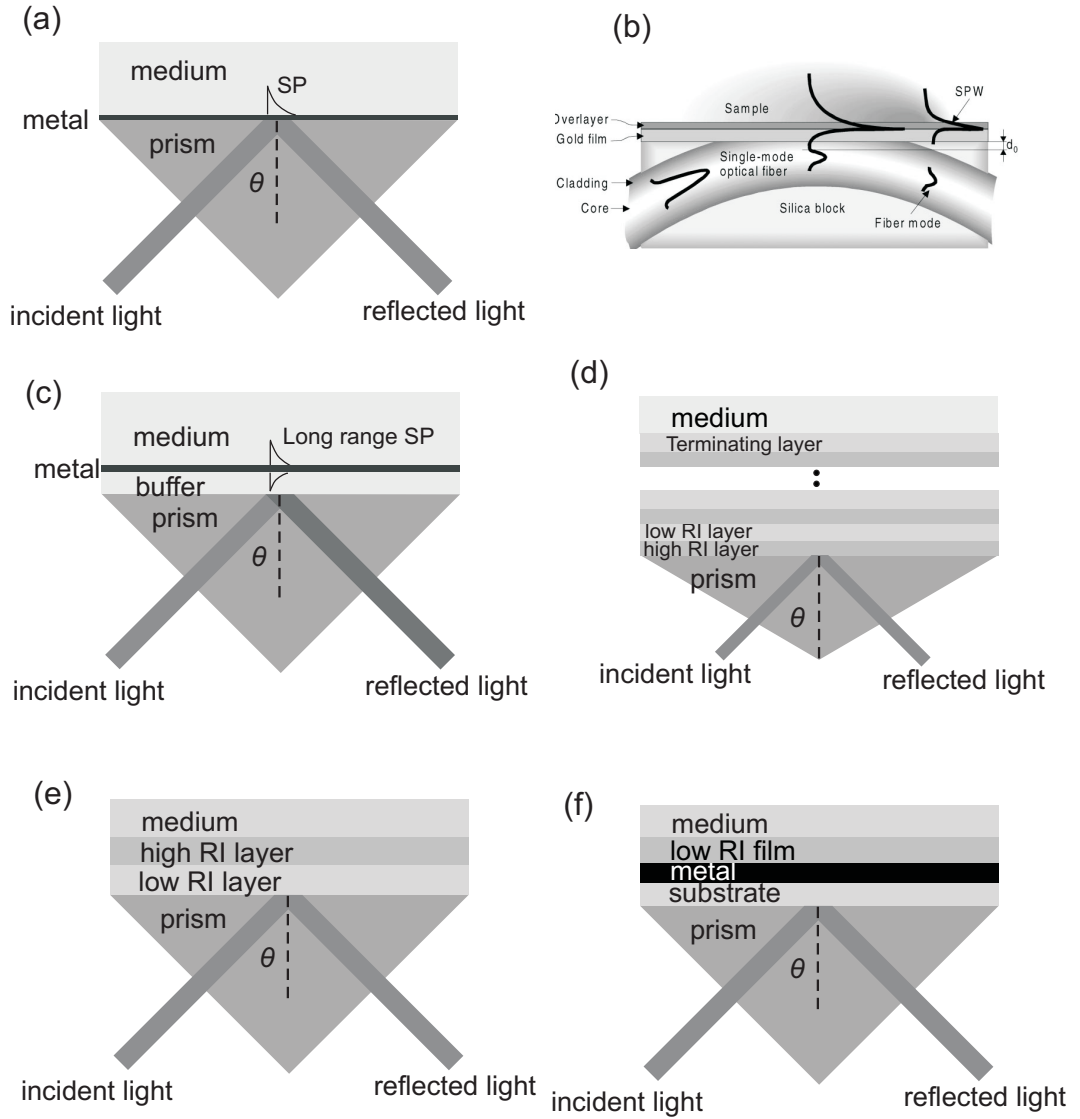


Figure 2.1: Various SPR and SPR-like sensor configurations mainly using prism coupling. (a) Kretschmann configuration for SPR sensors; (b) side-polished fiber coupling (Ref. [15]) of SPR sensor; (c) long range surface plasmon sensor; (d) Bloch surface wave sensor; (e) resonant mirror sensor; (f) metal clad waveguide sensor.

2. STATE OF ART

angle (θ) for a wide spectral band. Due to the definition, the sensitivity of the two methods shows different wavelength dependencies [16]. For angular modulation, the sensitivity decreases with wavelength, while it increases with wavelength for spectral modulation. Spectral modulation exhibits high values in the order 10^4 nm/RIU for visible light, resulting from its dependence on the dispersion of the metal and the prism. The material dispersion results in a small value in the denominator of the sensitivity calculation [16]. The sensitivity for angular modulation is in the order of 100 degree/RIU in the visible range. As for resolution, commercial instruments from Biacore [17] achieve a typical resolution of 10^{-6} to 10^{-7} RIU, which already qualifies many applications.

In addition to angle and spectral modulation, the intensity and phase of the reflected light (constant wavelength and constant incidence angle) are also studied to measure the RI variation. The phase of the reflected beam experiences a phase singularity when the reflection is close to zero. Research [18] claims that phase modulation can provide at least two orders of magnitude better resolution than with amplitude modulation. The reason is that the phase modulation has a larger sensitivity at resonance (steep slope), lower noise level of the laser, and enhanced possibilities for signal averaging and filtering. However, phase modulation is subjected to a very narrow RI detection range. A resolution of 2.8×10^{-9} RIU has been achieved by differential phase modulation while the dynamic range is merely 1.4×10^{-6} RIU [19]. The recent work [20] proposes the combination of phase detection and angular modulation to achieve a resolution of 2.2×10^{-7} RIU over an improved dynamic range of 0.06 RIU.

It is predicted [21] that the ultimate resolution of SPR sensors depends predominantly on the noise present in the light source and the detector, while the performance is independent of the coupler and the modulation methods. In addition to the improvement in resolution, research into SPR sensors is directed to the multiplexing of channels. The SPR imaging (SPRI) technique [22] shows promise for high throughput detection in which a sample array in the order of hundreds is imaged. Typical SPRI is based on the prism coupling of monochromatic light with one incident angle and the intensity of the reflected light embodies the RI variation. The reflected light from the entire array is collected by a camera. Due to intensity modulation, the resolution of SPRI devices is approximately one or two orders magnitude worse than the SPR technique by spectral or angular modulation. At the same time, efforts have been proposed for high compact, portable, or even multi-sample SPR sensing. Two compact prototype devices have been realized based on light coupling through a metal coated diffraction grating with different diffraction orders being coupled to the SP [23, 24]. One prototype has integrated ten independent microfluidic channels and the angular modulation ensures its sensing resolution to 6×10^{-7} RIU [24].

Fiber based SPR sensors combine the high sensitivity of the SPR sensor and the compact, remote control, and cost-effective properties of optical fibers. A review [25] presents various fiber-optic SPR sensors in the field for sensing different chemical, physical and biochemical parameters, on which a thin metal layer or a particle array is deposited on fibers. Generally, the cladding of the fiber has been polished and the metal layer is deposited close to the core of the fiber. The scheme of a side-polished fiber based SPR sensor is shown in Fig. 2.1 (b) [15]. The typical resolution of fiber based SPR sensors is 10^{-5} to 10^{-6} RIU. Considering performance improvements, the polarization sensitivity of the SP excitation leads to stability problems. Slavik *et al.* [15] reported that the achievable resolution of a side polished single mode fiber by depolarized light and spectral interrogation is 5×10^{-7} RIU, and where the resolution decreases to 3×10^{-5} RIU due to residual polarization of the fiber mode. The most recent work demonstrates a single-mode fiber based SPR sensor with an in-fiber tilted Bragg grating in which the influence of temperature, fragility of side polishing are minimized [26]. Its sensitivity varies between 500 and 1000 nm/RIU and the resolution still remains to be measured.

SPR sensors realize sensing using the evanescent wave that probes the medium. Thereby the sensing region is confined to the vicinity of the surface, which is determined by the penetration depth which is in the order of a few hundred nanometers. A long range surface plasmon (LRSP) sensor [27, 28] is also under investigation, employing the scheme shown in Fig. 2.1(c). When the RI of the buffer layer is similar to the RI of the medium, a symmetric mode is supported by the thin metal layer with a long penetration depth and low loss. The LRSP sensor presents advantages over conventional SPR sensors: it presents an extended probe depth into the sensing area and has a higher sensitivity and resolution to RI variations. In Ref. [27], the sensor sensitivity and resolution are 57000 nm/RIU and 2.5×10^{-8} RIU, respectively, at the wavelength of 830 nm.

(b) SPR-like sensors

Excluding SPR sensors, a group of waveguides have been applied in the Kretschmann configuration to sense the RI variation. With the schemes shown in Fig. 2.1, Bloch surface wave (BSW), resonant mirror (RM), metal clad waveguide (MCWG) will now be generally discussed.

BSW sensors [29, 30] make use of a truncated one dimensional dielectric photonic crystal to replace the metal film of the SPR sensors. The BSW is confined to the terminating layer by total internal reflection at the waveguide/medium interface. It shows exponential decay for the field envelope inside the periodic structure. As with SPR sensors, the reflected light exhibits a dip at the resonance when the propagation constant of the BSW is matched with the transverse component of the incidence wave vector. The low loss dielectric material results in a much narrower reflection dip and the photonic band gap can be engineered at any desired optical wavelength. The near

2. STATE OF ART

infrared BSW sensor ($\lambda = 1.55 \mu\text{m}$) has been demonstrated to achieve a sensitivity of more than 10^3 nm/RIU with the resolution for water solution being $3.8 \times 10^{-6} \text{ RIU}$ [29].

RM has been implemented commercially on the Kretschmann configuration for sensing since 1993 [31]. Examples for sensing can be found in the literature [32, 33]. As shown in Fig. 2.1(e), a low index layer is inserted between the prism and the high RI waveguide for total internal reflection. At least one RM mode is supported in the high RI waveguide, which is leaky on the waveguide/prism side and evanescent with the detected medium. When the propagation constant of the evanescent wave matches that of the RM mode, light is efficiently coupled to the RM mode and is coupled back to the prism after some distance of propagation along the sensing interface. The reflected light undergoes a full 2π phase variation as one scans across the resonance, being equal to π exactly at resonance. Thus the resonance is monitored by the phase change of the reflection for TE- or TM-polarized light. As in the case for sensing, the RM mode varies when RI of the medium is changed. The achieved sensitivity generally is lower than for SPR sensors due to a lower field fraction of the optical mode in the sensing material. However, the RM sensor experiences a narrower resonance and material flexibility in the device design.

MCWG [34, 35] is another waveguide structure where a leaky mode is supported by the low refractive index layer. The metal is an interval layer to increase the field overlap in the sensing medium. Thereby the bulk RI change in the sensing medium results in a larger angular shift of the resonant reflection than the RM device. Depending on the permittivity and the thickness of the metal layer, the angular analysis of the reflection can be dip-type or peak-type [35]. They are attractive alternatives to the SPR sensors due to their extended penetration depth and narrow resonance. The sensitivity is maximum when the sensor works at a wavelength close to the cutoff of the low RI layer mode.

Waveguide mode based sensing shows reduced sensitivity in comparison with SPR sensors. Their advantages mainly relies on three aspects. First, BSW and RM sensors avoid the use of metal and MCWG has the low RI film for metal protection. Second, waveguide based sensors have more flexibility in material choice and parameter optimization. The third point is the improvement of the quality factor at resonance, which compensates somehow the sensitivity decrease.

2.1.3.2 Optical fiber based sensors

Fibers serve as a low-cost and convenient tool for sensing due to their self signal-delivery function. They enable remote sensing and control at sites inaccessible for conventional spectroscopy. Fiber Bragg grating (FBG) and long period grating (LPG) are the two most notable structures for fiber sensing application.

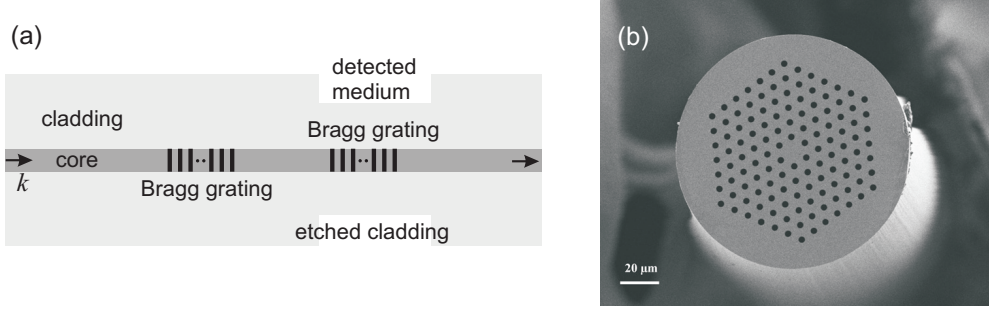


Figure 2.2: Different optical fibers. (a) scheme of dual FBG structure; (b) SEM image of the cross section of a photonic crystal fiber (Ref. [36])

A Bragg grating is a periodic RI perturbation, which is inscribed by UV exposure of the fiber core. Due to the small RI difference, a narrow forbidden band is formed in the fiber transmission called the Bragg wavelength λ_B , which is related to the period (Λ) and the effective RI (n_{eff}) of the core mode by the following equation:

$$\lambda_B = 2\Lambda n_{eff} \quad (2.8)$$

Slight modification of the period Λ or n_{eff} leads to a shift of the λ_B position. The FBG fibers are investigated for detection of strain, temperature, and load. For environmental RI monitoring, the basis is the partial influence of the surrounding material on n_{eff} of the core mode. Consequently, a FBG is side polished or chemically etched [37] to partly, or entirely, remove the cladding and enhance n_{eff} sensitivity to the RI variation of the surrounding medium. With the scheme shown in Fig. 2.2(a), a dual Bragg grating fiber is commonly applied while the second un-etched Bragg grating is the reference to cancel out the temperature effect. The sensitivity is calculated by

$$S = \frac{d\lambda_B}{dn_d} = \frac{d\lambda_B}{dn_{eff}} \frac{dn_{eff}}{dn_d} = 2\Lambda \frac{dn_{eff}}{dn_d} \quad (2.9)$$

where n_d is the refractive index of the medium. One can conclude that by dn_{eff}/dn_d , the sensitivity is proportional to the fraction of the evanescent wave that penetrates into the medium. In 2001, a side polished fiber grating functioned above the cutoff wavelength of the fiber and achieved its sensitivity for 340 nm/RIU with an improved resolution up to 2×10^{-6} RIU [38].

Long period gratings (LPG) [39, 40] have been another technique to correlate the surrounding material with the fiber core. The principal difference with respect to FBGs is the much longer period, which is typically hundreds of micrometers. The working principle is that the LPG couples the guided core mode to forward propagating cladding modes and incurs transmission dips when the propagation constants match.

2. STATE OF ART

The resonant coupling position λ_r is formulated by the effective refractive indices of the core mode (n_{eff}^{co}) and one of the cladding modes (n_{eff}^{cl}) and the period (Λ).

$$\lambda_r = (n_{eff}^{co} - n_{eff}^{cl})\Lambda \quad (2.10)$$

The direct interaction of the surrounding material on the cladding modes instills its usefulness for sensing by the detection of transmission dip shifts. However, the bare LPGs are still not competitive to perform sensing due to their rather low sensitivities. Sensitivity can be enhanced by cladding etching, fine tuning the cladding to function at the dispersion turning points, or the deposition of a high RI overlayer on LPGs [41, 42, 43]. The thin high RI material overlay on the LPG area pulls the light into the surrounding medium. In Ref. [43], the sensitivity in aqueous solutions exceeds 1000 nm/RIU for a suitable overlayer design.

Photonic crystal fibers (PhC) as variations of conventional fibers present interesting characteristics under research. The cross section of one sample is shown in Fig. 2.2(b). Note that the filling of the detected medium in the PhC cladding, where holes localize, enhances the field overlap with the medium. The LPG inscribed in PhC fibers (LPG-PhC) have been developed for bimolecular binding events to observe resonance shifts [44]. The experimental results indicate a coarse resolution of 10^{-4} RIU. The sensitivity of PhC-LPGs depends on the dimension and the lattice structure of the hole channels in the cladding which suggests flexibility in design. By filling the medium in the hole channels, the sensitivity is boosted to more than 2000 nm/RIU in aqueous solution, which is superior to all conventional solid LPG fibers [45]. This integration with nanofluidics could select PhC fibers as a potential platform as an optofluidic label-free sensor [36].

Grating-based optical fibers are useful for bulk material sensing. The sensing length is in dimensions of centimeter for the LPG requirement. Several other structures have been studied for sample volume reduction. The tapered optical fiber is one of the promising structures for which both the magnitude and the penetration depth of the evanescent field with the surrounding medium are enhanced by tapering. Based on the tapered multimode fiber interference, a recent work offers a high sensitivity 1900 nm/RIU at the material with RI of $n_d = 1.44$ [46]. The polymer fabricated microfiber is also considered to be coiled to form a resonator with a calculated sensitivity of 700 nm/RIU and an expected resolution of 10^{-7} RIU due to its high quality factor [47, 48]. Further, a copper-based microfiber loop resonator provides a robust structure for liquid sensing and estimates a resolution of 1.8×10^{-5} RIU [49]. The fiber coupler, fiber Fabry-Pérot cavity based sensors are discussed in Ref. [4], which achieve a resolution of 10^{-5} to 10^{-6} RIU.

To date, fiber-based biosensors thrive in research due to their advantages for remote sensing, low-cost, and device integration. Even though the resolution is not comparable with SPR sensors, it is informative to note their substantial advancements.

2.1.3.3 Ring resonator based sensors

In a ring resonator, light is guided by total internal reflection between the high RI material and the low RI surrounding medium. The resonant circulation around the ring is in the form of whispering gallery modes (WGMs) or circulating waveguide modes, while the resonant wavelength λ_R is given by:

$$\lambda_R = 2\pi r n_{eff} / m \quad (2.11)$$

where r is the radius of the ring, n_{eff} is the effective RI of the confined mode, and m is an integer. When a waveguide or a tapered fiber approaches the surface of the ring resonator with an evanescent wave overlap, the light is coupled to the resonator, causing a transmission dip in the spectrum of the coupling waveguide or tapered fiber. As for the RI sensing application, the resonance λ_R is tuned by the RI of the surrounding medium on n_{eff} of the confined mode. Its sensitivity can be written as:

$$S = \frac{d\lambda_R}{dn_d} = \frac{d\lambda_R}{dn_{eff}} \frac{dn_{eff}}{dn_d} = \frac{\lambda_R}{n_{eff}} \frac{dn_{eff}}{dn_d} \quad (2.12)$$

where n_d is the RI of the surrounding medium. The dn_{eff}/dn_d is influenced by the fraction of the probe field in the medium. Moreover, the sensitivity is independent of the size of the ring resonator. Even though the sensitivity is superior to other cavities, the ring resonator shows extra-high quality factors, making them applicable for sensing with a high resolution. The quality factor varies from 10^3 to 10^8 in water depending on the surface roughness and material absorption [50].

Ring resonators (Fig. 2.3) have been implemented in structures variously named as microsphere, microtoroid, microring, liquid core optical ring resonator (LCORR) [4, 50, 53, 54, 55]. The label-free detection down to the single molecule level is possible by perturbations on the WGM mode [53].

Note that the on-chip ring resonator shows its potential for mass production and the capability for easy integration with other photonic devices [56]. A silicon-on-insulator (SOI) ring resonator array has been reported to achieve a detection resolution better than 2×10^{-6} RIU and having a sensitivity of 135 nm/RIU [57]. Considering the resolution improvement, through sensitivity enhancement, such a realization can be achieved through improvement of the field fraction in the detected medium. One possible way is the implementation of a slot waveguide, which is composed of a slot located in the core of a strip waveguide where the field is confined [58]. Slot-waveguides have been demonstrated to improve the sensor sensitivity by medium infiltration in the slot. In one particular example, it has been applied to monitor molecular binding events [59]. A recent microfluidic sample is packaged for multiplex sensing and yields a bulk RI resolution of 5×10^{-6} RIU [60].

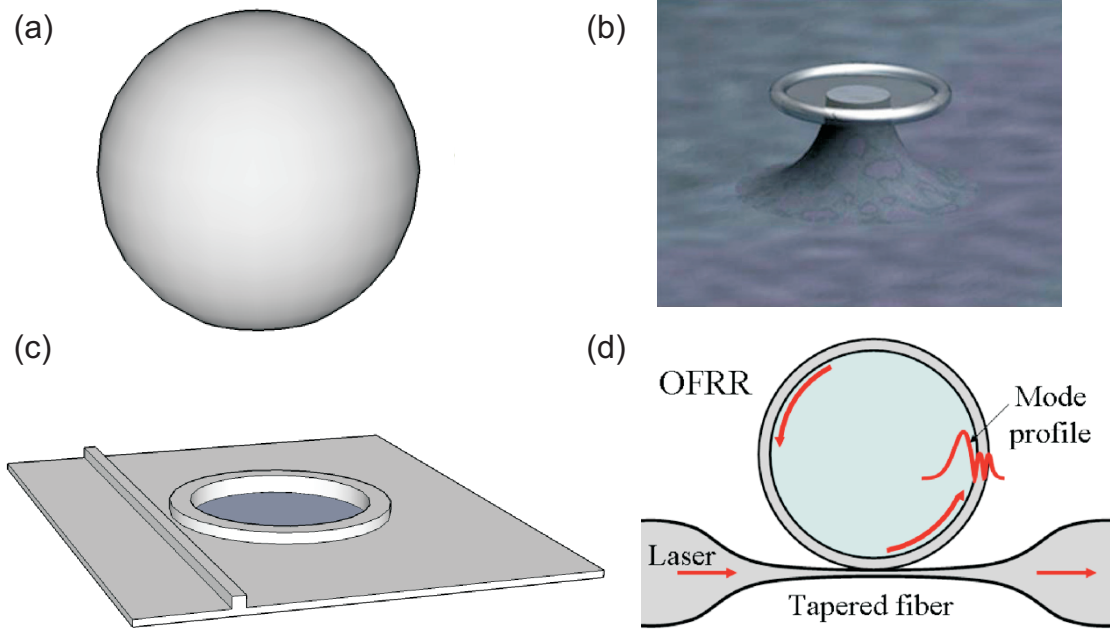


Figure 2.3: Different structures based on ring resonators. (a) microsphere; (b) micro-toroid (Ref. [51]); (c) microring; (d) liquid core optical ring resonator (Ref. [52]).

Considering sensitivity enhancement, the LCORR is very interesting for fluidic flow through the ring. By LCORR, a benchmark for ring resonator sensing has been realized for a sensitivity of 570 nm/RIU and a quality factor of 1.2×10^5 [52]. The noise equivalent resolution is 3.8×10^{-8} RIU, which is favorable when compared with other label-free optical sensors.

2.1.3.4 Interferometer based sensors

Interferometer-based sensors correlate the phase variation ($\Delta\phi$) of the light propagation to the RI variation. The phase variation $\Delta\phi$ is related to the variation of the effective RI of the waveguide mode Δn_{eff} and the interaction distance L by

$$\Delta\phi = \frac{2\pi}{\lambda} \Delta n_{eff} L \quad (2.13)$$

for which the Δn_{eff} is the partial perturbation by the surrounding medium. In the interferometer configuration, the phase in the sensing part is retrieved through light interference with a reference arm, with the reference canceling out the temperature effect. The interference with the reference arm can be interrogated from light intensity by a photodetector or an interference pattern on a screen [4], which differentiates Mach-Zehnder interferometer (MZI) and the Young's interferometer (YI), shown in Fig. 2.4.

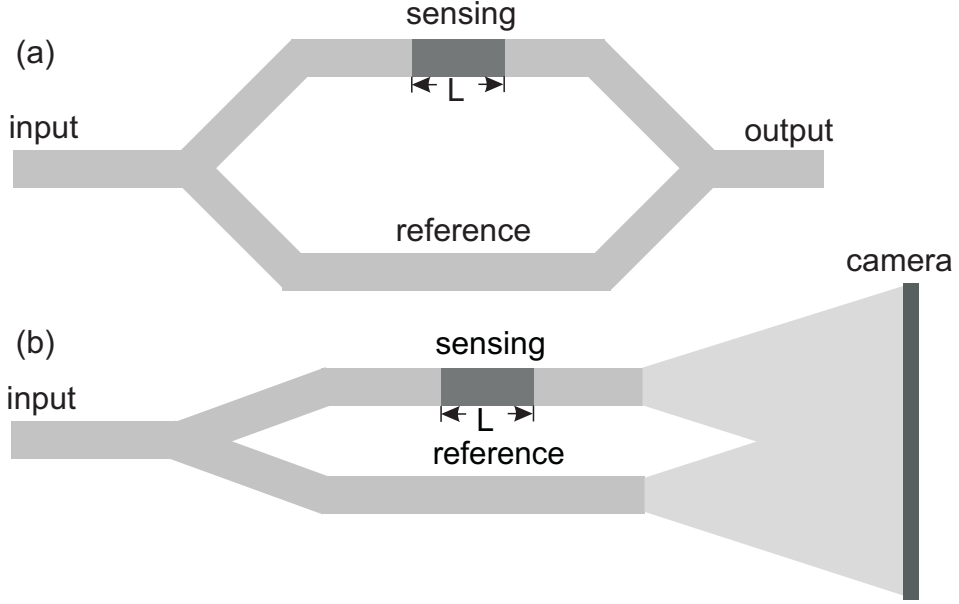


Figure 2.4: Different structures of interferometer based sensors. (a) Mach-Zehnder interferometer; (b) Young's interferometer

As a sensor, the phase sensitivity is proportional to the fraction of the evanescent wave, which probes the medium, and the sensing length L . The resolution achieved ranges from 10^{-4} to 10^{-7} RIU [61, 62], depending on the noise level of the detection system. The latest advancements follow the development route for integration with nanofluidics or even multiplexing of different sensing arms on the same chip [62, 63, 64]. An integrated bimodal waveguide MZI using standard silicon technology can achieve a resolution of 2.5×10^{-7} RIU [64]. The bimodal waveguide is a single channel waveguide operated with two waveguide modes of the same polarization and thus overcomes the difficulty in light separation by conventional Y-junction.

Due to the small amount of field immersion in the surrounding medium, interferometer-based sensors normally require centimeter scale of interaction length L to obtain sufficient sensitivity. Nanowire waveguides are theoretically proposed to increase the evanescent field in the surrounding medium. Then the interaction length is decreased by one order of magnitude to achieve a similar resolution [65]. The other proposed technique is the surface plasmon interferometer where a metal layer is embedded in a dielectric waveguide. The interference occurs between two surface plasmon modes, which are excited on both sides of the metal. The predicted resolution can be 10^{-6} RIU for a physical footprint of only $100 \mu\text{m}^2$ [66]. The same group later experimentally demonstrates, in aqueous NaCl, a sensitivity of 315.45 nm/RIU and the resolution is in the order of 10^{-3} RIU [67].

2. STATE OF ART

2.1.3.5 Photonic crystal sensors

Photonic crystal (PhC) structures comprise a novel platform for on-chip sensing of the RI. A photonic crystal is a periodic variation of refractive indices in subwavelength scale in one, two or three dimensions. The motion of the photon is altered by the periodicity in a similar way to the motion of electrons by the periodic potential in a semiconductor crystal. One typical characteristic of PhC is the photonic band gap (PBG) where photons within a prescribed energy gap cannot propagate far into the structure. Since the PBG is shifted with the RI variation of the surrounding medium, one group have used photonic band gap (PBG) to perform chemical sensing and achieved a resolution of 5.6×10^{-6} RIU in 2011 [68]. The resolution is estimated to improve to 2×10^{-6} RIU by measurement averaging to reduce the thermal noise.

Today, PhC sensors haven't achieved the resolutions currently obtained with SPR or MZI sensors. More attention has been directed to the small volume detection by a microcavity [69] and on-chip sample multiplexing [70, 71]. In the PhC microcavity, the field confinement around a defect shows an active sensing volume significantly smaller than other evanescent wave measurements. The Fauchet group has reported an achievable lowest detection volume of 1.5 fg for human IgG molecules but where the resolution is 10^{-2} RIU [71]. The PhC sensor is promising for small volume detection and their development is still in its initial stage.

Clearly the classification is not absolute as many of the listed structures belong to more than one category. The types of RI sensors show respective advantages and disadvantages over each other. The device selection ultimately depends on the characteristic of primary importance for the different applications. Considering sensitivity, different devices show clear dependence on various parameters. Generally, the sensitivity can be improved with the enhancement of the light-matter interaction volume. The resolution can be optimized either by the sensitivity or by the measurement system control (polarization, phase detection, and so on) to minimize the noise on the output signal. Recently, lab-on-a-chip multiplexing and optofluidic integration has emerged as a new analytical field for enhancing the sensing performance and simplifying the design of microsystems [50, 72, 73].

2.1.4 Optical biosensors

The optical biosensor is a device that uses specific biochemical reactions to detect chemical compounds by optical signals. A biosensor is composed of two elements: a recognition element and a transducer [50]. The recognition element is the immobilized biochemical compound on the surface of the transducer to specify the target chemicals, also called analyte. The transducer is the sensor that convert information of analytes

to detectable signals. The immobilization technique for the recognition element is critically important in a biosensor with the principal requirements having high selectivity, capture efficiency of target chemicals, stability on the surface, and reliability not to influence the chemical activity of the target. For the transducer, it must be sensitive to alterations of the target, for example, the target concentration. There are two major classes of optical transducers: fluorescence based sensors and label-free techniques [4].

Fluorescence based detection is one of the most sensitive techniques and the fluorescence intensity is correlated with the concentration of the analyte of interest and interaction strength. With light excitation from a high-power laser, the fluorescence yield has a high signal-to-noise ratio. A fluorescence sensor is adaptive for low-concentration measurement due to its high sensitivity. Even single molecule detection [2] have been reported in many studies. Nevertheless, the labeling of molecules with fluorescent tags requires laborious work and precise control of tag positions.

Label-free techniques are much more straightforward in bio/chemical sensing. In principle, optical label-free techniques are based on the molecular-binding induced change in optical properties, including Raman-based spectroscopy [3], absorption detection and RI detection.

For refractive index (RI) detection, any molecule modification or replacement of molecules instills an RI variation. Furthermore, the independence of RI on sample volume brings a potential advantage for small sample volumes. The previous mentioned configurations of optical RI sensors have all been studied for biosensing, for which the evanescent wave is penetrating into the medium to convert the RI information of the analyte to corresponding optical modes. For the evanescent wave, the field is maximum on the surface where the recognition element is immobilized. Thus the layer thickness of the recognition element and the penetration depth are essential for the detection capability of the sensor. Note that each sensor configuration is chosen according to specific applications. For example, a long penetration depth is essential for large molecule or cell detection. Considering the sensor characteristics, the resolution represents the detection of the bulk refractive index variation. A more precise term for performance evaluation of a biosensor is the limit of detection (LOD), sometimes called detection limit in the literature. It is defined as the minimum resolvable concentration of the analyte that the sensor can measure. In general, two ways are used for the illustration of LOD [6]. One way is the surface mass density (unit: pg mm^{-2}) and the other way is the sample concentration (unit: ng mL^{-1}) for known analytes. With the condition that the analyte thickness is much smaller than the penetration depth of the evanescent wave (L_{pd}), LOD is proportional to the resolution.

For the past decade, optical biosensors have advanced for improved LOD to achieve small concentration detection. The other emphasis has been on the development of immobilization techniques and exploration of portable device designs.

2.1.5 To nanostructure based sensors

Following technology advancements in the semiconductor industry, optical devices are pushed forward to realize complex and functional systems through device miniaturization. With the size reduction from macro to micro or nano dimensions, light scattering with materials takes obvious importance in modifications of optical properties. For the the interferometer based sensors, a decrease in sensitivity is accompanied by a decrease of the size (sensing length L in Eq. 2.13). On the other hand, for the resonance based sensors working at a fixed resonant wavelength, such as surface plasmon resonance, ring resonators and grating based fiber sensors, they demonstrate an independence of the sensitivity to the size (Eq. 2.7, 2.9, 2.12), under the condition that the sensor size is much larger than the diffraction limit. However, size reduction brings an additional difficulty to achieve a high quality factor for the resonance. Moreover, the micro or nano sensor dimensions demand strict and precise control of the geometry fabrication. Above all, decreasing the size means decreasing the sensor performance: the resolution.

Nevertheless, light interaction at subwavelength scale brings “extraordinary” phenomenon compared with classical optics, which can then be suitably applied for sensing. For example, the photonic crystal is a novel platform for sensor development. Note that plasmonics is a rapidly growing research field for which the metal is structured at the nanoscale. The surface wave, resulting from the oscillation of free electrons on the metal surface with the electromagnetic field, allows light to be squeezed into dimensions in far subwavelength scale [74, 75]. At the same time, most of the energy is distributed in the surrounding medium. Thereby light propagation in plasmonic devices shows extraordinary and environment sensitive properties depending on the structure. Many promising results have revealed their potential in various applications, including subwavelength optics, optoelectronics and chemical sensing.

With a metallic thin film, SPR sensors are playing an important role in sensing. When the size is confined in three dimensions, nanoparticles or nano-structured metallic thin films have been envisaged for local sensing [76, 77]. Moreover, the periodically patterned metallic films exhibit a collective optical function. Extraordinary optical transmission (EOT) [78, 79] is one of the key phenomenons, which has been studied as par of a new generation of RI based sensors [80].

In 1998, researchers demonstrated the EOT through the nanohole array structured Au film due to the SPR excitation on the film surface [78]. Since the EOT is based on light coupling on the metal surface, the resonance embraces the information of the dielectric environment. Subsequently, Brolo *et al.* applied this technique to monitor the binding of organic and biological molecules to the surface with a sensitivity of 400 nm/RIU [81]. Studies from Fainman group have improved the sensing resolution to 1.5×10^{-5} RIU by polarization controlled linewidth narrowing [82] and the sensitivity to over 1000 nm/RIU through diffraction order selection by grating coupling [83]. Other

groups utilize the planar configuration to integrate the microfluidic for real-time or parallel array sensing [84, 85]. Furthermore, the nanoholes can act as a flow channel for liquids. The optimum response time improvement is 20-fold for small biomolecules with rapid kinetics [86]. Compared with in-plane SPR sensing, the rapid delivery of analytes to the interaction region enhances the dynamic characteristics of a sensor.

For nanostructured sensors, the local interaction volume enables a detailed monitoring of molecule interaction. In this thesis, metallic nanostructures are investigated to take advantage of their local field confinement for the RI sensing. Considering the absorption from electrons, metallic structures will be integrated with dielectric waveguides to function as a on-chip platform.

2.2 Simulation Tools

Light interaction with nanostructures is complicated and the effects not anticipated. In order to predict the behavior of optical devices and design them with desirable properties, numerical techniques have been developed. The electromagnetic field interaction with any medium is described by the Maxwell's equations [87]. They are composed of Maxwell-Faraday equation (Eq. 2.14), Ampere's law with Maxwell correction (Eq. 2.15), Gauss's law (Eq. 2.16), and Gauss's law for magnetism (Eq. 2.17), for which the widely used differential forms are shown below:

$$\vec{\nabla} \times \vec{\mathbf{E}} = -\frac{\partial \vec{\mathbf{B}}}{\partial t} \quad (2.14)$$

$$\vec{\nabla} \times \vec{\mathbf{H}} = \frac{\partial \vec{\mathbf{D}}}{\partial t} + \vec{\mathbf{J}} \quad (2.15)$$

$$\vec{\nabla} \cdot \vec{\mathbf{D}} = \rho \quad (2.16)$$

$$\vec{\nabla} \cdot \vec{\mathbf{B}} = 0 \quad (2.17)$$

where $\vec{\mathbf{E}}$ is the electric field intensity (Vm^{-1}), $\vec{\mathbf{D}}$ is the electric flux density (Cm^{-2}), $\vec{\mathbf{H}}$ is the magnetic field intensity (Am^{-1}), $\vec{\mathbf{B}}$ is the magnetic flux density (Vsm^{-2}), $\vec{\mathbf{J}}$ is the electric current density (Am^{-2}), and ρ is the electric charge density (Cm^{-3}).

Another fundamental equation, known as the equation of continuity, relates the variation of the electric current density to the charge density. (Eq. 2.18).

$$\vec{\nabla} \cdot \vec{\mathbf{J}} = -\frac{\partial \rho}{\partial t} \quad (2.18)$$

In addition, at an interface between two media (medium 1 and medium 2), light must satisfy some boundary conditions (Eq. 2.19), which are derived from the integral form

2. STATE OF ART

of Maxwell's equations. Physically, boundary conditions determine the light scattering at the interface.

$$\begin{aligned}\hat{n} \times (\vec{\mathbf{E}}_2 - \vec{\mathbf{E}}_1) &= 0 & \hat{n} \times (\vec{\mathbf{H}}_2 - \vec{\mathbf{H}}_1) &= \vec{\mathbf{J}}_s \\ \hat{n} \cdot (\vec{\mathbf{D}}_2 - \vec{\mathbf{D}}_1) &= \rho_s & \hat{n} \cdot (\vec{\mathbf{B}}_2 - \vec{\mathbf{B}}_1) &= 0\end{aligned}\tag{2.19}$$

where \hat{n} is the unit vector normal to the interface pointing from medium 2 to medium 1.

The constitutive relations (Eq. 2.20) describe the macroscopic properties of the medium considered.

$$\begin{aligned}\vec{\mathbf{D}} &= \varepsilon_0 \varepsilon_r \vec{\mathbf{E}} \\ \vec{\mathbf{B}} &= \mu_0 \mu_r \vec{\mathbf{H}} \\ \vec{\mathbf{J}} &= \sigma \vec{\mathbf{E}}\end{aligned}\tag{2.20}$$

where constitutive parameters ε_0 , ε_r , μ_0 , μ_r , σ denote the vacuum permittivity, relative permittivity, vacuum permeability, relative permeability, and conductivity of the medium, respectively. The medium is defined to be linear when ε_r , μ_r , σ are independent of $\vec{\mathbf{E}}$ and $\vec{\mathbf{H}}$. Otherwise the medium is nonlinear. It is homogeneous if ε_r , μ_r , σ are not functions of space and inhomogeneous otherwise. It is isotropic when ε_r , μ_r , σ are not related to the field direction or anisotropic otherwise. For linear, isotropic, and non-magnetic medium, which is considered for all the materials used in the thesis, $\mu_r=1$ and ε_r is only frequency dependent for dispersive metals.

Maxwell's equations and the constitutive equations decide the exchange of the electromagnetic field in the medium. Note that the partial differential equations are difficult to solve analytically. An abundance of numerical methods have been developed and studied. A detailed description of the most commonly used numerical techniques is given in the book *Numerical Techniques in Electromagnetics* by Matthew. N. O. Sadiku [88]. Each method shows its respective advantages and disadvantages. The choice of one numerical method over another depends on the structure for modeling and the optical parameters to be obtained. Rigorous coupled wave analysis (RCWA) and finite difference time domain (FDTD) method are the two principle methods used in this thesis. A brief description of each is given herein.

2.2.1 Rigorous coupled wave analysis (RCWA)

By Fourier transform, the electric and magnetic field in the time domain are related to their frequency domain counterparts through the time-harmonic component ($e^{j\omega t}$) and the relations are $\vec{\mathbf{E}} = \vec{\mathbf{E}}(\omega)e^{j\omega t}$, $\vec{\mathbf{H}} = \vec{\mathbf{H}}(\omega)e^{j\omega t}$. Substituting the transform in Maxwell's equations, the time dependence is canceled. Then the differential equations for $\vec{\mathbf{E}}$ and $\vec{\mathbf{H}}$ can be separately obtained by eliminating each other with the aid of the

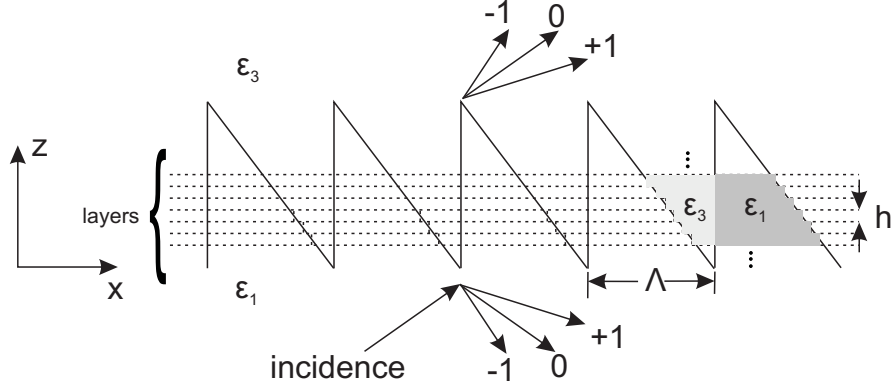


Figure 2.5: Scheme of RCWA method on one periodic grating.

constitutive equations. With linear, isotropic, and non-magnetic medium, one obtains the wave equations for $\vec{\mathbf{E}}$ and $\vec{\mathbf{H}}$ in Eq. 2.21.

$$\begin{aligned} \vec{\nabla} \times \left(\frac{1}{\mu_0} \vec{\nabla} \times \vec{\mathbf{E}}(\omega) \right) - \omega^2 \epsilon_0 \epsilon_r \vec{\mathbf{E}}(\omega) &= -j\omega \vec{\mathbf{J}}(\omega) \\ \vec{\nabla} \times \left(\frac{1}{\epsilon_0 \epsilon_r} \vec{\nabla} \times \vec{\mathbf{H}}(\omega) \right) - \omega^2 \mu_0 \vec{\mathbf{H}}(\omega) &= \vec{\nabla} \times \frac{1}{\epsilon_0 \epsilon_r} \vec{\mathbf{J}}(\omega) \end{aligned} \quad (2.21)$$

An eigenmode represents a solution of wave equation and thus the modes which are supported in the structure. For the simulation of periodic structures such as grating, the RCWA method, which is based on the eigenmode expansion technique, is an efficient method. The scheme of the RCWA method is shown in Fig. 2.5 for one example. It begins with slicing the structure into layers. Within each layer, the structure profile does not change in the propagation direction (z direction) and the optical field in each layer is the sum of the supported eigenmodes. The incident field is priori-assigned by a set of eigenmodes with weighting coefficients. When light propagates among adjacent layers, boundary conditions (Eq. 2.19) are applied for scattering coefficient calculation of eigenmodes.

RCWA method solves the wave equations without approximation. It is mathematically rigorous while the accuracy limit depends on two aspects: the structure profile description, which is controlled by the slab thickness h in the scheme, and the finite number of eigenmodes, which are used to present the optical field.

The RCWA method models light propagation in a straightforward manner. One calculation simulates for a single frequency and the spectral property requires a series of calculations at each separate frequency. They generally perform fast and accurate modeling for structures when eigenmode calculations are not too complicated. For the one dimensional structures composed of different material slabs in this thesis, the eigenmode is modeled by the open source called Camfr [89], which is developed by Bienstman *et al.* [90].

2.2.2 Finite difference time domain (FDTD) method

The Finite Difference Time Domain (FDTD) method has been initiated by Yee [91] in 1966. The main book entitled *Computational electrodynamics: The Finite-Difference Time-Domain Method* is written by A. Taflov and S. Hagness [92]. The FDTD method is based on the numerical “resolution” of the Maxwell’s equations, especially the Maxwell-Faraday equation (Eq. 2.14) and Ampere’s law with Maxwell correction (Eq. 2.15). These two vector curl equations are first decomposed into six scalar equations for derivative relation and thus each components of the electric ($\vec{\mathbf{E}}$) and magnetic ($\vec{\mathbf{H}}$) fields are separated.

Following the Taylor’s theorem in the case of a central finite difference, the derivatives can be written in a discretized space and time domain. Each grid in the rectangular coordinate system has side dimensions δx , δy , δz and a time step δt . Introducing the notation $F(x, y, z, t) = F^n(i, j, k)$ for any function F from curl equations decomposition, where $x = i\delta x$, $y = j\delta y$, $z = k\delta z$, $t = n\delta t$, $i, j, k, n \in \mathbb{N}$, the first-order derivatives for space and time are approximated by:

$$\frac{\partial F^n(i, j, k)}{\partial x} \approx \frac{F^n(i + 1/2, j, k) - F^n(i - 1/2, j, k)}{\delta x} \quad (2.22)$$

$$\frac{\partial F^n(i, j, k)}{\partial t} \approx \frac{F^{n+1/2}(i, j, k) - F^{n-1/2}(i, j, k)}{\delta t} \quad (2.23)$$

Based on this approximation with second-order accuracy and curl equation decomposition, the modeled space is composed of multiple unit cells called Yee’s cell which is shown in Fig. 2.6 [92]. In each cell, every component of the electric field is surrounded by the curl equation defined magnetic field components and vice versa. Positions for the calculated electric field and magnetic field are half-grid shifted from each other as shown by the vector in Yee’s cell. During the calculation, the electric field component of grid (i, j, k) at time step $n + 1$ is determined by the electric field component of previous time step (n) and the surrounding magnetic field components, which are half a grid away in Yee’s cell, at time step $(n + 1/2)$. The magnetic field component is solved in a similar manner for the next time step $(n + 3/2)$. Between adjacent cells, the boundary condition is inherent in the Yee’s cell. Thereby, all components of the electromagnetic field are solved step by step over the whole computation space with time evolution.

The accuracy of the computation relies on the first-order derivative approximation (Eq. 2.22, 2.23), from which the cell size and time step are critical. In order to achieve a sufficiently high numerical accuracy, the spatial increment must be fine enough compared to the wavelength (usually $\leq \lambda/10$) or minimum dimension of the scatterer. The time increment δt should satisfy the condition given by

$$u_{max}\delta t \leq (1/\delta x^2 + 1/\delta y^2 + 1/\delta z^2)^{-1/2} \quad (2.24)$$

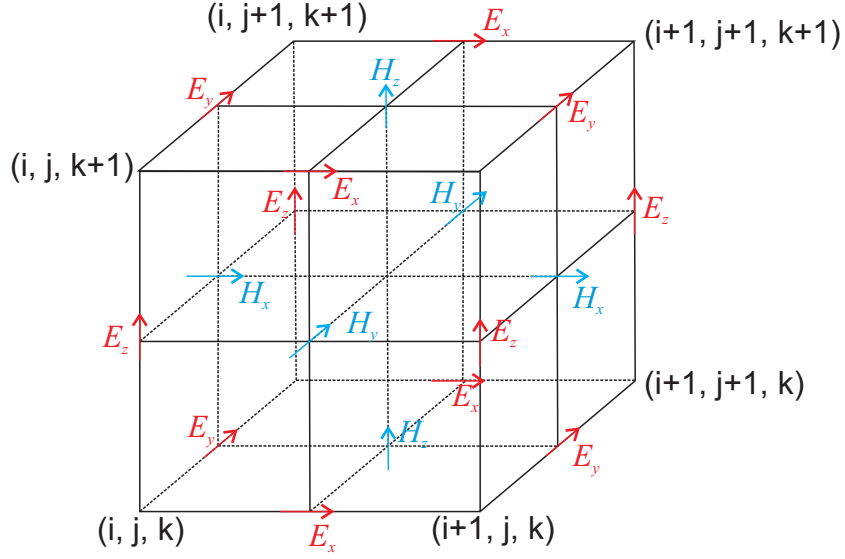


Figure 2.6: Yee's cell for the FDTD method [92].

where u_{max} is the maximum wave phase velocity inside the cell.

Since the calculation domain covers the whole structure, no computer can handle calculations for models with infinite size. An artificial boundary is enforced on the calculation edge to truncate the calculation domain and to emulate infinity. Perfectly matched layers (PMLs) are preferentially used to absorb propagation waves while almost no light is reflected back to the model. The property of the PML demands enough space between scatterers and the boundary to minimize the artificial enhancement of evanescent wave by the PMLs.

The FDTD method is versatile for the modeling of complex structures. The discretization of space into grids makes the computation adaptive to arbitrary distribution of different materials, such as nonlinear, inhomogeneous materials. Moreover, when the illumination is a broadband pulse, it models a well selected spectral range with a single run. However, the spatial and time discretization brings a large calculation burden and it is time-consuming, especially for a relatively large model size or strongly resonant structure.

In the thesis, the modeling of the SWC device and the AAA structure is based on the finite integration time domain (FITD) method [93]. This method is implemented in Microwave studio, commercialized by the company CST Computer Simulation Technology AG. [94]. The FITD method is similar to the FDTD method except that it discretizes the integral form of Maxwell's equations rather than the differential ones. The spatial discretization generates grid system with a dual mesh set-up in one grid. The similarity for FITD and FDTD methods shows the same accuracy and boundary condition requirements.

2. STATE OF ART

In our work, the fabrication process is performed in Center of MicroNanoTechnology (CMi), EPFL. The description of fabrication techniques and related problem discussion can be referred in the thesis of Armando Cosentino, who is the project collaborator in OPT group.

Chapter 3

Slot Waveguide Cavity

3.1 Introduction

Optical sensors based on refractive index detection [4] are attractive due to their versatile structures and label-free nature they provide. The various configurations are discussed in chapter 2. They can generally be classified into two groups: waveguide based devices and surface plasmon devices.

For waveguide based devices, light propagates through a strip waveguide or a fiber and the evanescent field, which penetrates into the analyte (material surrounding the sensor), is used for the refractive index detection. The optical fiber based sensors and waveguide interferometer based sensors can achieve a resolution down to 10^{-6} RIU (Refractive Index Unit) or even 10^{-7} RIU [38, 61]. However, the small interaction of the evanescent wave with the analyte requires that the sensing area (length) is in the order of millimeter to centimeter to attain enough interaction volume. Attempts for miniaturizing these sensors have been implemented using photonic crystal cavities [95]. But decreasing the size of the sensor means decreasing its resolution, which is either due to the decrease of the sensitivity (e.g., interferometer) or due to the degradation of the measurement resolution in a resonance based sensor (e.g., ring resonator). Indeed the sensitivity is proportional to the interaction volume between light and analyte. The measurement resolution depends on the quality factor of the resonance, which may deteriorate due to the size reduction. It is evident that a compromise between the size of the sensor and the resolution needs to be found.

For the second group based on surface plasmon devices, the negative permittivity of the metal localizes most of the field fraction in the analyte and thus enhances the sensitivity. The well developed surface plasmon resonance (SPR) sensors may achieve a sensitivity in the order of 10^4 nm/RIU and a resolution as high as 10^{-8} RIU [27]. Generally, these sensors are based on the Kretschmann configuration [13, 14, 96, 97], which

3. SLOT WAVEGUIDE CAVITY

does not lead to high efficiency if a large integration of devices is needed. Some attempts have been made to create SPR sensors using metallic nanostructures [76, 77, 98]. These are promising candidates to achieve both high enhancement and a confinement of the electromagnetic field in a small volume. Nanostructures then appear as the ideal solution for the integration of different optical sensors having high sensitivities.

Veronis and Fan [99] and Dionne *et al.* [100] have shown that a plasmonic mode can be supported and confined in a far subwavelength slot of a few tens of nanometers in width. This mode shows potential towards chip-scale optical circuit realization with subwavelength-scale localization. Experimental demonstrations have been realized to bridge the dimensional gap between macroscopic optics and plasmonic devices [101, 102], see Delacour *et al.* in 2010 [102]. In this paper they studied the efficient coupling from a classical silicon waveguide to a copper plasmonic nanoslot waveguide where silica fills the 100 nm-width slot. The localized field in such tiny slot is attractive for small-volume sensing. We propose here an application of such a metallic slot with light confinement with an air interface. Note that the field confinement is accompanied by a strong light absorption due to energy transfer to local electrons. It is not efficient to achieve a long propagation lengths using metallic waveguides. The integration with dielectric structures takes advantage of the small analyte volume in the slot region and shows good compatibility with other photonic devices, such as photonic crystals. The device design and property analysis, fabrication process and experimental measurements will be illustrated in the following sections.

3.2 Design & Principle

A three dimensional (3D) schematic view of the studied structure is present in Fig. 3.1. It consists of a dielectric slab waveguide on top of which lays a thin film gold (Au) cavity. The waveguide is composed of a silicon dioxide (SiO_2) layer and a silicon (Si) layer, deposited onto a SiO_2 substrate. The Au cavity is a periodic slot grating, extended in the x direction, which will be called a slot waveguide cavity (SWC) in the subsequent discussion. The geometrical parameters of the cavity are: the slot width (w), the thickness of the gold layer (h), the cavity length (l), and the periodicity (p). The thicknesses of the SiO_2 and Si layers are h_{SiO_2} and h_{Si} , respectively. In this device, TM polarized light, with the electric field perpendicular to the slot axis (z direction), is taken into account. Light propagates through the Si waveguide and is coupled with the SWC at the overlap region. The coupling occurs via the evanescent wave, as the evanescent tail of the propagation mode in the Si waveguide penetrates into the supported mode of the slot structure.

A commercial software (CST Microwave Studio) [94], working with the finite integration time domain (FITD) method, is used to compute the optical properties and

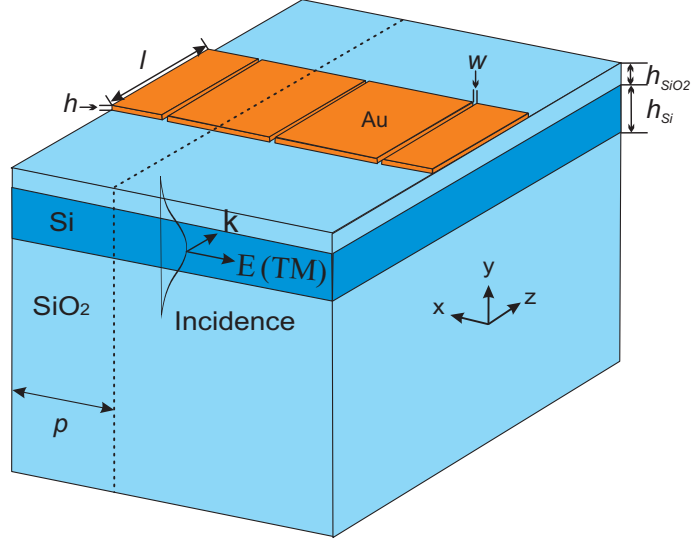


Figure 3.1: Schematic view of the studied device with a periodic slot array extended in the x direction. The device parameters are: the slot width (w), the gold thickness (h), the cavity length (l), the periodicity (p), the Si thickness (h_{Si}), and the SiO₂ thickness (h_{SiO_2}).

response of the device. In the model, periodic boundary conditions are used to simulate infinity of the structure in x direction. Perfectly matched layers (PMLs), which absorb propagating waves, are applied in the other two directions (y and z directions). The structure illumination is the fundamental optical mode supported by the waveguide (SiO₂/Si/SiO₂), for which the mode profile is illustrated in the scheme. Since the mesh size is critical in determining the calculation accuracy, it has been varied to verify the convergence of results when the size is reduced. In particular, the metallic cavity should be finely discretized where details are crucial. Finally, an adaptive mesh is considered in this model: the step size is 2 nm in the Au cavity area and about 20 nm in the other regions. Note that the dispersion property of Au is taken into account using the Drude model (Eq. 3.1):

$$\epsilon_{Au} = 1.0 - \frac{\omega_p^2}{\omega^2 - i\omega\gamma} \quad (3.1)$$

where the bulk plasma frequency is $\omega_p = 1.2 \times 10^{16} \text{ s}^{-1}$, the damping rate is $\gamma = 1.25 \times 10^{14} \text{ s}^{-1}$, and ω is the angular frequency.

The chosen parameters ω_p and γ enable a fit in good agreement with the experimental values of the permittivity of Au from Ref. [103] in the wavelength range of interest (1.3 μm to 2.4 μm). The accuracy verification is demonstrated in Appendix B, where the transmission spectrum, from the Drude-fitting replacement of the Au permittivity, is compared with that of the point-by-point calculation for the corresponding Au permittivity. The dielectric constants for Si and SiO₂ are set, respectively, to be

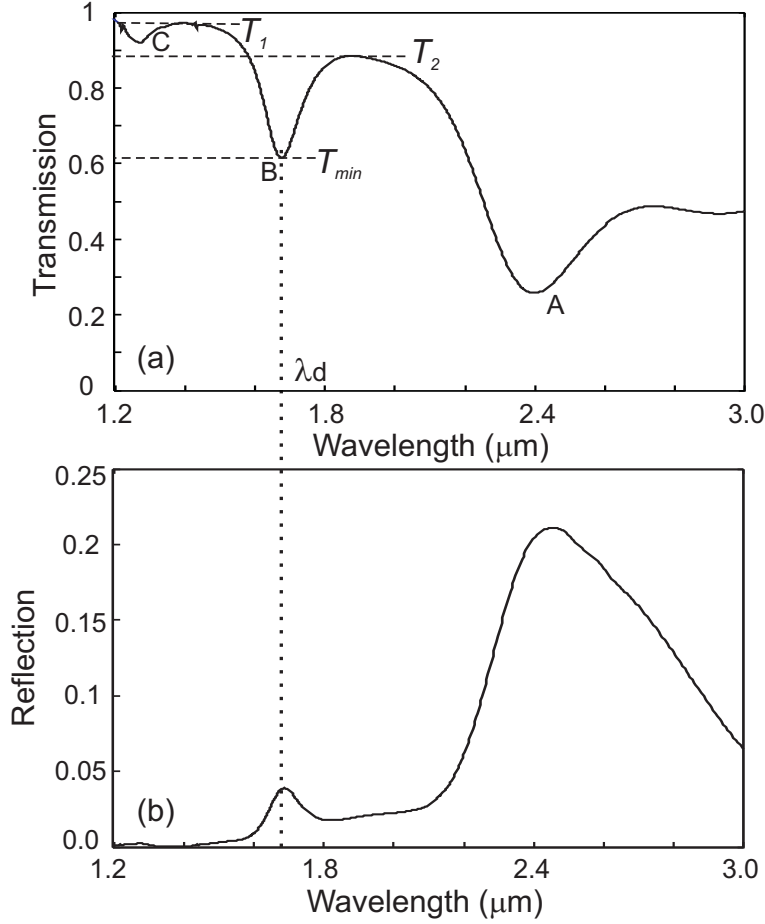


Figure 3.2: Normalized transmission (a) and reflection (b) spectra of the slot waveguide cavity for $p = 500$ nm, $l = 800$ nm, $h = 20$ nm, $w = 20$ nm, $h_{SiO_2} = 100$ nm, $h_{Si} = 220$ nm. The amplitude of resonance B is determined by $A_d = (T_1 + T_2)/2 - T_{min}$.

$\varepsilon_{Si} = 11.9716$ ($n_{Si} = 3.46$) and $\varepsilon_{SiO_2} = 2.074$ ($n_{SiO_2} = 1.44$). The device parameters are $p = 500$ nm, $l = 800$ nm, $h = 20$ nm, $w = 20$ nm, $h_{SiO_2} = 100$ nm, $h_{Si} = 220$ nm.

3.2.1 Spectrum analysis

The normalized transmission and reflection spectra of the structure (including the waveguide and the substrate) are given in Fig. 3.2 for TM polarization. One can observe three transmission dips A, B and C, corresponding to the resonances of the structure. The normalized electric field intensity $|E|^2$ distribution and the phase profile φ in the direction of light propagation direction (+ z) in the centre of the slot are displayed in Fig. 3.3 for the three resonances A, B, and C.

The electric field intensity profiles in the + z direction show that the electric field is highly confined in the air slot of the Au cavity. According to the study of Vero-

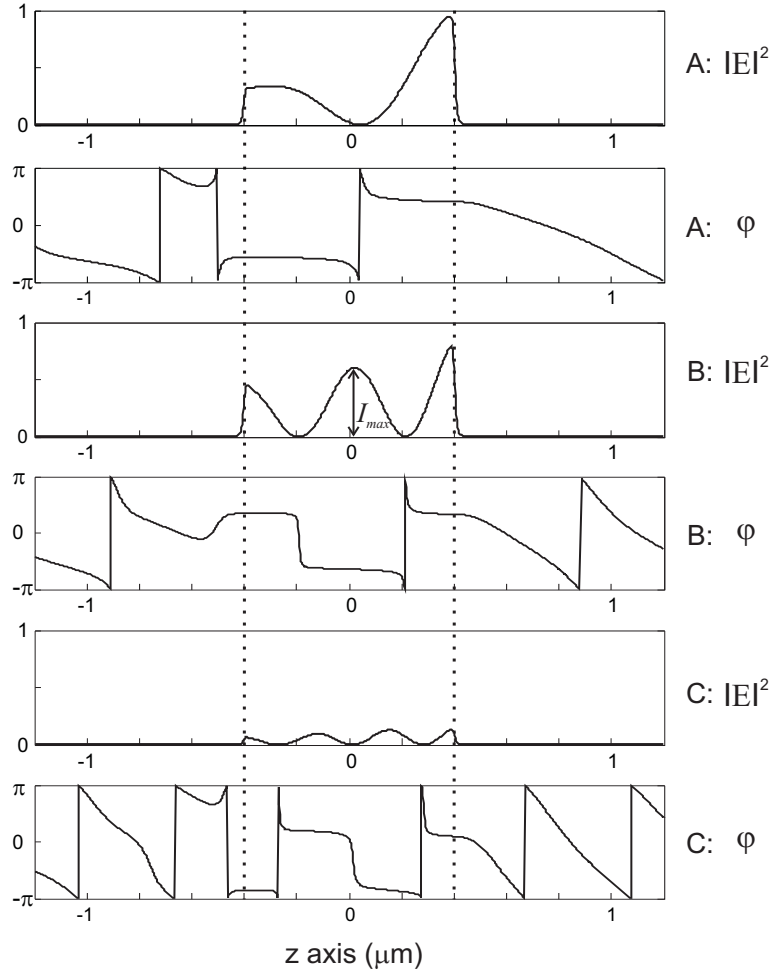


Figure 3.3: Normalized electric field intensity $|E|^2$ distribution and phase φ profile in the central of the air slot for the different resonances A, B, C (see Fig. 3.2), respectively. The dashed lines indicate the ends of the slots.

3. SLOT WAVEGUIDE CAVITY

nis and Fan [99, 104], light can be well localized in a far subwavelength slot of the metal-insulator-metal (MIM) structure. The localization is supported over the whole spectrum of analysis, as the spectrum range is below the cut-off wavelength of the supported mode. Nevertheless, the field localization is further enhanced at the three transmission resonances. From Fig. 3.3, this improvement is due to the Fabry-Pérot (FP)-like behavior of the cavity, which improves the evanescent wave coupling efficiency to the slots. The phase profiles show the existence of a standing wave in the slots while light propagates through the slots. The phase difference between the forward and backward propagating waves in the cavity is equal to π , 2π and 3π for resonances A, B and C, respectively. It corresponds to the resonance condition of a classical FP cavity: $\varphi = m\pi$ where m is an integer. The resonances A, B and C correspond to the first three modes of the FP, which is confirmed by the intensity $|E|^2$ distribution in the air slot showing 1, 2 and 3 zeros respectively.

The reflection spectrum (Fig. 3.2 (b)) shows reflection peaks at resonances A and B. The peak at resonance C is too small and will not be considered. The spectral property of the device is similar to that of a ring resonator [105]. In the SWC device, propagating light in the Si waveguide is coupled to the Au cavity through the evanescent wave overlap. At the FP-like resonance of the cavity, light is efficiently coupled to the cavity and thus induces a dip in the transmission spectrum of the Si waveguide. At the same time, the accumulated light in the cavity is coupled back to the Si waveguide to form a reflection peak. The peak height in the reflection spectrum and the dip amplitude in the transmission spectrum are both related to the coupling strength and the resonance property of the cavity. The peak and dip at position A in Fig. 3.2 have the maximum amplitude compared with that at position B and C. In other words, resonance A has the maximum amount of light which is coupled to the air slot array.

For TE polarization with electric field perpendicular to the Si/SiO₂ interface, no resonance exists for the Au cavity. The transmission and reflection spectra of the Si waveguide are not interesting for investigation.

3.2.2 Quantitative FP analysis

From the phase and electric field intensity profile description, Fabry-Pérot (FP) resonance is the mechanism explaining the existence of transmission dips. In this section, quantitative analysis is to be established step by step to verify the details of each resonance. The resonance condition in the FP model will first be discussed. Then the calculation of supported modes will be explained. Finally, we will see how the FP model can fit the observed features of SWC.

Firstly, the FP interferometer model (shown in Fig. 3.4) is introduced to simplify the working principle of the device. In Fig. 3.4, the cavity of the FP interferometer

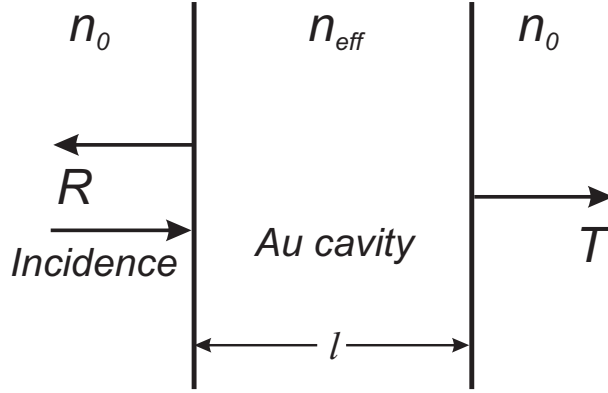


Figure 3.4: Simplification of the Au cavity of the SWC device by a Fabry-Pérot interferometer model.

represent the slot array structured Au cavity. The effective refractive index of supported modes n_{eff} depends on the geometry of the slot array and the illumination wavelength.

In the FP model, the normalized transmission (T) is calculated by Eq. 3.2 [106].

$$T = \frac{T_{max}}{1 + (2F/\pi)^2 \sin^2(\pi f / \nu_F + \chi)} \quad (3.2)$$

with

$$T_{max} = \frac{t^2 e^{-\alpha_s l}}{(1 - r)^2}; \quad (3.3)$$

$$F = \frac{\pi \sqrt{r}}{1 - r}; \quad (3.4)$$

$$r = \frac{(n_{eff} - n_0)^2}{(n_{eff} + n_0)^2} \exp(-\alpha_s l); \quad (3.5)$$

$$t = 1 - \frac{(n_{eff} - n_0)^2}{(n_{eff} + n_0)^2}; \quad (3.6)$$

$$\nu_F = \frac{c_0}{2n_{eff}l}; \quad (3.7)$$

$$\chi = \arg\left(\frac{n_{eff} + j\frac{\alpha_s c_0}{2\pi f} - n_0}{n_{eff} + j\frac{\alpha_s c_0}{2\pi f} + n_0}\right). \quad (3.8)$$

where l is the length of the cavity, α_s is the absorption coefficient of the cavity, c_0 is the light speed in vacuum, f is the frequency, F is the finesse, r is the reflection including reflection coefficient at each interface and the consideration of light absorption inside the cavity, t is the transmission efficiency at the interface, ν_F is the frequency spacing of adjacent resonance orders, χ is the reflection induced phase shift at the interface.

3. SLOT WAVEGUIDE CAVITY

From the transmission calculation of the FP interferometer, a resonance appears when the phase matching condition (Eq. 3.9) is satisfied ($T = T_{max}$ at λ_d).

$$\pi f / \nu_F + \chi = q\pi \quad (3.9)$$

where q is an integer.

Physically, light with different path lengths interferes inside the cavity, where the different light paths come from the reflection at the edges of the cavity. With constructive interference, which satisfies Eq. 3.9, the transmission is maximized when the cavity releases the stored light and the reflection of the FP cavity is minimum. In the SWC device, when conditions for constructive interference inside the cavity are satisfied, maximum light is coupled and stored in the cavity and the transmission of the Si waveguide is minimized. Simultaneously, part of the coupled light is coupled back to the reflection arm of the Si waveguide and its reflection is maximized at the resonance. Even though the transmission (T) and reflection (R) spectra of the SWC device are not exactly the same as in the case of the FP interferometer, the spectral properties (resonance position, quality factor of the dip, etc.) can be analyzed analogously with the FP cavity. From Eq. 3.9, the effective index (n_{eff}) of the slot array is the key aspect in the calculation. Herein it depends on the geometrical dimensions of the cavity $n_{eff} = n_{eff}(f, p, l, h, w, h_{SiO_2}, h_{Si})$.

For the second step, calculations have been made to check the supported modes of the cavity. Based on the complex propagation constant $\beta = \beta_r + j\beta_i$ calculation, mode effective refractive index n_{eff} and the absorption coefficient α_s in FP resonance conditions are defined by $n_{eff} = \beta_r / k_0$ and $\alpha_s = 2\beta_i$, respectively. $k_0 = 2\pi c_0 / f$ is the wave vector in vacuum. The model is the same as the geometrical setting in Fig. 3.2. For the spectral range 1.28 μm to 2.5 μm , two modes are supported by the structure with the electric field amplitude ($|E|$) distribution shown in Fig. 3.5. The field fractions in the air slot are different for the two modes. In mode 1, the light is more distributed in the Si waveguide while mode 2 has a strong field localization in the air slot region. The field confinement of mode 2 will result in a stronger mode dispersion due to Au dispersion and leads to additional light losses in Au. Their dispersive properties are given in Fig. 3.6. The x axis “Wavelength” corresponds to the wavelength in vacuum. The propagation length L is defined by the absorption coefficient $L = 1/\alpha_s$. With increased light wavelength, the effective refractive index n_{eff} of both modes is decreased. Mode 1 extends more light upward in the slot region and L decreases with wavelength, indicating that the effect of the Au layer on the optical field in the Si waveguide is more pronounced. Mode 2 extends more light downward to the substrate and more light out of the slot resulting in a longer L , indicating that the ability of the slot to confine light is decreasing with increasing wavelength. When the wavelength is longer than 2.5 μm , mode 2 becomes leaky. Within the interesting wavelength range,

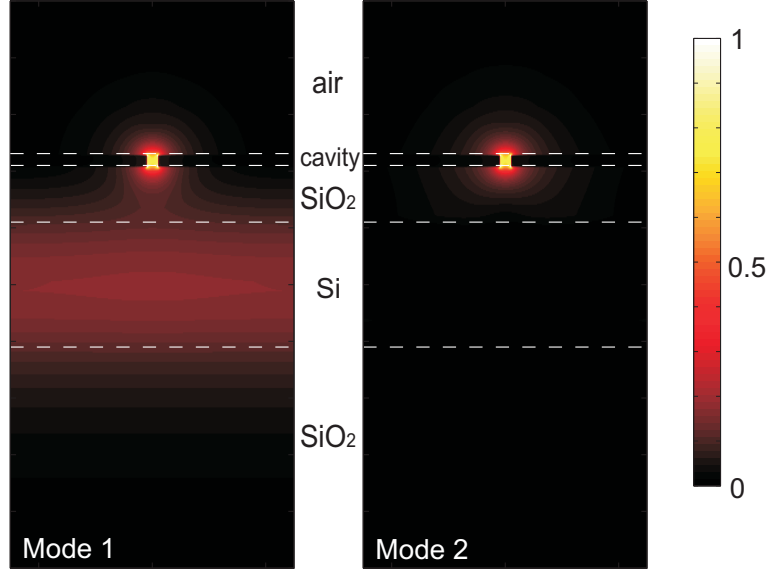


Figure 3.5: Electric field amplitude ($|E|$) distribution of the supported modes by the Au cavity. The dashed lines shows the position of different layers.

mode 1 has a larger n_{eff} than mode 2. And L of mode 2 is less than $5.5 \mu\text{m}$ due to the Au absorption. L for mode 2 at A, B and C resonances are $3.96 \mu\text{m}$, $1.95 \mu\text{m}$, $1.57 \mu\text{m}$, respectively. Both modes may play their roles in determining the resonance position. Note that there exists other modes beyond the chosen wavelength range. For wavelength $\lambda < 1.28 \mu\text{m}$, there is a third mode. As with mode 1, most of its energy is located in the Si layer for mode 3. Since it is close to the edge of our spectral range of interest, mode 3 will not be considered in detail.

During the third step, the phase condition is discussed for the two modes at the three transmission resonances A, B, and C. The results are listed in table 3.1. For each mode in the table, q' is defined by $q' = f/\nu_F + \chi/\pi$. And ν_F , χ are calculated from n_{eff} and α_s . From the electric field distribution and the phase analysis in Fig. 3.3, the phase condition (Eq. 3.9) has $q = 1, 2, 3$ for A, B, C respectively. By comparison of q and q' , it is possible to define the importance of both modes in the determination of the resonance. When $q' = q$, the corresponding mode is the one that decides the phase resonance. When the values of q' for both modes are not equal to the expected integer q , the resonance is determined by the two modes with weighting coefficients. The importance of the mode is linked to the value difference ($|q - q'|$). Having a smaller difference, the corresponding mode is more important in the resonance determination.

Note that the resonance wavelength of C is smaller than $1.28 \mu\text{m}$, where the third mode starts to appear. The parameters for the third mode are: $n_{eff} = 1.562$ and $q' = 1.99$. As q' is far away from the expected $q = 3$, it is not considered for analysis

3. SLOT WAVEGUIDE CAVITY

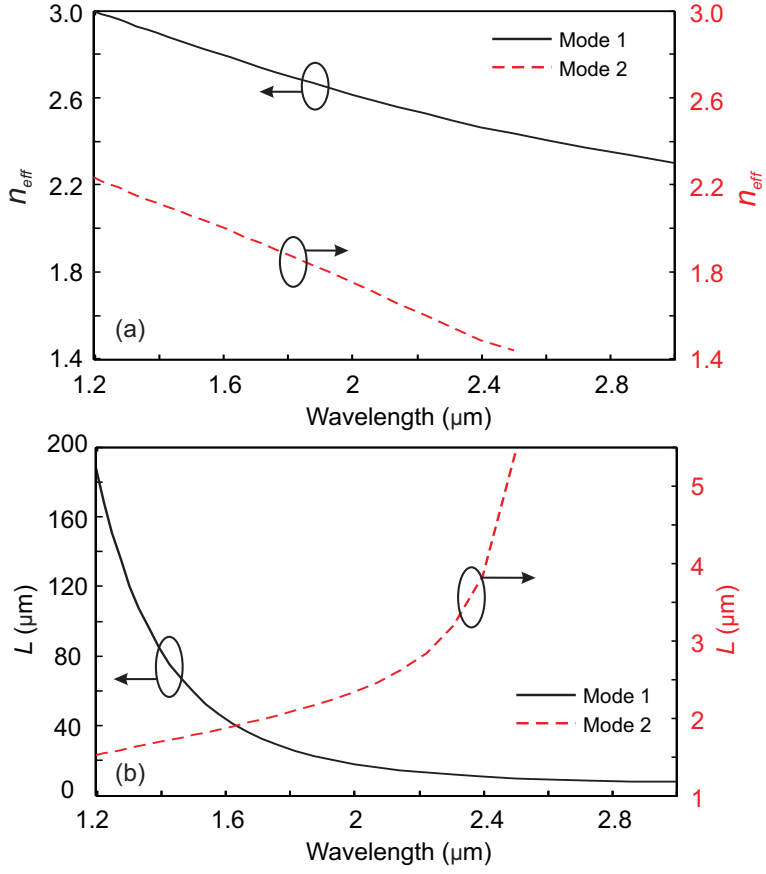


Figure 3.6: Dispersion property of the cavity modes (Fig. 3.5) with parameters: $p = 500$ nm, $l = 800$ nm, $h = 20$ nm, $w = 20$ nm, $h_{\text{SiO}_2} = 100$ nm, $h_{\text{Si}} = 220$ nm. (a) Mode effective refractive index (n_{eff}); (b) Propagation length (L).

in the table.

Table 3.1: Quantitative analysis of the mode parameters at the resonant dips A, B, and C (Fig. 3.2).

λ_r	Parameters	Mode 1	Mode 2
A ($2.412\mu m$)	n_{eff}	2.462	1.483
	$\alpha_s(m^{-1})$	93804	252748
	χ	0.0071	0.0806
	F	1.572	0.601
	q'	1.635	1.0
B ($1.678\mu m$)	n_{eff}	2.759	1.956
	$\alpha_s(m^{-1})$	28140	513452
	χ	0.0011	0.0483
	F	1.866	1.003
	q'	2.633	1.882
C ($1.26\mu m$)	n_{eff}	2.968	2.198
	$\alpha_s(m^{-1})$	6872	637290
	χ	0	0.0332
	F	2.062	1.162
	q'	3.778	2.808

For the resonance A, $q' = 1.635$ and $q' = 1$ for mode 1 and mode 2, respectively, while $q = 1$ for the first order FP resonance. Thus mode 2 is responsible for the resonance. For resonances B and C, none of the modes possess an integer value of q' , meaning that the resonance is a mixture of both modes. Considering the weighting coefficient of each mode in the resonance determination a_i ($i = 1, 2$), $a_1 + a_2 = 1$. For the resonance determination, $q'_1 a_1 + q'_2 a_2 = q$. At wavelength B, $a_1 = 0.158$ and $a_2 = 0.842$. And at wavelength C, $a_1 = 0.198$ and $a_2 = 0.802$. It is clear that a_2 is much larger than a_1 for both wavelength B and C. Mode 2 makes the major contribution to the resonances B and C.

In addition to the decision on resonance position, table 3.1 gives more interesting information from the parameter comparison. The absorption coefficient α_s is compared first. The absorption coefficient α_s for mode 2 is minimum at wavelength A of the three resonances and α_s for mode 1 is maximum at wavelength A. The reason is that from wavelength A to wavelength C, mode 1 tends to distribute more energy in the Si waveguide by decreasing the wavelength, while the mode 2 conversely better confines the light inside the slot. Then, comparing the n_{eff} variation with wavelength, n_{eff} of mode 1 is increased from 2.462 to 2.968 while n_{eff} of mode 2 is increased from 1.483 to 2.198. Evidently, mode 1 is less dispersive than mode 2. Finally, when the importance of mode 2 in the resonance determination is considered, a_2 is compared. The influence of mode 2 is decreased from resonance A to C, since $a_2 = 1.0$ decreases

3. SLOT WAVEGUIDE CAVITY

to $a_2 = 0.802$. It matches with the fact that the influence of the slot array is decreasing by decreasing the wavelength, which then causes the reduction of the transmission dip at C. At wavelength A, light is well coupled to the SWC cavity and achieves a deep transmission dip. On the other hand, mode 2 tends to repel light out of the slot as light wavelength at A is close to its cutoff wavelength $2.5 \mu\text{m}$. This explains a low transmission in Fig. 3.2 at the out-of-resonance wavelength ($2.7 \mu\text{m}$). From wavelength A to C, mode 1 and mode 2 function together to determine the resonance of the cavity. The contribution of the two modes is realized due to the field overlap between the Si waveguide and the slot array, where the Si waveguide plays roles in both the light coupling and the light confinement. Light coupling from the Si waveguide to the slot array depends on the variations of the working wavelength.

Additionally, the shape of the resonance is important. The finesse F , which is introduced in Eq. 3.4, displays the sharpness of the peak. From the equation, F is related to the reflection coefficient at the cavity edge and the absorption in the cavity. F is large for the FP cavity with a high reflective interface and a low absorption coefficient. The finesse F is correlated with the quality factor. The quality factor is one of the most important parameters to define a peak. The definition of the quality factor is $Q = f/\delta f$ where δf is the FWHM (full width half maximum) of the peak. Under the condition that $F \gg 1$, the quality factor of the FP resonance is $Q = f_0 F/\nu_F$, showing that Q is proportional to F . In our device, the strong absorption of modes and small refractive index difference at the edges of the cavity induce a low F . Table 3.1 shows the F values for existing modes and three resonances. The quite influential mode 2 has a very low finesse, in accordance to the low quality factor of the resonances (transmission and reflection spectra in Fig. 3.2). F is slowly increasing with shortened wavelength. This is due to an increased reflectivity at both ends of the Au cavity, as n_{eff} is increased from wavelength A to wavelength C.

The simplified FP model extracts the important properties of the SWC device: the resonance position definition and the sharpness of the resonance. Subsequently, the FP model will be used for further discussion concerning the sensing application of the device. However, as discussed in the spectral analysis, the transmission and reflection spectra are similar to a ring resonator, which is evanescently coupled from a waveguide to a ring resonator. In a ring resonator, the coupling region forms a small part of the resonator and the source waveguide is not influential to the resonance determination. The working principle of the SWC device is more complicated due to the double role of the Si waveguide. In our case, the Si waveguide not only couples the light to the cavity, but also plays a non-negligible role in the resonance determination.

The amplitude of transmission dips is another important parameter to be considered for future characterizations. The amplitude is defined as $A_d = (T_1 + T_2)/2 - T_{min}$ in Fig. 3.2. A_d equals 0.428, 0.294, and 0.062 for dip A, B, and C. Its amplitude is

associated with the coupling strength, which cannot be explained by the FP model. In general, when light is coupled from the Si waveguide to the slot array, the coupling strength is proportional to the field overlap integral between the Si waveguide mode and the slot mode. At wavelength A, the Si waveguide has more energy above its surface, which means more light overlaps with the slot region. Maximum light is coupled for slot confinement and the influence of the Au layer is the strongest for light transmission in Si waveguide. This mechanism is the reason that the coupling strength is maximum at resonance A.

In the following only the second resonance (B) will be considered. Indeed two reasons make this resonance interesting for sensing application. First, considering the shape of each dip, dip A is too large and dip C is too shallow to perform experimental measurements. Compared with dip B, dip A and C are more difficult to detect when the noise of the characterization system is added to the spectrum. Second, the field localization which is mainly centered in the middle of the slot will confer to the structure a more stable response even with fabrication imperfections at both ends of the cavity. For resonance A, the localization of the field close to both ends of the slots has a high demanding on the quality of the cavity edge as simulation. In other words, the fabrication imperfections are expected to alter the transmission dip property more radically at resonance A than at resonance B.

For the section below, the geometrical parameters will be studied for their influences on the optical property, thus improve its performance for sensing applications.

3.3 Parameters Study

Both the Au cavity parameters (the slot width w , the Au thickness h , the cavity length l and the period p) and the waveguide dimensions (the Si thickness h_{Si} and the top SiO_2 layer thickness h_{SiO_2}) are set as variables in this section.

According to the FP model, the phase condition in Eq. 3.9 explains the transmission dip position. Inside the cavity, the effective refractive index n_{eff} is a combination of two modes (see Fig. 3.5) supported by the structure, while mode 2 is the principal one. The device geometry can affect the resonance position λ_d via n_{eff} or the cavity length l variation. The Au cavity geometry will definitely alter the supported mode profile, and thus the spectrum. Besides λ_d , the amplitude of the transmission dip A_d is controlled by the amount of the coupled light to the Au cavity. Clearly, since the waveguide dimensions play a direct role on the evanescent wave intensity above the waveguide surface, they are likely to play an important part on the coupling strength.

The resonance position λ_d , the amplitude of the transmission dip A_d , and the electric field intensity I_{max} are taken into account for the optical property analysis. Herein I_{max}

3. SLOT WAVEGUIDE CAVITY

is shown in Fig. 3.3, meaning the peak intensity $|E|^2$ in the middle of the slot. Note that the incident power of the electromagnetic wave to the periodic unit of the Si waveguide is kept constant of 1 Watt for all calculations. I_{max} proves the field localization strength in the slot, determined by the amount of the coupled light and the field confinement ability of the slot. Based on the setting $w = 20$ nm, $h = 20$ nm, $l = 800$ nm, $p = 500$ nm, $h_{Si} = 220$ nm, $h_{SiO_2} = 100$ nm, each parameter is varied separately while the others are invariant.

3.3.1 Slot width w & Au thickness h

Veronis and Fan [104] have shown that the guided subwavelength plasmonic mode supported by a slot in a thin metal film depends strongly on the slot geometry itself. Furthermore, the FP-like resonance, which plays a role in the resonance position determination, enhances the light coupling and then the field localization in the slot. Therefore, the cavity geometry can easily vary the λ_d position of resonance B, with regard to the mode effective refractive index n_{eff} .

Figure 3.7 shows the λ_d position (squares), the normalized I_{max} (circles), and the dip amplitude A_d (stars) in variation with (left side) the slot width w ranging from 5 nm to 50 nm and (right side) the Au thickness h in the range of 5 nm to 50 nm. Each curve is mathematically fitted from discrete calculated points. It is observable that the three most important properties (λ_d , A_d , and I_{max}) are a function of the slot size, especially when the slot is quite small ($w, h < 20$ nm). For $w, h = 0$, there is no periodic slot array or no Au film on the Si waveguide. Since no resonant transmission dip exists, they are not then considered.

λ_d is first discussed. At $w = 5$ nm and $h = 5$ nm, λ_d is maximum within the calculated range. Smaller values for w and h have not been simulated because there is no current interest in fabricating such dimensions. Verified by Veronis and Fan [104], the supported mode of a smaller air slot has a stronger field confinement in the slot region and more energy loss in the Au layer. In the phase condition (Eq. 3.9), the phase change χ can be disregarded from the details extracted in table 3.1. The effective refractive index n_{eff} of both mode 1 and mode 2 (see Fig. 3.5) are modeled to check their relation with the slot geometry. Results are shown in Fig. 3.8 for constant wavelength in the vacuum $1.55 \mu\text{m}$. n_{eff} of mode 2 apparently decreases with the slot width or Au thickness, while n_{eff} of mode 1 is almost constant after $w, h \geq 7.5$ nm. Since mode 2 is the dominant mode in the cavity, the λ_d position follows the change of n_{eff} for mode 2. As a result, λ_d exponentially blue shifts by the increase of w or h .

In contrast to λ_d , I_{max} and A_d show different reactions to w and h variations. There exists optimum values for A_d and I_{max} when h is varied. Two aspects should be taken into account for the I_{max} and A_d discussion: resonance position induced coupling strength dependence and the field confinement ability of the slot. A_d shows

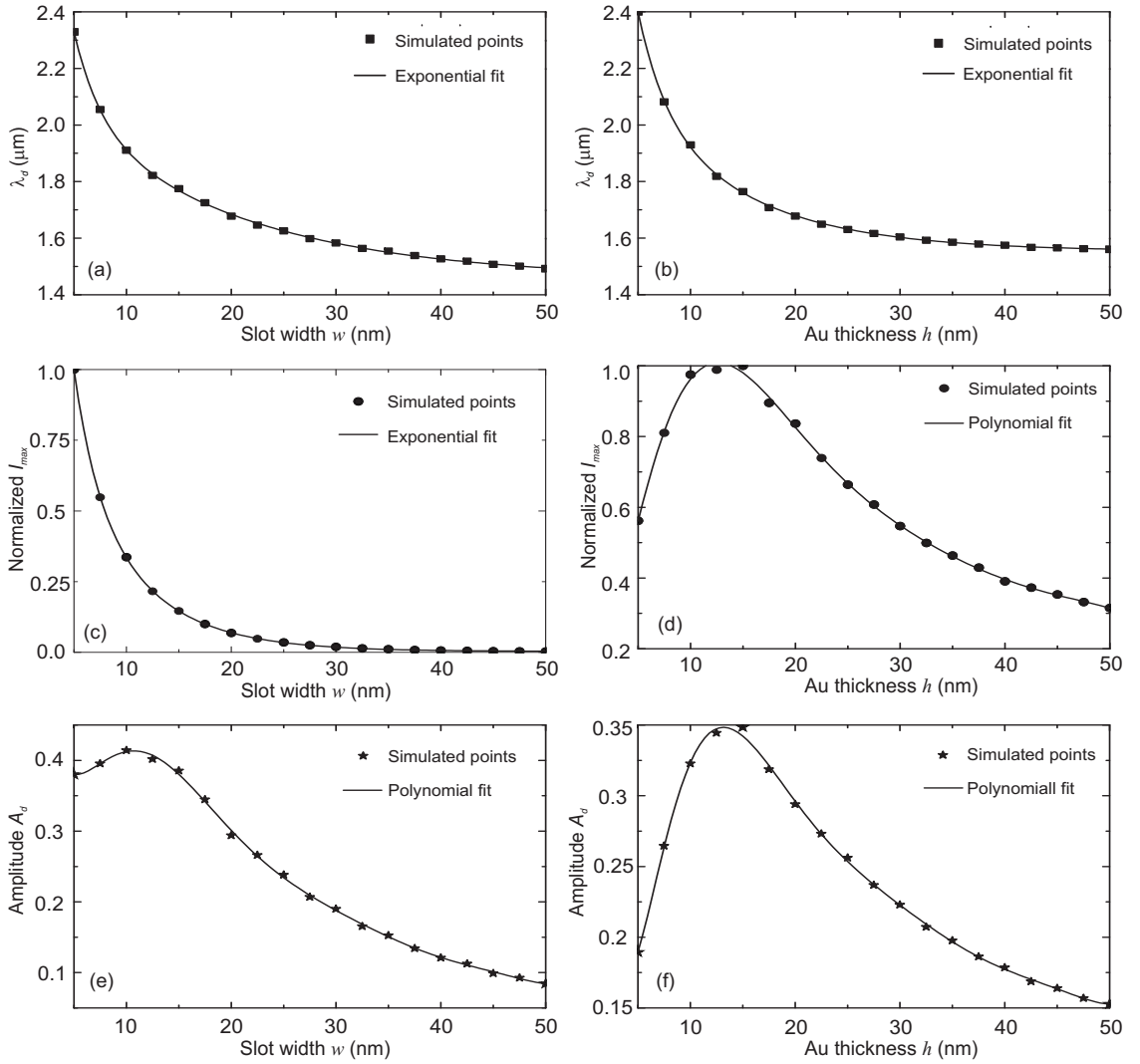


Figure 3.7: The resonance position λ_d (squares), the normalized electric field intensity I_{max} (circles), and the dip amplitude A_d (stars) as a function of the slot width w (left side) and the Au layer thickness h (right side) of the cavity. Other parameters are the same as in Fig. 3.2.

3. SLOT WAVEGUIDE CAVITY

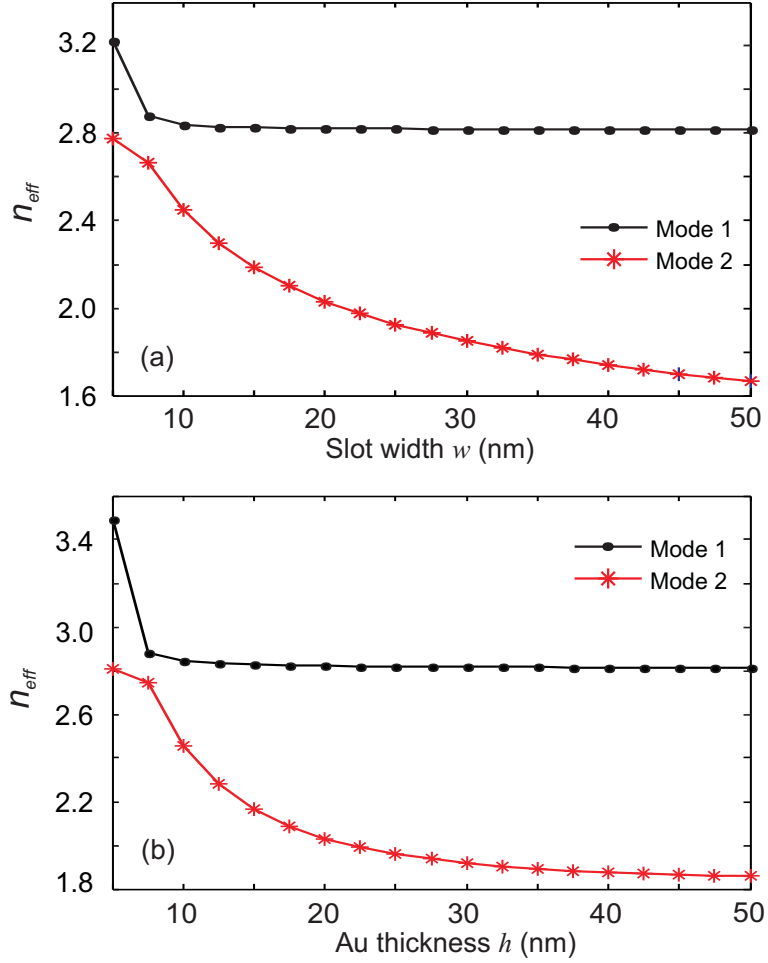


Figure 3.8: Effective refractive index n_{eff} variation of the supported modes in the slot structure of Fig. 3.7 with: (a) the slot width (w); (b) the Au thickness (h). The calculation is made for the fixed wavelength $1.55 \mu\text{m}$.

essentially the coupling strength between the Si waveguide and the slot array. I_{max} is a combination of the amount of coupled light and the field localization ability of the slot.

When w is increased, the resonance position is blue shifting. For $w \geq 10$ nm, the coupling strength is decreasing as the field tends to be distributed in the Si waveguide and the field confinement ability of the slot decreases. Both A_d and I_{max} decrease with the w increment. For $w < 10$ nm, the amount of light confined in the tiny slot is small even though the field overlap is large. A_d is increasing somewhat with an increase in w . I_{max} at $w = 5$ nm shows the apparent light localization in the slot even though the total amount is not an optimum.

For Au thickness variation, A_d is low at $h = 5$ nm, even though considering the large amount of light localized above the Si waveguide surface. The reduced value of A_d indicates that the impact of the slot array on the transmission is small when the Au film is much thinner than the light penetration depth. Nevertheless, the blue shift of λ_d results in the field localization in the Si waveguide and A_d decreases after its optimum value at $h = 15$ nm. At the same time, I_{max} is apparently decreasing with the Au thickness due to the decrease of the amount of coupled light.

The w and h size is optimized at 10 nm and 15 nm respectively. The design will be chosen as close to these values as possible in order to optimize the transmission spectrum and field localization. On the other hand, the device fabrication technique limits the slot size. The Au thickness is chosen to be 20 nm from experience and the slot width is considered to be 30 nm due to the fabrication tolerance of the available techniques.

3.3.2 Cavity length l

Figure 3.9 shows the position of the resonance B (λ_d), normalized $|E|^2$ in the center of the slot (I_{max}) and the amplitude of the transmission dip (A_d) in relation to the cavity length (l), varying from 650 nm to 1100 nm. Within this length range, λ_d still locates in the spectral range of interest ($1.3 \mu\text{m} \sim 2.4 \mu\text{m}$). λ_d is increasing with the cavity length l . Note that both ends of the Au cavity act as reflection interfaces in the FP model. When the reflection phase shifts χ at the interfaces are ignored, the phase condition Eq. 3.9 can be transformed to: $\lambda_d = n_{eff}l$ for resonance B, where l is the cavity length and n_{eff} mainly depends on mode 2. λ_d is linearly related to l where n_{eff} is the slope. For $1.47 \mu\text{m} < \lambda_d < 2.0 \mu\text{m}$, n_{eff} of mode 2 is inversely decreased with wavelength from 2.07 to 1.75 (see Fig. 3.6). However, the slope variation is not obvious from the λ_d graph with the l variation.

For the graph of A_d , the coupling strength to the slot array increases due to the prolongation of the coupling length and the red shift of the resonance position at the beginning. After l reaches $1 \mu\text{m}$, it indicates saturation for this amount of coupled light.

3. SLOT WAVEGUIDE CAVITY

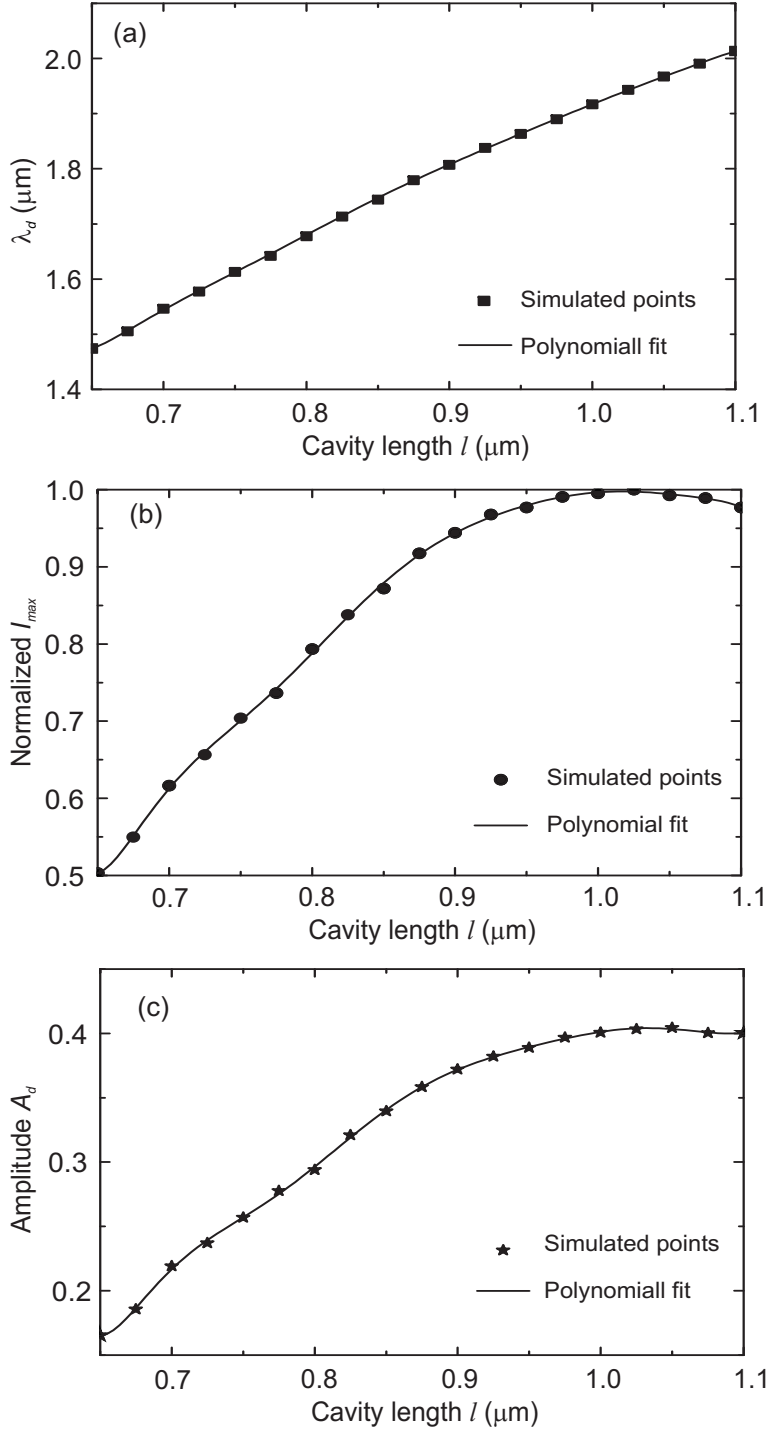


Figure 3.9: Resonance position λ_d (squares), the normalized electric field intensity I_{max} (circles), and the transmission dip amplitude A_d (stars) as a function of the cavity length l . Other parameters are: $w = 20$ nm, $h = 20$ nm, $p = 500$ nm, $h_{Si} = 220$ nm, $h_{SiO_2} = 100$ nm.

Correspondingly, the I_{max} is enhanced at the beginning by the improved coupling. Then I_{max} begins to decline from the coupling saturation point, since the electric field distributes over the whole cavity.

In our design, the cavity length is convenient to be used for tuning the λ_d position of the resonance around $1.55 \mu\text{m}$. Indeed, the length of the cavity is one of the least difficult parameters to control during fabrication.

3.3.3 Period p

The period p is another parameter considered to influence the transmission spectrum and the field confinement of the device. The field interaction among adjacent slots in the Au cavity varies the resonance position λ_d (squares), the transmission dip amplitude A_d (stars), and the field confinement I_{max} (circles) as shown in Fig. 3.10. According to the phase condition of the FP model, λ_d follows the variation of n_{eff} in the cavity. Calculations on n_{eff} have been made at a fixed wavelength $\lambda = 1.55 \mu\text{m}$. The effective refractive index of mode 1 slowly decreases from 2.832 to 2.818, which is insignificant. The augmentation of n_{eff} of mode 2 by enlarging the value of p is shown in Fig. 3.11. Here it is understood that the field interaction among adjacent slots decreases n_{eff} . As a result, n_{eff} for $p = 250 \text{ nm}$ is minimum and its value saturates when p is large enough since the field interaction decreases with the slot separation. The difference of growth shape between λ_d and n_{eff} graphs is caused by the dispersion property of n_{eff} , the influence variation of mode 2, and the phase shift χ deviation.

The A_d graph indicates the enhancement of the energy coupled to the slot array with p . When p is small, the interaction among slots decreases the λ_d position and thus decreases light coupling to the slot. From a comparison of graphs, the growth of n_{eff} and A_d is similar. Due to the enhanced coupling, the graph of field localization I_{max} also shows an enhancement as a function of p .

The value of p is chosen to be 500 nm for the fabricated device. Even though with $p = 600$, a higher coupling efficiency and a better field confinement can be achieved, the choice of p should in practice be smaller. The reason is that illuminating light on the periodic structured Au film is diffracted on the Au/air interface. Furthermore, the excitation of the surface plasmon prevents light coupling to the slots so that the transmission dip deteriorates. For $p = 600 \text{ nm}$, this occurs at around $\lambda = 1.63 \mu\text{m}$. It is close to the $1.55 \mu\text{m}$ where the transmission dip is expected. For $p = 500 \text{ nm}$, the surface plasmon excitation exists around $1.43 \mu\text{m}$, while the A_d and I_{max} still keep an elevated value.

3.3.4 Waveguide

Because the field coupling from the Si waveguide to the Au cavity depends on the overlap integral of the evanescent wave, the dimensions of the Si waveguide are very

3. SLOT WAVEGUIDE CAVITY

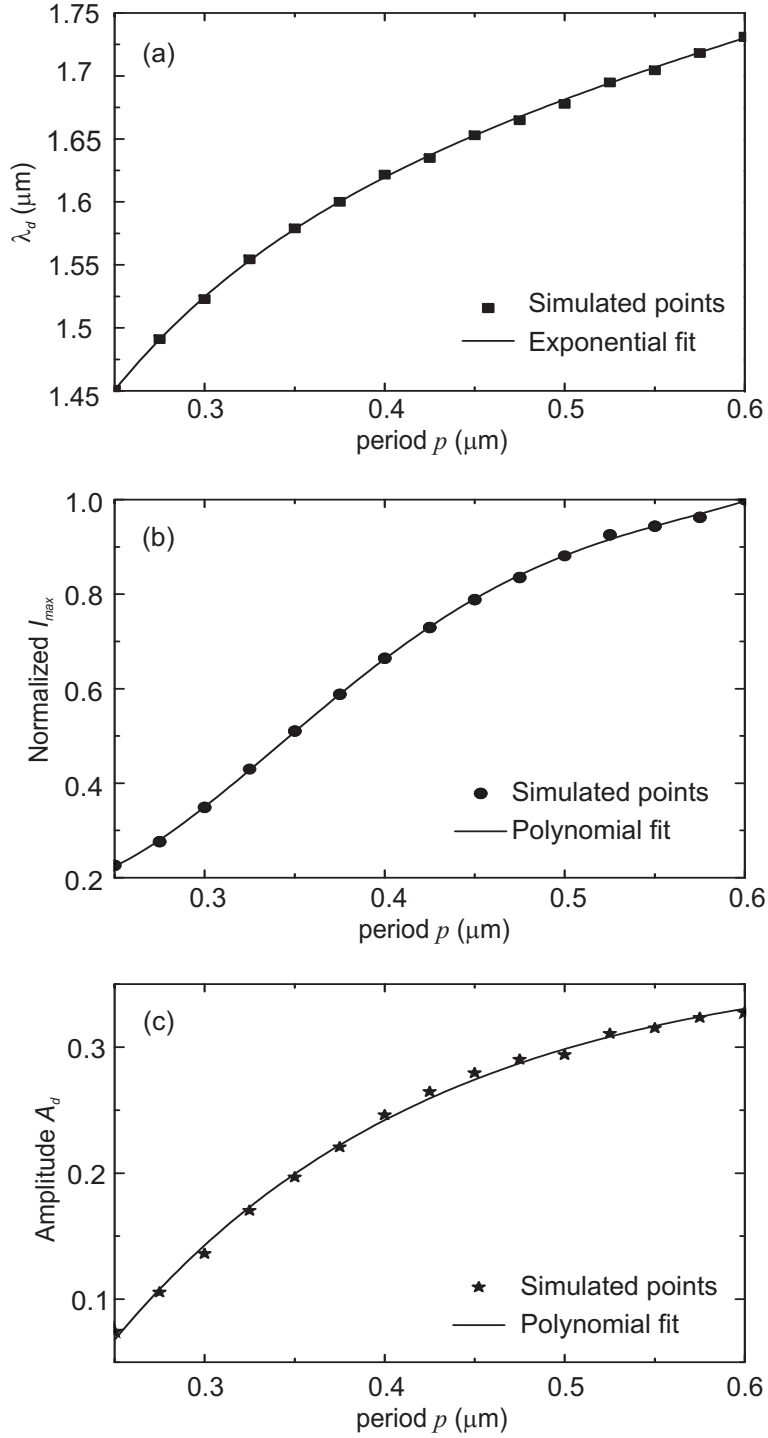


Figure 3.10: Resonance position λ_d (squares), the normalized electric field intensity I_{max} (circles), and the transmission dip amplitude A_d (stars), in response to a variation of the period p of the cavity. Other parameters are: $w = 20$ nm, $h = 20$ nm, $l = 800$ nm, $h_{Si} = 220$ nm, $h_{SiO_2} = 100$ nm.

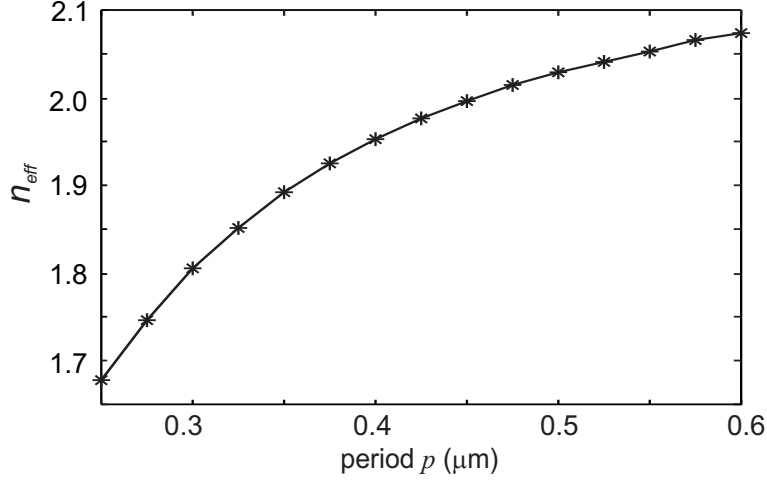


Figure 3.11: Effective refractive index n_{eff} variation of the mode 2 in the slot structure of Fig. 3.10, in response to a variation of the period p . The calculation is made for the fixed wavelength $1.55 \mu\text{m}$.

influential for the final device properties. Especially for the amount of the coupled light, the waveguide size drastically alters the evanescent wave intensity above the surface.

The variations of the λ_d position (squares), the normalized I_{max} (circles), and the transmission dip amplitude A_d (stars) with the thickness of the top SiO_2 layer (h_{SiO_2}) (right side) and the Si layer (h_{Si}) (left side) are shown in Fig. 3.12. The Au cavity geometry is fixed to be the same as in Fig. 3.2. The three parameters reveal their distinctive dependence on h_{Si} and h_{SiO_2} .

λ_d clearly changes with h_{SiO_2} when h_{SiO_2} is small. It is exponentially blue shifting by the increase of h_{SiO_2} . When h_{SiO_2} is larger than 80 nm, the λ_d position is almost invariant. Relatively, the influence of the Si layer thickness h_{Si} on λ_d is weaker than h_{SiO_2} . λ_d is continuously increased with the value of h_{Si} . From the above analysis, λ_d is determined by n_{eff} in the FP cavity. The effective refractive indices of mode 1 and mode 2 are displayed in Fig. 3.13 as functions of h_{Si} (left side) and h_{SiO_2} (right side). Comparing the λ_d profile with n_{eff} of mode 1 and 2, mode 2 is established to be the principal mode in the resonance determination for both h_{Si} and h_{SiO_2} modifications. Note that n_{eff} of mode 2 undoubtedly is a function of the slot substrate. When the slot substrate is replaced by a higher refractive index material, the effective refractive index of the supported mode is required to be larger to avoid light leakage in the substrate. It is reasonable that the increase of h_{SiO_2} lowers n_{eff} and the increase of h_{Si} raises the n_{eff} value. The fluctuation of λ_d to h_{SiO_2} is greater than to h_{Si} .

For A_d and I_{max} graphs with enlarging h_{Si} , they indicate that a declining amount of light is coupled to the slot due to the decrease of the evanescent wave intensity on the Si waveguide surface, thus the amount of the coupled light and the field intensity

3. SLOT WAVEGUIDE CAVITY

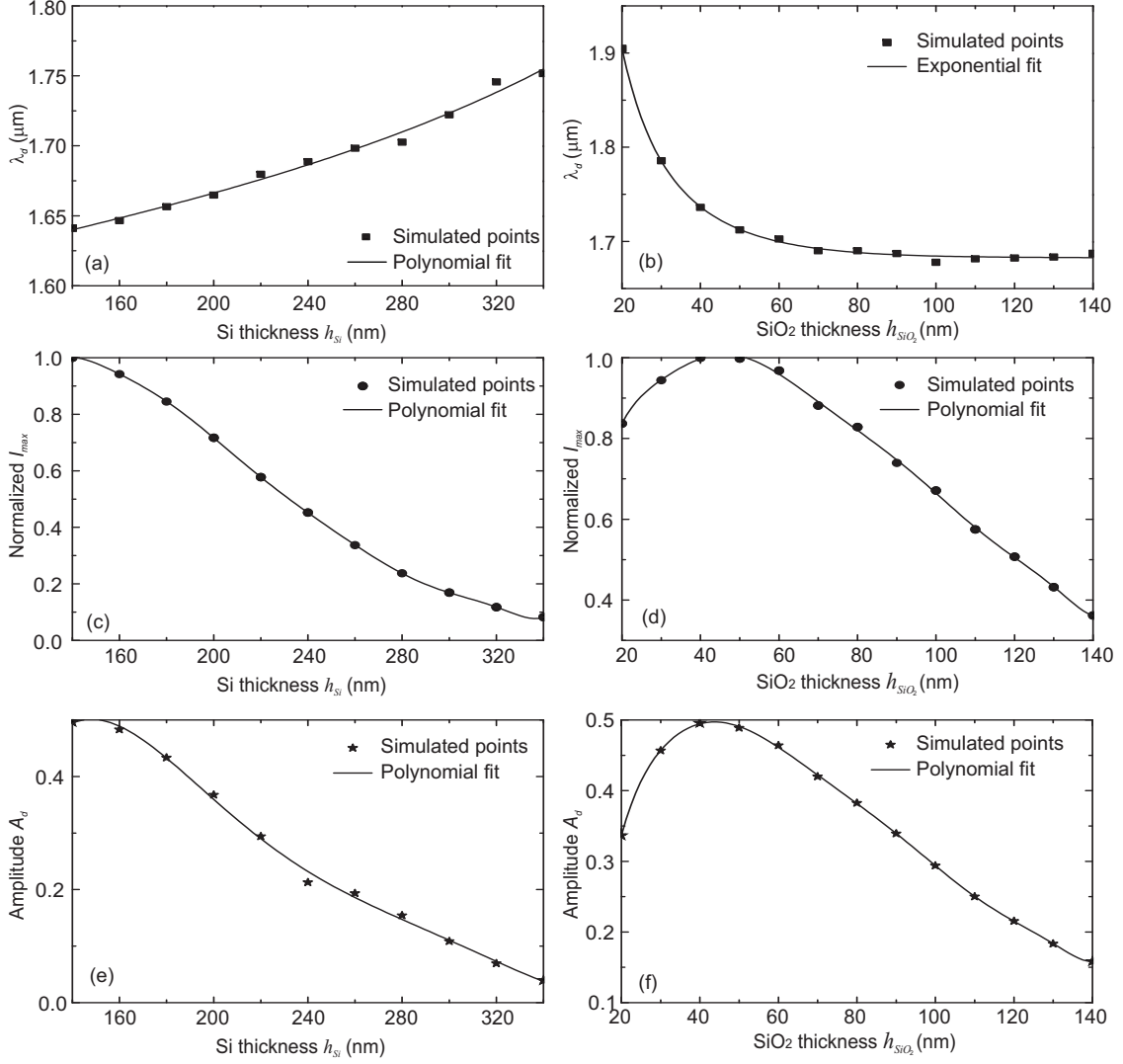


Figure 3.12: The resonance position λ_d (squares), the normalized electric field intensity I_{max} (circles), and the transmission dip amplitude A_d (stars) as a function of the Si thickness h_{Si} (left side) and the SiO₂ thickness h_{SiO_2} (right side) of the waveguide. Other parameters are the same as in Fig. 3.2.

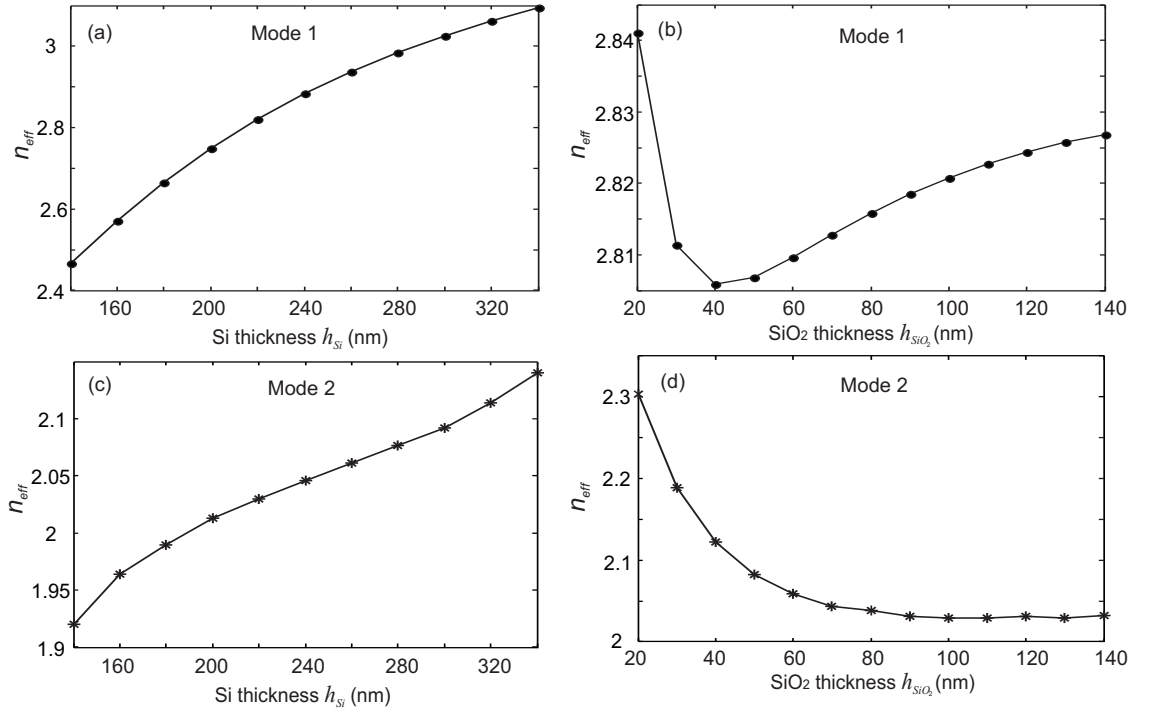


Figure 3.13: Effective refractive index of the slot supported modes as a function of the Si thickness h_{Si} (left side) and the SiO₂ thickness h_{SiO_2} (right side) of the waveguide. The calculation is made at a the fixed wavelength of $1.55 \mu\text{m}$.

3. SLOT WAVEGUIDE CAVITY

in the slot. For h_{SiO_2} variation, A_d and I_{max} have a similar profile. They reach an optimum value when $h_{SiO_2} = 50$ nm. At $h_{SiO_2} = 20$ nm, the coupling strength is in a relative sense lower, resulting from the repelling of light to the substrate by the Au cavity. With such a thin SiO_2 layer, the Au cavity is not effectively confining light inside the slot and the light becomes easily leaky to the Si layer. It is also the reason that there is no transmission dip when the slot is deposited on the high RI Si substrate, which is the $h_{SiO_2} = 0$ case. Afterwards, the coupled light is enhanced by improved light confinement in the slot. When $h_{SiO_2} > 50$ nm, A_d and I_{max} are decreasing with the decline of the evanescent wave overlap on the slot region.

From the waveguide design, the amount of light coupled to the slot array A_d needs to be optimized. At the same time, the thickness of the Si layer must conserve the property of an efficient light propagation medium. Ideally, the infinitely extended Si layer has no cutoff for our spectral range. However, the fabrication imperfections induce light losses and may lead to inefficient light propagation in the Si waveguide. h_{Si} is designed to be thick enough to well confine the light inside the waveguide. For the spectral range around $1.55 \mu m$, $h_{Si} = 220$ nm is chosen and h_{SiO_2} is 100 nm.

3.3.5 Summary

The above analysis presents the variation in position (λ_d), the shape of the transmission dip (A_d), and the field intensity (I_{max}) as a function of the different geometrical parameters of the slot waveguide cavity.

It is well known, and we just have demonstrated that small variations in the geometry involve dramatic changes in the spectral response of a nanostructure. Unfortunately, it is almost impossible to exactly fabricate the structure which has been modeled. Therefore, a trade-off must be found between the ideal theoretical parameters and the fabrication issues.

Considering the theoretical study and the experimental (fabrication and characterization) issues, we can make the following conclusion:

- $h_{Si} = 220$ nm, to confine light well in the Si waveguide. Even though a thinner Si layer can achieve a better amplitude of the resonance, the imperfections at the interfaces will degrade the propagation efficiency.

- $h_{SiO_2} = 100$ nm. $h_{SiO_2} = 40$ nm presents a larger resonance amplitude. But at the same time around this value, λ_d is varying significantly. It is therefore preferable to choose a value which may allow some fabrication variations without drastically changing the resonance position.

- $p = 500$ nm. A large value of the period is required (Fig. 3.10) to have good coupling and confinement of light in the slot cavity, but the coupling between the mode

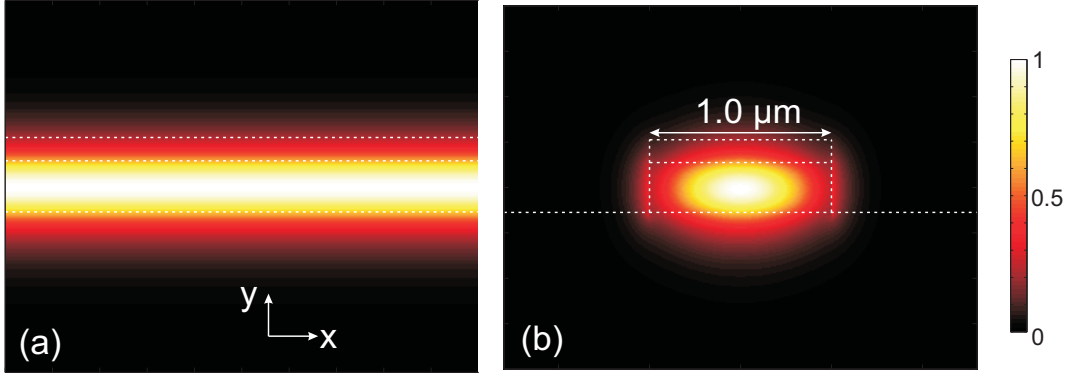


Figure 3.14: Electric field distribution of the launched mode with (a) periodic boundary in the x direction; (b) finite waveguide with 1 μm . The dotted lines show the outline of the Si waveguide layers.

and the surface plasmon has to be avoided. Indeed the surface plasmon may have a negative effect on the guided mode [107].

- $w = 30 \text{ nm}$ and $h = 20 \text{ nm}$ have been chosen for fabrication issues. Indeed, $w = 10 \text{ nm}$ and $h = 15 \text{ nm}$ are ideal but impossible to obtain, simultaneously. w and h are linked during the fabrication process and the chosen values are the limit of our fabrication techniques.

- $l = 700 \text{ nm}$ or 800 nm to set the resonance position around $\lambda = 1.55 \mu\text{m}$.

3.3.6 Discussion of the finite structure

From a practical view point, the device will be finite in the x direction. From infinite width modeling to the realization based on finite width, the incident light distribution is varied depending on the waveguide width. The electric field ($|E|$) distribution is compared in Fig. 3.14 between the model with the periodic boundary and the one with a finite width, corresponding to two periods (1 μm). The waveguide is composed of a 220 nm thick Si layer and 100 nm SiO_2 above the SiO_2 substrate. Air surrounds the waveguide. It is clear that the finite width squeezes the light to the center of the waveguide. When the waveguide is widened, the field is extended to both sides of the waveguide. The inhomogeneity of the field distribution in x direction causes varied coupling strength for different slots. Thus each slot plays a varied role on the transmission resonance determination.

Additional calculations have been undertaken to verify the optical response variation of the device for different waveguide widths. Figure 3.15 shows the transmission spectra for waveguides with width variation (width = period $p \times$ slot number). In this model, perfectly matched layers (PML) are used in the x direction to absorb propagating waves

3. SLOT WAVEGUIDE CAVITY

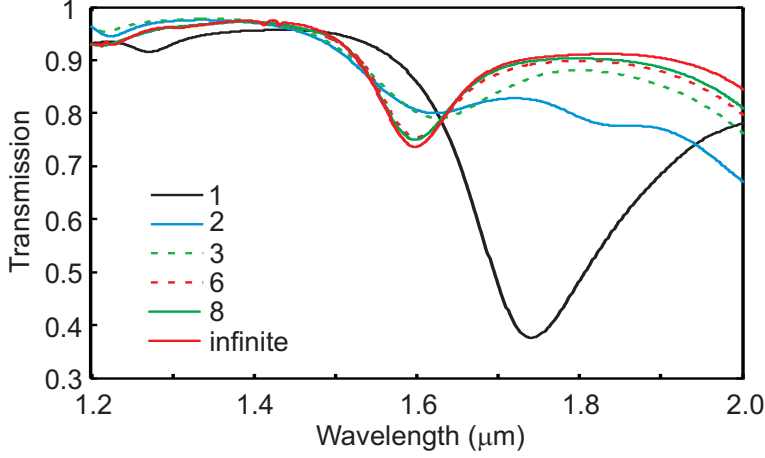


Figure 3.15: Transmission spectra for varied waveguide widths (period $p \times$ slot number).

instead of periodic boundary conditions. For the single slot device, the transmission dip is apparent due to field squeezing to the center of the waveguide where the slot is located. Thus light is more efficiently coupled to the slot cavity and the amplitude of the transmission dip is enhanced. Nevertheless, the 500 nm width demands a high quality of the waveguide to avoid significant light propagation loss. It is therefore preferable to utilize a larger device width. With two periods of the width, the two slots have a low coupling efficiency because they are located away from the high energy center of the Si waveguide. When the number of slots increases, the transmission spectrum evolves to be close to that of the infinity case. For a slot number higher than 8, a difference of only 2% is observable on the transmission dip compared to the case of the infinite structure. Experimentally, the fabricated structure involves 30 slots, which will follow the simulation results for the infinite structure, theoretically. The chosen width (15 μm) is adapted to the modal field diameter (about 10 μm) of the single mode fiber SMF28 at wavelength 1.55 μm .

With 15 μm in width, the Si waveguide supports multiple modes which will influence the transmission spectrum. In theory, the basic order of the supported modes (shown in Fig. 3.14(b)) is required for characterization. At the same time, this mode is mainly excited from the mode overlap integral with that of the single mode fiber. However, higher order modes may also be excited by waveguide imperfections. These higher order modes may cause modifications of the transmission dip. Depending on the field distribution in relation to slots, certain modes shift or reduce the transmission dip. Accordingly, the desired transmission dip may be widened or multiple dips appear, linked to the the excitation of corresponding higher order modes.

3.4 Fabrication

The device is fabricated at the Center of MicroNanoTechnology (CMI, EPFL) by Armando Cosentino from the OPT Laboratory, EPFL. The precision and quality control of each step determines the final properties of the fabricated device. The fabrication process follows the sequential steps listed below:

1. The surface of the $\langle 100 \rangle$ oriented Si wafer is wet oxidized in order to create a $3\text{ }\mu\text{m}$ -thick SiO_2 layer. As it is the substrate of the device, the roughness of the surface is one of the key points to guarantee successful subsequent steps. The oxidation is processed on a double side polished wafer and the root mean square of the roughness is 1.2 nm .
2. Amorphous Si (220 nm) is deposited by means of low temperature ($T_{temp} < 560^\circ\text{C}$) LPCVD (Low Pressure Chemical Vapor Deposition) [108] on the SiO_2 layer. In advance of LPCVD, the RCA (Radio Corporation of America) cleaning is performed to remove contaminants.
3. The substrate is dehydrated with an oxygen plasma cleaning for 2 minutes. Then a SiO_2 (100 nm) layer is deposited by room temperature sputtering while the oxygen flux assists. The achieved SiO_2 layer is amorphous.
4. Once the substrate is dehydrated on a 180°C hot plate and cooled down, positive e-beam resist ZEP520A, which is diluted in Anisol with a $1 : 2$ ratio of ZEP520A:Anisol, is spin coated for 70 nm thickness. The thickness of the resist is controlled by the spinning speed. Then the slot array pattern on ZEP520A is processed by e-beam lithography and development in n-amyl-acetate liquid. The mask used here has a high resolution of 2 nm to attain the desired 30 nm slot width. The substrate should be gently cleaned by the “PMMA descum” recipe after the photoresist development.
5. The Au (20 nm) layer is deposited by e-beam evaporation. Note that a layer of 1.5 nm titanium (Ti) is used to increase the adhesion between Au and the SiO_2 layer.
6. The slot array pattern is transferred from ZEP520A to Au layer by the lift-off method [109] in the acetone soak bath.
7. Positive photoresist AZ 1512 is deposited in a $1.1\text{ }\mu\text{m}$ thick layer. A second lithography is carried out for waveguide etching.
8. The waveguide ($15\text{ }\mu\text{m}$ width) is formed by reactive ion etching (RIE) on the Au layer and the waveguide layers (SiO_2 layer + Si layer). Various etching recipes are chosen for different materials etching.

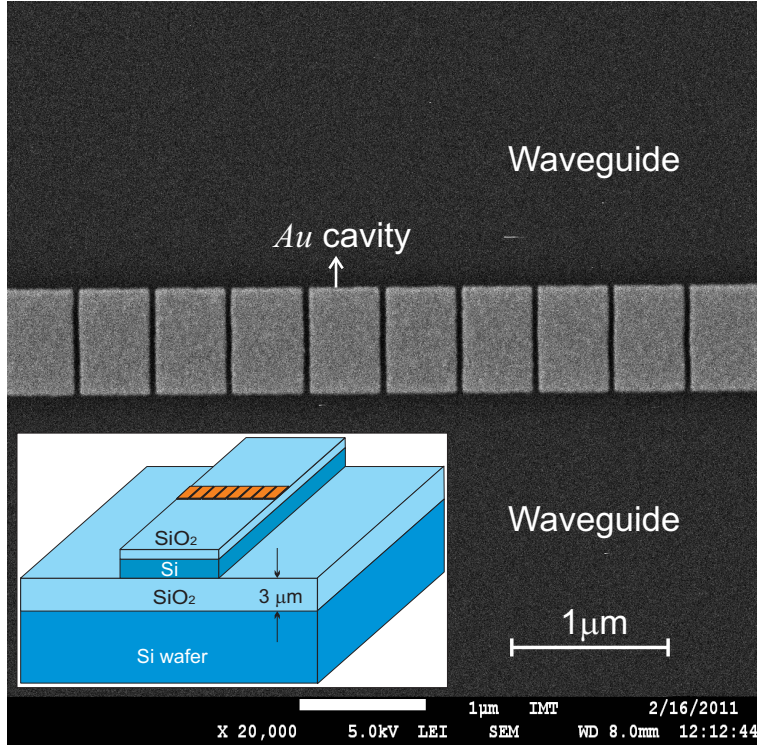


Figure 3.16: Top view of the Au cavity by scanning electron microscopy (SEM). The inset is the scheme of the fabricated device.

9. The photoresist is stripped off the sample by acetone and isopropanol (IPA) in sequence.

Note that during step 4, ZEP520A (Nippon Zeon Co.) [110] e-beam resist is used due to its high sensitivity to electron bombardment and its ability to achieve a high resolution and a high aspect ratio. Figure 3.16 shows the SEM image of the Au cavity (a scheme of the full device is in the inset of Fig. 3.16).

3.5 Characterization and Results

3.5.1 Set-up

The scheme for the characterization set-up is shown in Fig. 3.17. Light from a supercontinuum (SC) white light source (Koheras, SuperK Extreme) is coupled to the waveguide via a cleaved single mode optical fiber at 1550 nm (SMF 28). The output signal is collected by another cleaved fiber, which is connected subsequently to an optical spectrum analyzer (OSA) (Ando AQ-6315B). The combination of the OSA and the SC enables to obtain a whole spectrum capture in a single measurement. The device

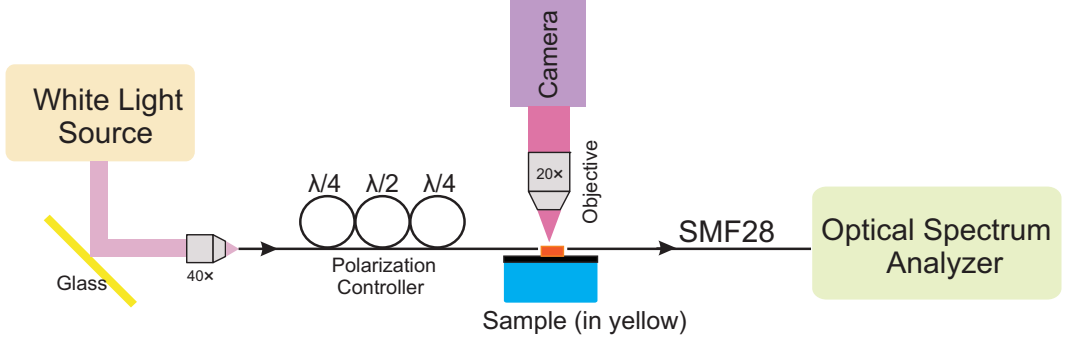


Figure 3.17: Schematic view of the characterization set-up.

has been designed to place alternate waveguides with and without nanostructures on the same sample. Therefore, a normalization of the cavity spectrum can be performed.

In the setup, the SMF 28 single mode fiber has an operating wavelength from 1260 nm to 1625 nm [111]. The SC light source provides a high power and unpolarized Gaussian beam from a single mode photonic crystal fiber with a spectral range extending from 400 nm to 2400 nm. The measurement wavelength range of the OSA is from 350 nm to 1750 nm with a wavelength resolution of 0.05 nm. Thereby the spectral range of the setup system is limited by the single mode fiber having a wavelength in vacuum of 1260 nm to 1625 nm. The fiber polarization controller functions to convert the unpolarized beam into the desired light having a linear polarization. Since the SWC device only functions with TM polarization, the polarization of the incidence can be verified by the amplitude of the transmission dip.

During the experiment, the alignment between the waveguide and the cleaved fibers is finely tuned by Newport ULTRAlign precision fiber optic positioners. The top camera helps to position the sample and the cleaved fibers. For the vertical alignment of fiber and Si waveguide, the injection and collection efficiency are ultra sensitive to their relative positions.

Note that to obtain a large and uniform spectrum from the white light source, the power of the pumping laser inside the source has to be set at a high value. The maximum power of the source is about 4 W, which corresponds to 2 mW/nm. When the laser is pulsed, it may cause some damage to the nanostructure, optical fibers or optical elements. Such high power is not needed to perform the measurement of the spectrum. In order to avoid such risks, we have placed a glass plate to align the beam with microscope objective during the injection into the optical fiber. Only 4% of the initial power is used during the experiment.

3. SLOT WAVEGUIDE CAVITY

3.5.2 Results

The experimental transmission spectra are shown in Fig. 3.18 for comparison with the simulation results. Each experimental result (black solid curve) is filtered by Fourier transform (red dashed curve) to remove parasitical oscillations. The parasitical oscillations are considered to come from incidence noise (representing light injection to the substrate, and so on), light scattering, and Fabry-Pérot resonance within the Si waveguide. Following the filtration process, we consider the normalized transmission, which corresponds to the ratio of the measured spectrum through the cavity to the waveguide without a cavity. The samples have been specially designed to have alternatively, side by side, a waveguide with and without a cavity. Note that the coupling efficiency varies somewhat from one waveguide to another, depending on the separation and vertical alignment between the fiber and the waveguide. It means that the shape of the spectra are normalized but not the amplitude.

Two different cavities have been compared, having different cavity lengths: $l = 700$ nm and $l = 800$ nm. One can first observe the presence of the dip in the experimental transmission spectra, which confirms the theoretical predictions: the experimental and calculated full width at half maximum ($\delta\lambda$) of the dips match and the dip shifts $\Delta\lambda$ due to the length variation are of the same order of magnitude. The dip positions for both $l = 700$ nm and $l = 800$ nm match with theory, even though with certain deviations. Figure 3.7 shows that a very small variation of the geometrical parameters may generate a large modification of the dip position λ_d , especially true for the slot dimensions. In our case, a variation of 1 nm in w causes a dip shift of 8 nm and a variation of 1 nm in Au thickness h moves the dip by 10 nm. The fabrication process allows an utmost resolution of 2 nm in w and h . Taking all the information into account, the theoretical spectra have been verified experimentally.

3.6 Sensing Application

According to the previous study, the resonance position λ_d is caused by the FP-like resonance in the Au cavity. The resonance wavelength is tunable within a wide spectral range by modifying the geometry of the device. This tunability is realized via their effect on the effective mode refractive index (n_{eff}) or the length (l) of the FP cavity. Considering a fixed geometry, one way to modify the effective refractive index n_{eff} of the guided mode inside the slot is to directly vary the refractive index (RI) of the medium inside and above the cavity. It is understandable that a variation of the medium alters the light reflection at the Au edge and thus the field distribution in the slot. Based on the FP-like resonance, the λ_d position is shifted in the transmission spectrum. Consequently, one is able to determine the RI variation of the material by measuring the resonance position, and the device is applicable as an RI sensor. The

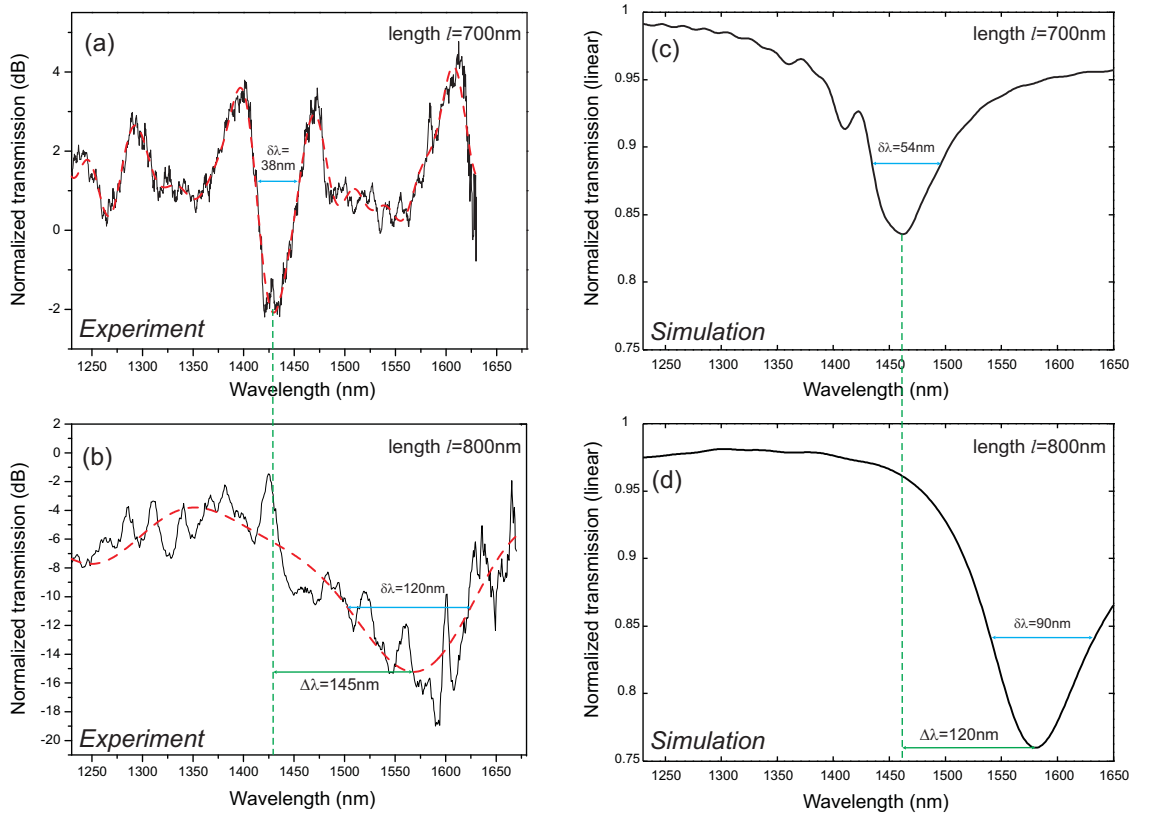


Figure 3.18: Experimental results (a) and (b) for different cavity lengths ($l = 700\text{ nm}$ for (a) and (c); $l = 800\text{ nm}$ for (b) and (d)) in comparison with the simulation spectra (c) and (d).

theoretical expectation, the experimental results, and the performance evaluation are now to be discussed.

3.6.1 Theoretical expectation

Taking into account the fabrication issues, the slot width is chosen to be 30 nm. The other parameters are $p = 500$ nm, $l = 700$ nm, $h = 20$ nm, $h_{Si} = 220$ nm, $h_{SiO_2} = 100$ nm. Figure 3.19 (a) gives transmission spectra for air, water ($n_{H_2O} = 1.318$) and ethanol ($n_{C_2H_5OH} = 1.354$) as analytes. The transmission resonance is red shifting with the increase of the RI of the analyte. Figure 3.19 (b) shows the resonance position λ_d in relation to the material RI ranging from 1.0 to 1.4. With an RI increment of 0.05, the calculated points are exponentially fitted, which is close to a linear curve. Within a smaller RI range, it will be recalculated with a smaller RI step for better precision. Moreover, the large RI range makes the device a sensor for a wide domain of analytes.

Sensitivity is one of the most useful characteristics of a sensor. It has been defined in chapter 2 (Eq. 2.1). In mathematical analysis, the sensitivity is the ratio of the λ_d shift over the RI change. From the phase matching condition (Eq. 3.9) of the resonance, it can be achieved as shown below (Eq. 3.10).

$$S = \frac{d\lambda}{dn_d} = \frac{d\lambda}{dn_{eff}} \frac{dn_{eff}}{dn_d} = \eta \frac{\lambda}{n_{eff}} \quad (3.10)$$

where $\eta = dn_{eff}/dn_d$ is governed by the fraction of the optical field that interacts with the sample.

The sensitivity is similar to that of the ring resonator demonstrated in Ref. [112, 113]. Herein, λ is the corresponding resonance wavelength, n_{eff} is the mode effective refractive index in the resonator, and η is the field fraction of the mode that interacts with the material to be measured. Clearly the sensitivity of the sensor is proportional to the field fraction in the analyte η . At the same time, the sensitivity is increasing with the working wavelength λ , which is tunable by the cavity length l within a limited variation range. As the medium with a higher RI fills the slot and its vicinity, more light is localized in the analyte for an interaction improvement and a larger value of η . As a result, the sensitivity is increasing with the RI of the analyte. For liquid environments within the RI range of $1.3 \leq n \leq 1.37$, the theoretical sensitivity is estimated to be 726 nm/RIU by a linear fit, which is higher than the sensitivity of the RI sensing in the air.

Nevertheless, the shape of the resonance evolves with the wavelength as shown in Fig. 3.19 (a). With a larger RI, the transmission dip is wider and deeper comparing the two dips for water and ethanol. The dip is deeper because of more light coupling to the slot and the wider dip is due to the smaller quality factor, which is reflectivity and absorption controlled. This should be taken into account when the characteristics (e.g. minimum detectable RI) of the sensor are considered.

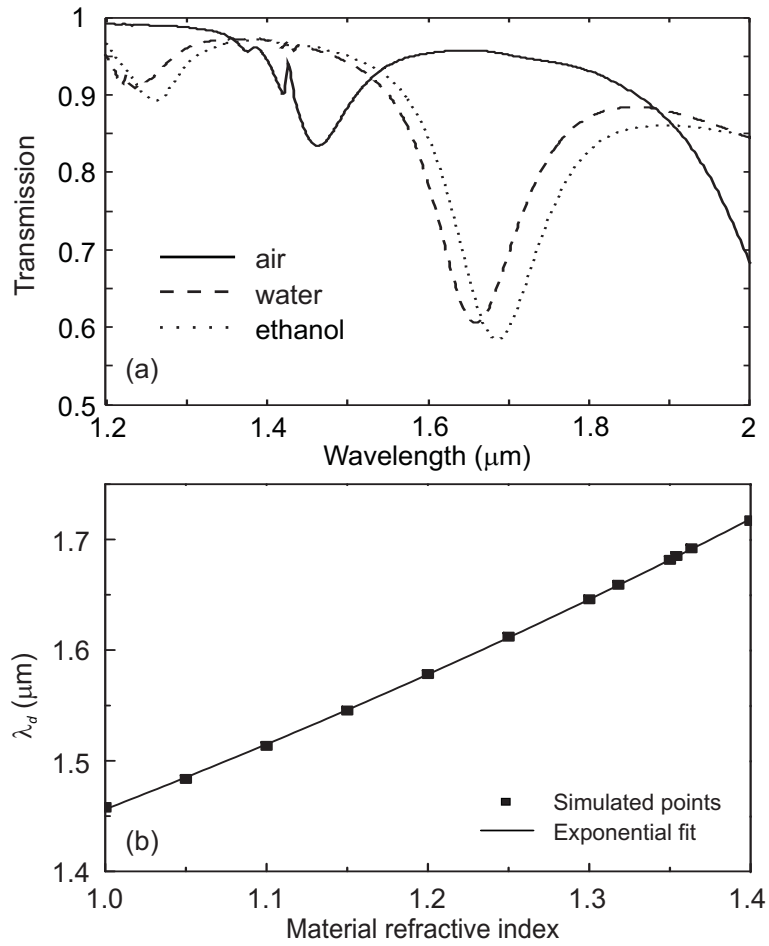


Figure 3.19: Optical property variation with different material refractive indices filling in the $30 \text{ nm} \times 20 \text{ nm} \times 700 \text{ nm}$ slots. (a) Transmission spectra for air, water and ethanol filling in and around the slots; (b) Resonance position λ_d as a function of the material index (analyte).

3. SLOT WAVEGUIDE CAVITY

Since the transmission resonance shows a small quality factor, its position is not easy to define with system noise during characterization. The first order derivative of the transmission spectrum is performed during the analysis of the experimental data. The resulting spectrum shows a dip with a smaller FWHM (full width at half maximum). The minimum point, which presents the minimum slope position on the transmission dip (left arm), is used to measure the spectral shift. For liquid detection with $1.3 \leq n \leq 1.37$, the sensitivity using the 1st order derivative performance is 622 nm/RIU, which is smaller than the sensitivity using λ_d position shifting. The reduced sensitivity indicates the influence of the dip widening with the RI increase. In other words, the left arm of the transmission dip shifts more slowly than λ_d as the transmission spectrum is widening with the RI enlargement.

3.6.2 Experiments

The geometry for the measured device is: $p = 500$ nm, $l = 700$ nm, $w = 30$ nm, $h = 20$ nm, $h_{Si} = 220$ nm, $h_{SiO_2} = 100$ nm. During the experiments, droplets of different liquids (analytes) are deposited on the Au cavity. Then the normalized transmission spectrum is measured using the same setup presented in Fig. 3.17. The refractive indices for the different liquids are $n = 1.3539$ for ethanol, $n = 1.3634$ for isopropanol (IPA), and $n = 1.318$ for deionized water. Salt-water solutions with different concentrations are also included in the experiment. The RI of the solutions is linearly varied with the salt concentration [114].

The experimental results are displayed in Fig. 3.20 where (a) shows the original and Fourier transform (FT) filtered transmission spectra for water, ethanol and IPA. The spectrum is red shifting for liquids with a higher RI. As the transmission dip is rather wide in the spectrum due to the strong field absorption, it is still not easy to track the resonance position from the Fourier transform (FT) filtered spectra. The first order derivative is performed on the filtered spectra and its minimum is used for the determination of the spectral variation. Fig. 3.20 (b) shows the linear fitting of the minimum positions of the 1st order derivative versus the material RI. The experimental sensitivity is 730 ± 10 nm/RIU in Fig. 3.20, which is compared with the calculated sensitivity of 622 nm/RIU for the 1st order derivative consideration. Note that the experimental sensitivity is in good agreement with the sensitivity 726 nm/RIU obtained from the λ_d shift. The discrepancy in sensitivity may arise due to the transmission spectrum of the fabricated structure not displaying an apparent widening effect. In the experiment, the shape of the transmission spectrum is affected by the energy loss in the structure and the excited modes. This combination of fabrication error and propagating modes may cause a non-expansion of the spectrum with the increase of the RI.

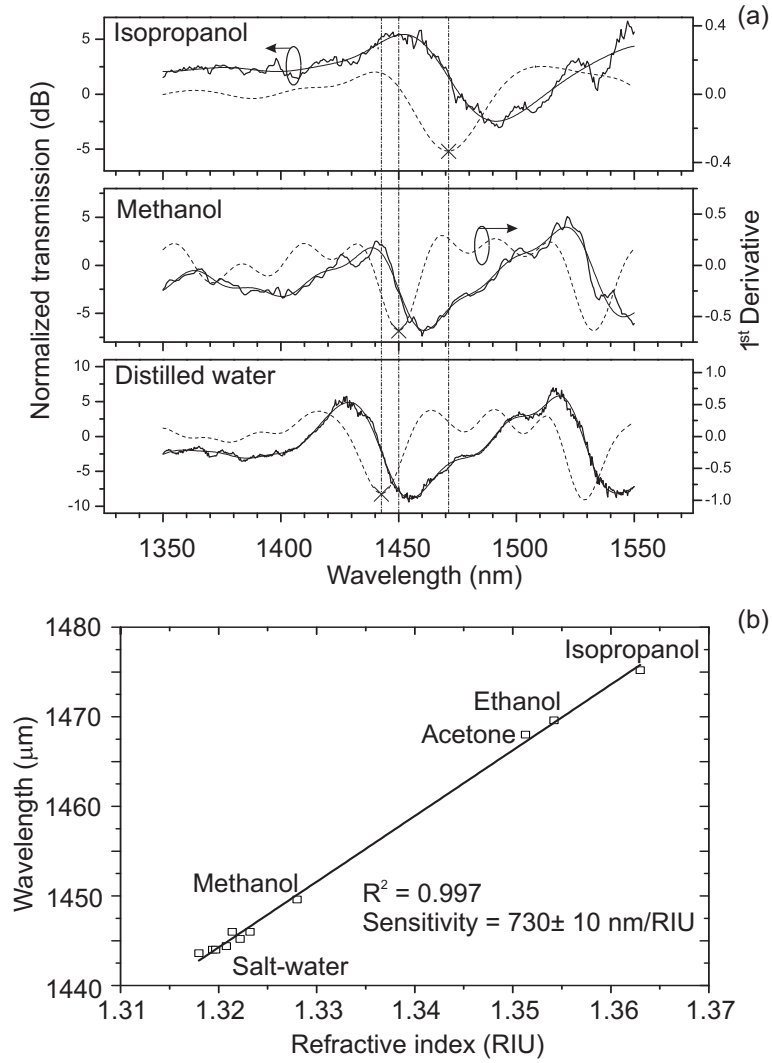


Figure 3.20: Experimental results for the SWC device ($p = 500 \text{ nm}$, $l = 700 \text{ nm}$, $w = 30 \text{ nm}$, $h = 20 \text{ nm}$, $h_{Si} = 220 \text{ nm}$, $h_{SiO_2} = 100 \text{ nm}$): (a) Transmission spectra for different liquids; (b) Sensitivity of the device (1^{st} derivative minimum vs refractive index of the analyte).

3. SLOT WAVEGUIDE CAVITY

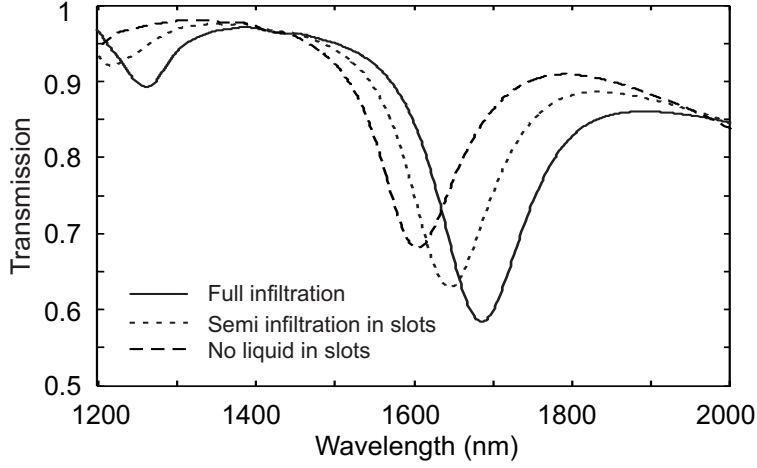


Figure 3.21: Calculated transmission spectra for different types of infiltration of ethanol in the cavity slots.

Herein the infiltration of liquid is not considered as the reason for the sensitivity discrepancy. Actually liquid infiltration in such a small slot is a complicated topic in the field of optofluidics. The viscosity between the surface and the liquid molecules induces specific challenges when the area is reduced from macro to micro or even nano dimension. Simulations have been made to check the impact of partial infiltration of liquids on the transmission spectrum. For different percentages of infiltration of ethanol on the Au cavity, the corresponding transmission spectra are given in Fig. 3.21. λ_d is clearly varied with different infiltration profiles of ethanol inside the slot. Even though the cavity slot is minute in dimension, the field localization in the slot makes the spectrum strongly dependent on the infiltration profile of the analyte. Assuming all the three liquids have the same infiltration percentage in the slot, the sensitivity of the sensor for full infiltration, semi slot infiltration and no liquids in slots can be 726 nm/RIU, 576 nm/RIU, 458 nm/RIU, respectively. Apparently, the liquid filling in the slot array determines the sensitivity of the sensor. Of course, the infiltration model for different liquids is related to the liquid property, which makes the sensitivity analysis more complicated. For a liquid droplet on a flat surface of a solid material, a contact angle depending on the hydrophilic property of the solid material is formed. During our experiments, the transmission spectrum is red shifting when the salt-water droplet size is increased. This phenomenon may be explained by the infiltration variation with the droplet size. The droplet size-dependent topic will be described in detail in the thesis of Armando Cosentino.

3.6.3 Performance evaluation

Our device is studied to be a RI based sensor, for which the resonance position λ_d is the key parameter for the RI detection. A standard characteristic is generally used to quantify the performance of the RI based sensors: the resolution R , which is defined to be the minimum detectable RI variation. The resolution R is related to the sensitivity (S) and the output resolution (r) by

$$R = r/S \quad (3.11)$$

The output resolution r is the minimum spectral shift that can be accurately measured. The section *Sensitivity and resolution* in Chapter 2 discusses the resolution determination. Conventionally, r is approximated to be the three standard deviation of the system noise (Eq. 2.5), which includes the amplitude noise (thermal and shot noise), equipment quantization accuracy (light source and OSA), and the device thermal stabilities. For the OSA with a resolution of 0.05 nm, the standard deviation of the OSA (σ_{spec}) is 0.014 nm assuming a uniform distribution of the error between -0.025 nm and 0.025 nm. For extremum position tracking of λ_d , the standard deviation σ_{amp} of the amplitude noise is linked to the quality factor (Q) and the signal-to-noise ratio (SNR) (Eq. 3.12) from statistical Monte Carlo simulation [9]. Appendix A explains the calculation process to calculate this standard deviation in detail.

$$\sigma_{amp} \approx \frac{\lambda}{4.5Q(SNR^{0.25})} \quad (3.12)$$

The theoretical transmission curve for water infiltration has the following values: $Q = 14$, $\lambda = 1659$ nm, SNR is assumed to be the SNR of the OSA ($SNR = 60$ dB). Then $\sigma_{amp} = 0.84$ nm. Apparently $\sigma_{amp} \gg \sigma_{spec}$ due to the low value of Q . Ignoring the thermal stability, the amplitude noise is the dominating factor in the resolution determination. Thus $r \simeq 3\sigma_{amp} = 2.52$ nm. With the sensitivity $S = 726$ nm/RIU, the resolution is estimated to be $R = 3.5 \times 10^{-3}$ RIU. The resolution is low compared with the sensors in the literature.

The improvement of R can be realized through the sensitivity enlargement or noise reduction. For our low quality factor device, the dominating amplitude noise depends on the quality factor and the signal-to-noise ratio (SNR) of the resonance dip (Eq. 3.12). Thereby, the sensitivity S , the quality factor Q , and SNR will be discussed for the performance improvement, respectively. Note that the quality factor is defined to be $Q = \lambda_d/\text{FWHM}$, which loses its physical meaning after mathematical transformations on the transmission spectrum.

For the SWC device, the sensitivity is described by Eq. 3.10. S is proportional to λ and η , and inversely proportional to n_{eff} . Based on the parameter study, the sensitivity is geometry dependent. Both η and n_{eff} are related to the confinement

3. SLOT WAVEGUIDE CAVITY

ability of the slot. When the slot shrinks (w or h decrease), n_{eff} is increased (Fig. 3.8) while η is increasing simultaneously due to the higher field confinement in the slot. Conversely, η and n_{eff} decrease with the increase of the slot dimension. Thereby the sensitivity S cannot be enhanced significantly by a modification in the slot dimensions. At the same time, the fabrication techniques restrict the slot dimensions to a minimum value. Considering the dimensions of the Si waveguide (Fig. 3.13), the increase of the SiO₂ layer thickness h_{SiO_2} decreases the n_{eff} and enhances the field confinement in the slot, meaning η is enlarged. For example, with structure parameters: $p = 400$ nm, $w = 30$ nm, $h = 20$ nm, $l = 700$ nm, $h_{Si} = 220$ nm, $h_{SiO_2} = 50$ nm, the sensitivity is 549 nm/RIU in liquid environment, which is smaller in comparison with the fabricated structure. The lower sensitivity results from the η decrease and n_{eff} increase at $h_{SiO_2} = 50$ nm. Consequentially, the sensitivity is increasing with h_{SiO_2} until the condition when the waveguide substrate can be approximated to be pure SiO₂. For the fabricated structure with $h_{SiO_2} = 100$ nm, the sensitivity is close to the optimized value.

Regarding the quality factor of the resonance, the FP model discussion reveals the very low quality factor due to the high absorption of the mode in the slot. The finesse definition (Eq. 3.4) shows that the quality factor depends on both the absorption coefficient α_s of the excited mode in the slot and the reflectivity $(n_{eff} - n_0)/(n_{eff} + n_0)$ at the edge of the slot cavity. However, when the field localization is enhanced in the slot, n_{eff} is increased while the absorption α_s by electrons is also increased (Fig. 3.6). The quality factor improvement through geometry modification is also not apparent. Experimentally, the value enhancement of the quality factor can be fulfilled by a series of mathematical transformations. First, the logarithm transform of the transmission spectrum improves Q from 14 to 15.3. Then the 1st order derivative shows that Q is improved from 15.3 to 25 in theory. Herein the Q improvement means the error reduction in tracking the minima position. Excluding mathematical post-processing, another possible way to increase the quality factor is to add Bragg mirrors physically on both sides of the Au cavity. The reflectivity is enlarged while the absorption of the slot is not affected. Then the quality factor is improved.

The resolution can be improved by 16% or 24% when the SNR is two to three times the original SNR , respectively. In general, SNR increases with the amplitude of the resonance A_d . Note that the above resolution calculations assume $SNR = 60$ dB. The FT filtering process and the measurement averaging are performed on the experimental transmission spectrum, which improve the SNR significantly. One has to also note that, when the transmission dip is too small, it is still difficult to achieve the spectrum by averaging and FT filtering. From the above discussion for sensitivity, the sensitivity can be improved by the increase of h_{SiO_2} . Nevertheless, the dip amplitude A_d is decreasing with h_{SiO_2} . With the structure parameters: $p = 400$ nm, $l = 700$

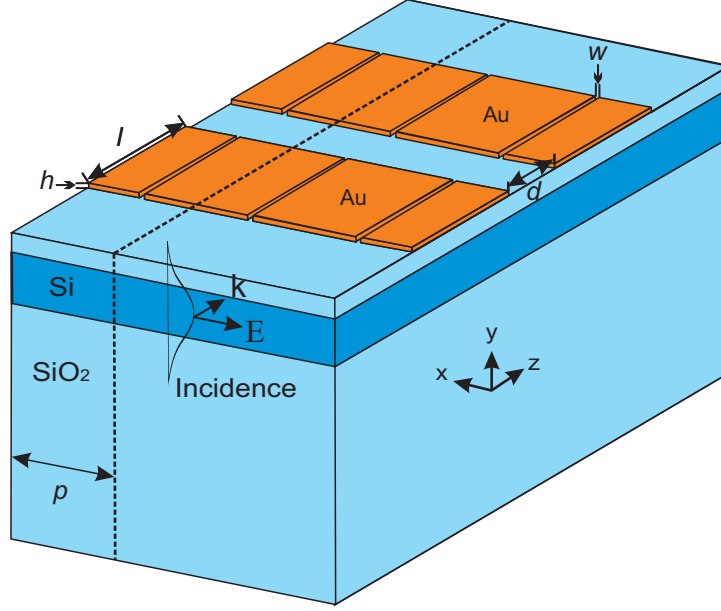


Figure 3.22: Scheme of a cascaded structure with two slot arrays, where d is the separation between the arrays.

nm, $w = 30$ nm, $h = 20$ nm, $h_{Si} = 220$ nm, $h_{SiO_2} = 100$ nm, $A_d = 0.1$ in an air environment. A cascaded structure is considered to enlarge A_d without affecting the sensitivity and the quality factor.

The scheme of the cascaded structure is shown in Fig. 3.22, where multiple slot arrays (N) are deposited on the Si waveguide. The other parameters are maintained as in the description. The distance between slot arrays is set to be $d = 150$ nm. With such a distance, the well field confinement in each slot (Fig. 3.3) makes coupling between adjacent cavities negligible. Since the resonance condition is identical for each cavity, λ_d is almost the same as for the single cavity. The transmission spectra comparison in Fig. 3.23 verifies that λ_d is independent of the cavity number N . Excluding λ_d , A_d is enlarged due to increased light coupling to sequential cavities. Under air condition, A_d equals 0.10, 0.21, 0.30 for $N = 1, 2, 3$, respectively. The quality factor does not vary since the absorption for each resonance depends separately on the cavity itself. Of course, the dip is broadened with A_d . In this case, the cascaded structure is expected to improve the performance of the device with shallow transmission dips. Finally, the SNR of the detected signal can be improved to the level of the detector by FT filtering and signal averaging.

The above resolution analysis is performed purely on the theoretical spectrum to evaluate the possibility of an improvement in resolution. For the fabricated structure, the resolution should be estimated based on the parameters from the experimental

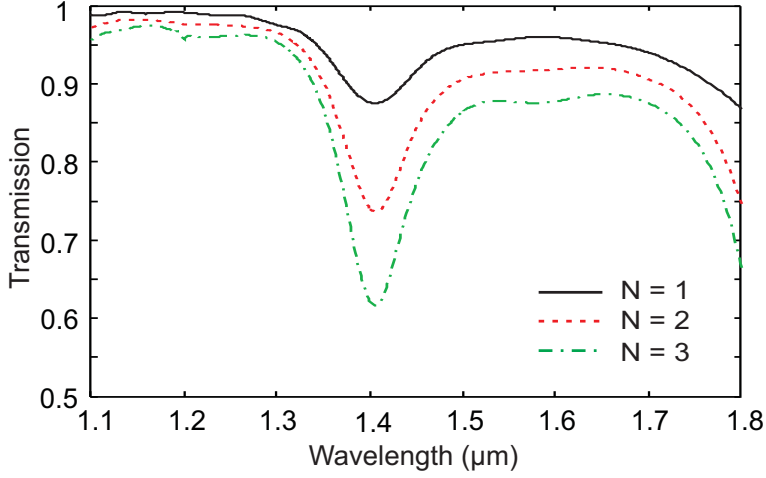


Figure 3.23: Transmission spectrum comparison for cascaded structure with different number of arrays (N).

spectrum. Considering the experimental spectrum of distilled water (Fig. 3.20 (a)), $Q = 34$, $\lambda = 1453.8$ nm for the filtered spectrum. Apparently, the resonance is narrowed after the 1st order derivative is implemented. The resultant quality factor is $Q = 72.15$, which is more than two times the quality factor Q for the transmission spectrum. With other parameters $\lambda = 1443$ nm, $SNR = 60$ dB, $S = 730$ nm/RIU, the resolution is calculated to be 5.8×10^{-4} RIU. The improved resolution over the simulation is due to the Q improvement in the amplitude noise determination (Eq. 3.12). The Q improvement is considered to be mainly due to a series of mathematical post-processing steps, including logarithm transform in dB, FT filtering, and 1st order derivative.

In conclusion, post-process of the transmission spectrum is shown to be important for the performance improvement of the sensor, especially the one with a low quality factor. The optimum performance is obtained when the amplitude noise is not the determining factor for the output resolution r . In theory, it is possible to cancel out the amplitude noise using sufficiently different measurements for identical detection. Under this condition, the standard deviation of the OSA dictates r with $r = 3\sigma_{spec} = 0.042$ nm. The ultimate resolution is 5.8×10^{-5} RIU, which is comparable with other optical devices in the RI detection.

3.6.4 Discussions

Basically, the SWC device has been demonstrated to be capable of refractive index (RI) sensing theoretically and experimentally. The characteristics of the sensor are listed in Table 3.2 for both the theoretical and experimental values.

The resolution difference between the theory and the experiment is due to the higher Q in Eq. 3.12 and the post-process of the transmission spectrum. The experimental

Table 3.2: Characteristics of the SWC sensor

Characteristics	Theory	Experiment
sensitivity	726 nm/RIU	730 ± 10 nm/RIU
resolution	3.5×10^{-3} RIU	5.8×10^{-4} RIU
span	1.0~ 1.4	1.0~ 1.4
hysteresis	0	0
repeatability	good	good

resolution is not as high in comparison to other sensors in the literature. Surface plasmon resonance (SPR) sensors [17] can achieve a resolution in the order of 10^{-6} to 10^{-7} RIU for commercial instruments. Ring resonators have been demonstrated to achieve a resolution at the level of 10^{-7} RIU. Photonic crystal (PhC) sensors have a smaller interaction area, resulting in a relatively lower sensitivity. Their high quality factor still helps to provide a resolution of 10^{-5} RIU. The optimum resolution of the SWC device can be expected to reach 5.8×10^{-5} RIU, when the amplitude noise is negligible. Furthermore, its advantage lies in the smaller sample volume requirement than the other sensors, its relative ease to be integrated for lab-on-a-chip devices and in parallel measurement systems.

3.7 Conclusion

Due to the coupling of the electromagnetic field with free electrons on the metal surface, light interaction with nano-structured metallic thin films exhibit interesting optical properties such as high light confinement by extreme sub-wavelength structures, which can be applied for local sensing. Simultaneously, the field confinement is accompanied by a strong light absorption, allowing light to propagate in the order of tens of micrometers. In this chapter, the metallic slot array has been integrated as a cavity on a Si waveguide. The Fabry-Pérot resonance in the slot array results in a resonant coupling between the Si waveguide and the metallic cavity. Due to this resonant coupling, the transmission spectrum of the Si waveguide displays resonant dips. The theoretical study has shown the dependence of the transmission properties on the geometrical dimensions. The field localization in the slot leads to an apparent variation of resonant coupling by modification of the Au cavity and the Si waveguide dimensions. Moreover, its sensitive reaction to the material refractive index in the slot confirms its useful application in RI sensing. The sensor is applicable for a large panel of analytes and a theoretical sensitivity of 726 nm/RIU can be achieved in liquid environment.

The slot waveguide cavity device is fabricated by e-beam lithography and lift-off methods. The fabrication techniques enables a realization of the slot structures down to 30 nm in width.

3. SLOT WAVEGUIDE CAVITY

Characterizations have verified the working function and its suitability in liquid sensing by measurements with different liquids. The sensor performance has also been evaluated. Even though the resolution of the present device is not currently as good as other refractive index based sensors, cascaded structure and postprocessing methods have been discussed to optimize the performance further. An optimum resolution down to 5.8×10^{-5} RIU is anticipated by the spectrum shift detection. From the sensing point of view, the SWC device shows its advantage for a sensitive detection in the nano scale. Moreover, the planar configuration implies the compatibility with other photonic devices.

Chapter 4

Annular Aperture Array

4.1 Introduction

In the course of last decade, it has been demonstrated [78, 79] that a thin nano-patterned metallic film may exhibit an unexpected enhanced transmission compared to Bethe's theory [115]. Different theoretical [116, 117] and experimental [74, 118, 119] studies have been carried out to understand the physics of this phenomenon and a development of devices based on such structures for various applications [120, 121].

This extraordinary transmission alters as a function of the hole-shape [122], the metal film thickness, the lattice arrangement, and, of course, on the material. The colloquium prepared by F. J. García de Abajo in 2007 explains in detail the difference between different kinds of nanoapertures, which are able to provide this extraordinary transmission [123]. We will here focus on two particular cases: circular [78] and annular apertures [79, 119]. First, the enhanced transmission has been explained by the coupling of surface plasmons on the two surfaces of the device (circular holes case) [78, 124]. But for the annular aperture [117], the work of Cao and Lalanne [107] has verified that the presence of a guided mode inside these subwavelength apertures can also be the principal factor leading to the extraordinary transmission. Moreover, the surface plasmon may play a negative role on the transmission.

With regard to applications, optical sensing is one of the most important topics. Indeed, the excited surface plasmon wave on circular aperture arrays penetrates strongly into the medium, which is in close proximity to the metal surface. Modifications (refractive index variations) of the output medium result in a shift of the resonance in the transmission spectrum [81]. In addition, the planar geometry [80] makes these types of structures good candidates for integration as on-a-chip sensors having the possibility of detecting environmental variations in a compact device. Ultimately, it allows a good compatibility with other integrated optical elements, optoelectronic components and

fluidic systems as it has been shown in the references [84, 125, 126], where nanohole arrays have been used as biosensors. The nanohole can act as flow-channel to enable rapid analyte delivery and improve the response time by up to 20-fold for small molecules [86]. In addition to nanohole arrays, disk or ring resonators have shown promising results in terms of sensitivity (around 600 nm/RIU) [76, 127]. Some other metallic structures present field confinement in a far-subwavelength region, which is interesting for local sensing with a small sample volume [99, 100].

We propose here to investigate the behavior of the electromagnetic field inside coaxial apertures when illuminated in-plane. The approach appears to benefit from the strong field localization in the annular aperture while the planar configuration attracts the interest in integration with dielectric devices. The field localization provides a high sensitivity associated to a local interaction with the measured medium. In this chapter, the integration of these nanostructures is considered in the context of direct waveguide-nanostructure embedding.

4.2 Design & Principle

Figure 4.1 presents the schematic view with three periods of the investigated structure. The structure consists of one row of annular apertures in a block of gold, which is embedded in a silicon nitride (Si_3N_4) waveguide (refractive index $n_1 = 1.98$). The geometrical parameters are: the periodicity (p), the cut distance (d_0), the inner radius (r_i), the outer radius (r_e) of the aperture, and the block metal thickness (d_1). The incident medium has a refractive index n_1 , while an analyte with refractive index n_2 fills the annular aperture of the cavity part. The working wavelength is the telecom wavelength ($\lambda = 1.55 \mu\text{m}$). Water ($n_2 = 1.32$) is first considered to fill the aperture in the gold (Au) cavity. For the illumination, TM polarized light is normally injected to the cavity with the electric field component oriented perpendicularly to the axes of the aperture.

The finite integration time domain (FITD) method [93], which is similar to the finite difference time domain (FDTD) [92] method, is used to simulate the optical property of the device. We consider here a two-dimensional model: the structure is infinite in the y direction. In the model, the periodic boundary condition is applied in the x direction and perfectly matched layers (PML) are added at the z_{max} and z_{min} edges of the model to absorb propagating light and then to avoid parasitic reflections. A non-uniform mesh is used for the space discretization: a step size of 1 nm in the Au cavity region, where the small details are located, and a step size of 20 nm for the Si_3N_4 waveguide. The dispersion of gold is modeled by the Drude model (Eq. 3.1) described in Chapter 3, in which the plasmon frequency $\omega_p = 1.2042 \times 10^{16} \text{ s}^{-1}$, and the damping

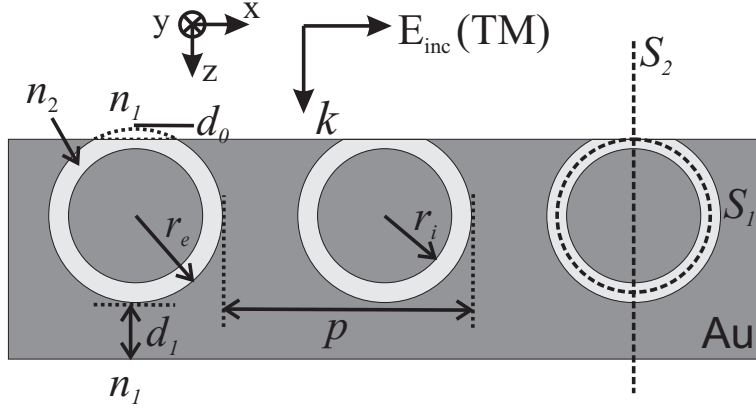


Figure 4.1: Schematic view of the studied cavity. The geometrical parameters of the structure are: the cut distance (d_0), the inner radius (r_i), the outer radius (r_e), and the periodicity (p). TM polarized light is normally incident on the periodic cavity.

rate $\gamma = 1.3754 \times 10^{14} \text{ s}^{-1}$. The geometrical parameters of the cavity are: $p = 600 \text{ nm}$, $r_e = 180 \text{ nm}$, $r_i = 140 \text{ nm}$, $d_0 = 10 \text{ nm}$.

Figure 4.2(a) shows the reflection spectrum for the parameters detailed earlier. A dip appears in the reflection spectrum at the wavelength $\lambda_r = 1.53 \mu\text{m}$. The block thickness of gold d_1 is set to be 80 nm , which is thick enough to allow less than 1% of light transmission. We make the assumption that the absorption of the cavity can be calculated by $A = 1 - R - T$ where R is the reflection and T is the transmission. Thus light is strongly absorbed as $A = 0.998$ at the resonance λ_r . This can be explained by the cavity-resonance, which induces localization of the electromagnetic field, accompanied by an absorption of the field itself. The electric field amplitude $|E|$ distribution is displayed at $\lambda = \lambda_r$ in Fig. 4.2(b), which shows the field localization in the aperture of the cavity. Since the device is intended to be a sensor, the maximum light localization in the aperture implies that a high interaction volume with the analyte is possible and it corresponds to an optimized sensing performance.

In consideration of the working mechanism of the resonance, the phase distribution along different directions is given in Fig. 4.3. Graph (a) is the phase of E_x along the center of the circular aperture (dashed line S_1 in Fig. 4.1), while graph (b) follows the phase in the propagation direction (z-axis) (dashed line S_2 in Fig. 4.1). Note that graph (a) shows a standing wave phase profile and has a phase step of π . The light is separated in two parts at the entrance of the cavity. One wave is propagating clockwise and another is propagating counter clockwise, which create a standing wave in the annular aperture. Graph (b) presents the phase profile of a standing wave in the cavity region, compared with the propagating wave in advance of and following the cavity region. The propagating wave shows that a part of the light can pass through the block of gold and one observes a phase shift of π between the input and the output of

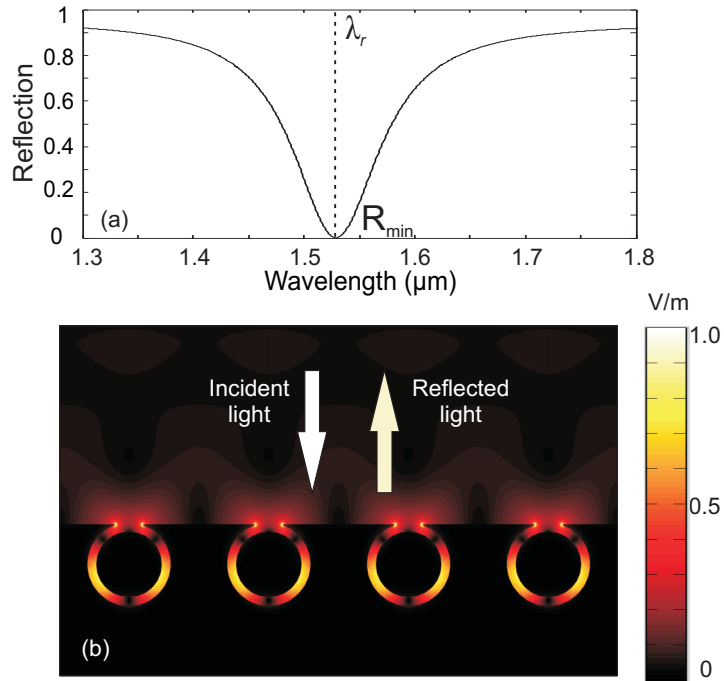


Figure 4.2: Calculated (a) reflection spectrum and (b) electric field amplitude ($|E|$) distribution at resonance $\lambda_r = 1.53 \mu\text{m}$. The device parameters are: $p = 600 \text{ nm}$, $d_0 = 10 \text{ nm}$, $r_i = 140 \text{ nm}$, $r_e = 180 \text{ nm}$, $d_1 = 80 \text{ nm}$. The incident material is Si_3N_4 ($n_1 = 1.98$) and water ($n_2 = 1.32$) fills the aperture.

the cavity, which corresponds to the first mode of a Fabry-Pérot (FP) interferometer. This FP resonance allows a high confinement of the electromagnetic field in the annular aperture, as shown in Fig. 4.2 (b).

To completely study the resonance mechanism, a quantitative analysis is undertaken in the following discussion. First of all, a simplified but analogous structure is considered as shown in Fig. 4.4. The cavity length is assumed to be $l = 2r_e - d_0$ and the aperture width is $w = r_e - r_i$. The separation s is large enough that the coupling between the two slits is not relevant. Comparing the cell of the AAA device with this simplified structure, w and s are functions of the z position, for the AAA cell. Even though the two are not identical, the simplified structure is expected to show the influential parameters of the AAA device. Then the mode supported by the subwavelength metal-insulator-metal (MIM) configuration is calculated. Finally, the phase condition of the FP interference is discussed to verify how it matches the resonance condition of the AAA structure.

The waveguide mode in a MIM structure, which is Au-water-Au in our case, is calculated. According to Gordon and Brolo [128], the supported TM mode (\vec{E} field perpendicular to the metal-dielectric interface) is the sum of two exponentially decaying SP modes on both interfaces of the dielectric layer. The cut-off wavelength of this mode increases as the width of the insulator (w) becomes smaller. Since w is very thin compared with $\lambda/2n_d$, the fundamental TM mode is guaranteed with the propagation constant β_{TM} given in Eq. 4.1 [128]. The propagation constant can be written as $\beta_{TM} = \beta_r + j\beta_i$ where the real part is related to the mode effective refractive index ($n_{eff} = \beta_r/k_0$) and the imaginary part to the propagation length of the mode ($L = 1/(2\beta_i)$).

$$\tanh\left(\frac{\sqrt{\beta_{TM}^2 - k_0^2 \varepsilon_d}}{2} w\right) = -\frac{\varepsilon_d}{\varepsilon_{Au}} \frac{\sqrt{\beta_{TM}^2 - k_0^2 \varepsilon_{Au}}}{\sqrt{\beta_{TM}^2 - k_0^2 \varepsilon_d}} \quad (4.1)$$

where ε_d is the permittivity of the insulator and k_0 is the light propagation constant in vacuum.

By considering Eq. 4.1, one can observe that the width w of the cavity has a dominating role. The dispersion property of the TM mode is shown in Fig. 4.5 for Au-water-Au case. The insulator width is set to be 40 nm as in Fig. 4.2. Clearly the TM mode shows a relatively weak dispersion. The effective refractive index n_{eff} of the mode is almost constant, which slowly declines from 1.999 to 1.9894 as the wavelength increases from 1.4 μm to 2.0 μm . The short propagation length L around 3.64 μm verifies the strong absorption of the mode. According to the previous discussion, the absorption A is 0.998 at the resonance $\lambda_r = 1.53 \mu\text{m}$. Therefore, the almost perfect absorption is due to the lossy nature of the supported mode.

4. ANNULAR APERTURE ARRAY

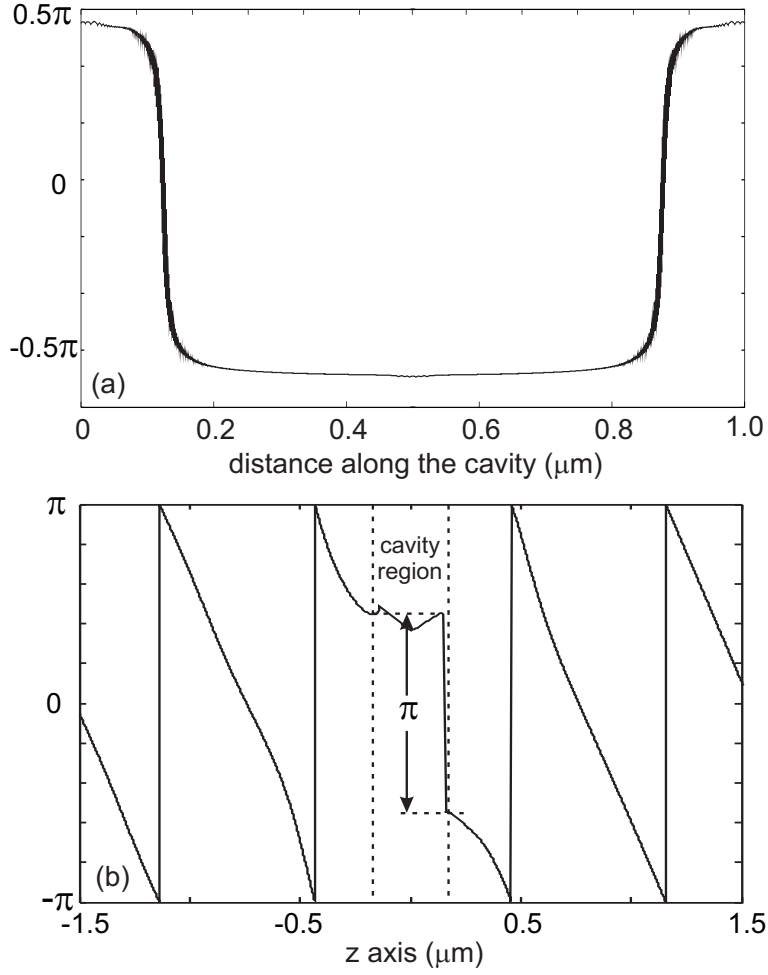


Figure 4.3: Phase distribution of the electric field component E_x for the reflection dip in Fig. 4.2: (a) along the middle of the circular aperture (dashed line S_1 in Fig. 4.1); (b) through the middle of the cavity and along the propagation direction ($+z$) (dashed line S_2 in Fig. 4.1). The vertically dashed lines show the edge positions of the cavity.

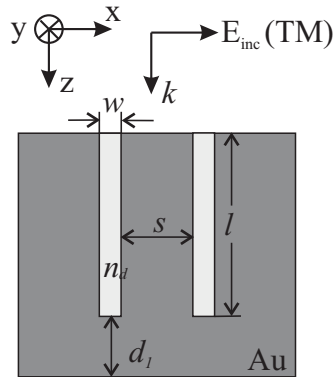


Figure 4.4: Simplified structure for quantitative analysis.

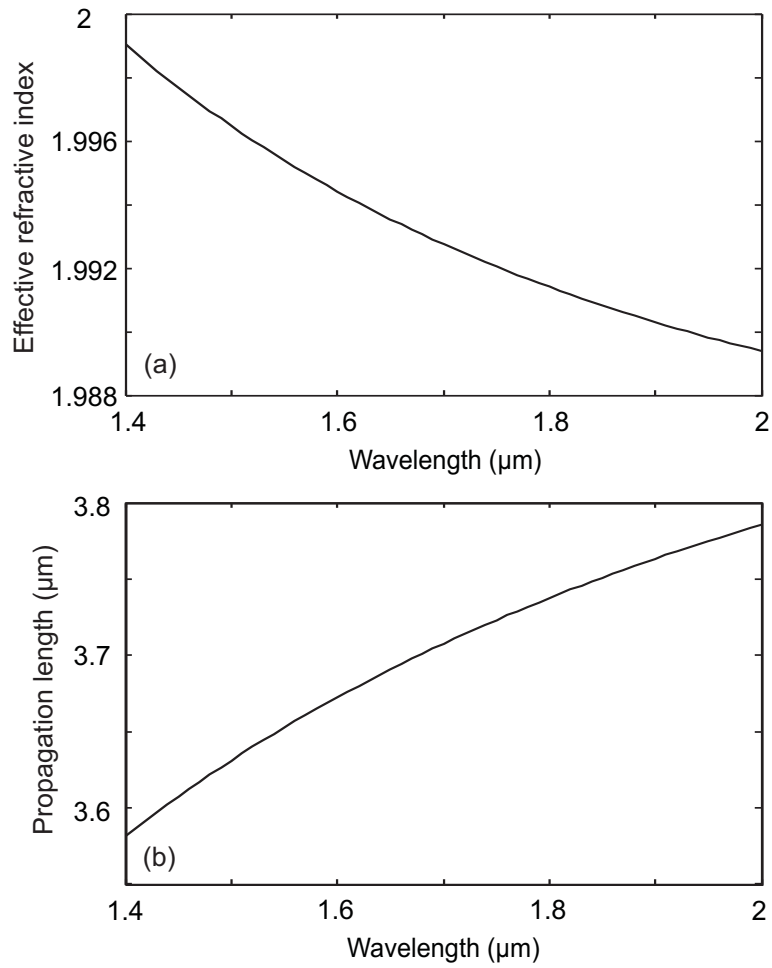


Figure 4.5: Dispersion property of the cavity mode in Au-water-Au structure: (a) mode effective refractive index (n_{eff}) and (b) propagation length (L) with varied wavelength.

4. ANNULAR APERTURE ARRAY

Then the phase matching condition for the E_x component at the resonant FP interference is calculated by

$$\phi = 2 \int k_0 n_{eff}(z) dz + \phi_1 + \phi_2 = 2m\pi \quad (4.2)$$

with m an integer. n_{eff} is the effective index of the supported mode at the z -axis cut-plane through the cavity. ϕ_1 and ϕ_2 represent the phase shifts due to reflection at the two interfaces.

From the FP analysis of the AAA structure, the phase in Eq. 4.3 is expected to be $\phi_{exp} = 2\pi$ at the resonance λ_r . For the field component E_x in the simplified structure (Fig. 4.4), $\phi = 2 \int \mathbf{k} \cdot d\mathbf{l} = 2 \int k_z dz = 2 \int k_0 n_{eff} dz$, for which ϕ_1 and ϕ_2 are disregarded. The TM mode is homogenous for the whole cavity at $\lambda_r = 1.53 \mu\text{m}$, thus $n_{eff} = 1.9958$. We obtain $\phi = 2k_0 n_{eff}(2r_e - d_0) = 1.826\pi$. The recovered phase deviates from the phase ϕ_{exp} in the AAA structure due to the n_{eff} mismatch and the phase shifts (ϕ_1 and ϕ_2) due to reflection. The n_{eff} mismatch indicates that in the AAA structure, the slit width w variation causes n_{eff} as a function of z and the variation of the slit separation s influences the interaction between neighboring slits. With $s = 140 \text{ nm}$, the resonance of the simplified structure appears at $1.237 \mu\text{m}$, which is blue shifted from the AAA structure. Taking everything into account, the phase matching condition (Eq. 4.2) quite well matches the Fabry-Pérot (FP) like property of the resonance in the AAA structure.

Above all, the FP-like waveguide mode resonance inside the Au cavity results in a field confinement and a resonant dip in the reflection spectrum. In the phase matching condition for the resonance, the refractive index n_{eff} of the supported mode and the cavity length in Eq. 4.2 are vital parameters, which are then determined using the device geometry dimensions.

In addition to the resonance position λ_r , the quality factor (Q) and the reflection at the resonance (R_{min}) are essential properties. As discussed in the quantitative analysis of the SWC device (Chapter 3, 3.2.2 Quantitative FP analysis), the cavity loss leads to a deterioration in Q. In our MIM configuration, the cavity mode is also strongly absorptive. Consequently, the resonance has a low quality factor of 16.5. Nevertheless, the amplitude of the resonance is very large since the minimal reflection at λ_r is equal to $R_{min} = 0.002$.

As the device is intended to be a sensor for gas or liquid, efforts to optimize the light confinement in the aperture are made to increase the interaction between light and the analyte and thus increase the sensitivity of the structure to the surrounding medium. In the next section, the variation of the design parameters will be discussed to examine their influence on the response of the nanostructure.

4.3 Parameters Study

In this section, the geometrical dimensions are varied separately leading to a property analysis. The geometry of the cavity influences the n_{eff} or the cavity length in Eq. 4.2. Therefore the reflection resonance is related to the geometry variation. The geometrical parameters considered here are: the periodicity p , which is linked to the coupling between the apertures; the cut distance d_0 , which is the opening of the cavity; the radii sum $r_e + r_i$, which is in direct relation to the length of the cavity; and finally the radii difference $r_e - r_i$, which corresponds to the width of the cavity.

Two properties of the spectrum are analyzed: the reflection dip position λ_r and the reflection at the resonance R_{min} , defined in Fig. 4.2. The study of the geometry is based on the structure dimension with $p = 600$ nm, $r_e = 180$ nm, $r_i = 140$ nm, $d_0 = 10$ nm, $n_1 = 1.98$, $n_2 = 1.32$. During the analysis, each dimension is varied while the others are kept constant.

4.3.1 Periodicity

The periodicity is responsible for the change in the coupling among neighboring apertures and the amount of light confined in the cavity. Figure 4.6(a) is the reflection map in relation to the periodicity. The periodicity p ranges from 400 nm to 1800 nm with an increment of 20 nm. λ_r , R_{min} and the shape of the dip are evidently dependent on the period. The reflection spectrum seems to be periodic with variation in p . More details will be described in the following paragraphs.

The reflection spectra for $p = 520$ nm and 820 nm are displayed in Fig. 4.6(b). For $p = 520$ nm, in addition to the desired waveguide mode resonance at $\lambda_r = 1.496$ μm , one can also observe another resonance at $\lambda_{sp}^M = 1.0306$ μm measured on the calculated spectrum. This additional dip is ascribed to the surface plasmon resonance (SPR) at the $\text{Si}_3\text{N}_4/\text{Au}$ interface. The incident light is diffracted by the periodic cavity and the surface plasmon is excited when the condition in Eq. 4.3 is fulfilled.

$$\lambda_{sp}^C = \frac{p}{m} \text{Re} \left(\sqrt{\frac{\epsilon_{\text{Si}_3\text{N}_4} \epsilon_{\text{Au}}}{\epsilon_{\text{Si}_3\text{N}_4} + \epsilon_{\text{Au}}}} \right) \quad (4.3)$$

with m a nonzero integer, corresponding to the diffraction order of the grating.

Equation 4.3 enables the calculation of surface plasmon resonance on a flat metal/dielectric interface. For $m = 1$ and $p = 520$ nm, one obtains $\lambda_{sp}^C = 1.0765$ μm . The measured wavelength ($\lambda_{sp}^M = 1.0306$ μm) in the spectrum (Fig. 4.6(b)) is slightly blue-shifted from the calculated one λ_{sp}^C . The blue shift is due to the existence of apertures on the interface, which are different from the uniform interface condition for Eq. 4.3. The electric field intensity ($|E|^2$) distribution at $\lambda_{sp} = 1.0306$ μm (Fig. 4.7) confirms that most of the field is distributed in the Si_3N_4 waveguide, which is the effect of the surface plasmon (SP) mode. Nevertheless, certain amount of light is injected to the Au cavity.

4. ANNULAR APERTURE ARRAY

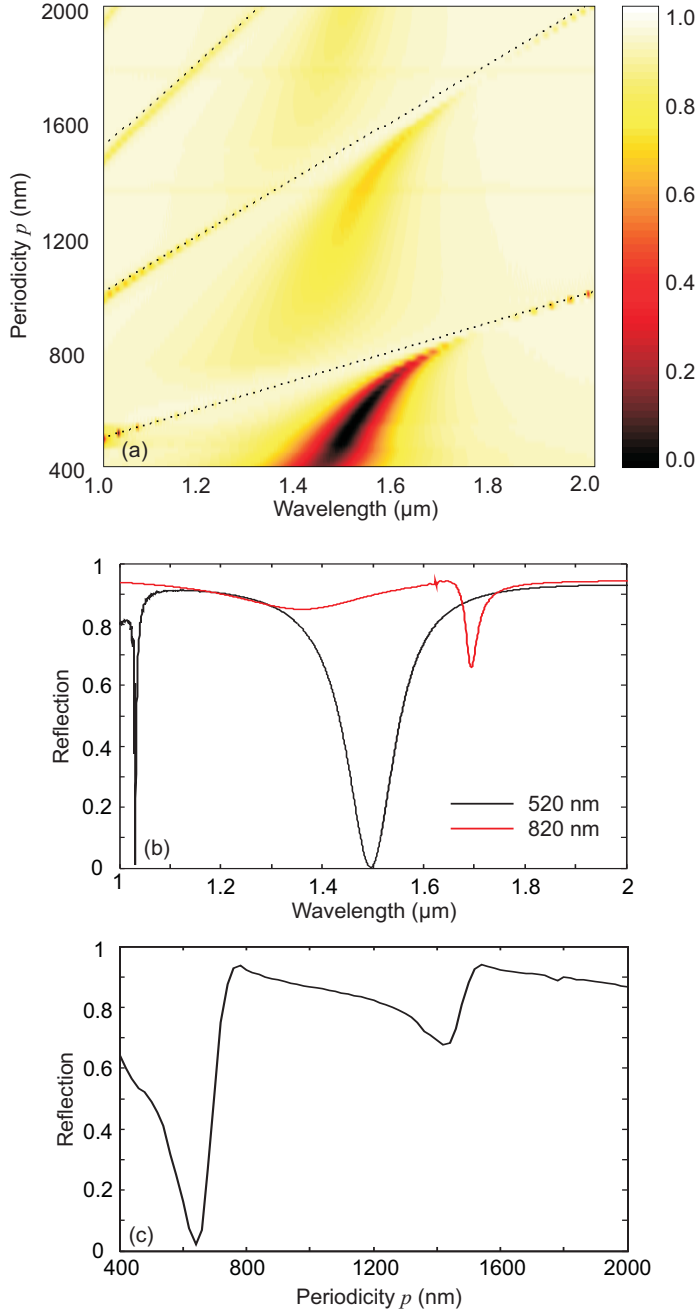


Figure 4.6: Calculated reflection spectra for (a) varied periodicity p from 400 nm to 1800 nm; (b) $p = 520$ nm and 820 nm. The other device parameters are the same as in Fig. 4.2. (c) reflection as a function of p at constant wavelength 1.55 μm . The dotted lines in (a) present Wood anomalies condition at the $\text{Si}_3\text{N}_4/\text{Au}$ interface.

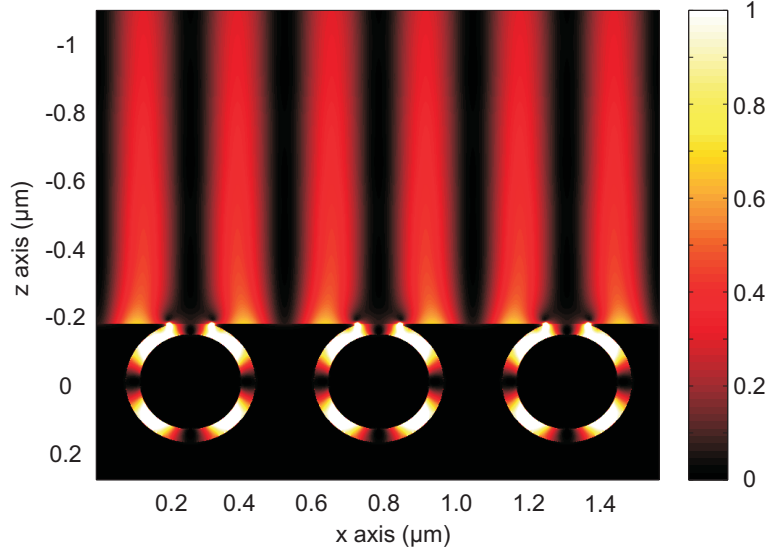


Figure 4.7: Normalized electric field intensity distribution $|E|^2$ at $\lambda_{sp} = 1.0306 \mu\text{m}$ (period $p = 520 \text{ nm}$).

The physical process can be understood, according to the study of light interaction with subwavelength apertures [75]. Light is scattered in all directions by the edge of the aperture, with the SP wave being excited at the $\text{Si}_3\text{N}_4/\text{Au}$ interface. When the counter-propagating SP waves, excited by adjacent apertures, interfere constructively with each other, a standing wave is formed at the $\text{Si}_3\text{N}_4/\text{Au}$ interface. The standing wave is periodic in the x direction as shown in Fig. 4.7. The SP excitation due to the light scattering is then enhanced. This process explains the SP excitation requirement (Eq. 4.3) where the period p is an integer times the effective SP wavelength $\lambda_{eff} = \lambda_{sp}^C/n_{sp}$, where n_{sp} is the effective refractive index of the SP wave. Moreover, the actual distance between the two adjacent edges is somewhat less than p because of the existence of apertures. Thus the measured SP excitation λ_{sp}^M is blue shifted from the calculation λ_{sp}^C , which does not consider the opening. The propagation length L of this SP mode is $10.05 \mu\text{m}$, which matches Fig. 4.7 where the SP wave penetrates deep into the Si_3N_4 waveguide.

For other periodicities, the SP resonance is shifting and its position is close to the Wood anomalies ($\lambda_W = p/m \times n_{\text{Si}_3\text{N}_4}$ with m as an integer) due to the large permittivity of Au. One can also notice that the SP resonance disappears when the SP approaches the mode resonance λ_r . For $p = 820 \text{ nm}$, there is no SP resonance and the mode resonance has a large R_{min} . It means light is less efficiently coupled to the cavity. This can be interpreted due to coupling between the SP resonance and the waveguide mode resonance.

4. ANNULAR APERTURE ARRAY

A group of studies [107, 129, 130] have been performed on the light transmission through a periodic array of slits in a thick metallic film. SP on the metal film surface plays a negative role in light transmission. The coupling of SP polaritons and the light in the metallic nanoslits prohibits light from injection into the slits. Similarly, the excitation of the SP resonance in our device blocks the light injection into the aperture of the cavity. Its interference with the broadband waveguide mode resonance results in the shallowing of the resonance (e.g. $p = 820$ nm). Note that the interference strength between the SP resonance and the waveguide mode resonance is enhanced with decreasing separation of the two resonances. When λ_{sp} and λ_r are well separated (e.g. $p = 520$ nm), the interference strength is small.

When p increases, λ_r shifts to the red within a certain range. There are two factors that contribute to this shift. According to the discussion, the interference coupling between the SP resonance and the waveguide mode resonance is the prime reason. Additionally, another reason can be the slight variation of n_{eff} with p , especially for small p , as p concerns the separating distance and interaction between adjacent circular apertures. When $p = 400$ nm, the distance is minimum and the interaction between adjacent apertures is maximum. This interaction is reducing with enlarged p and can be disregarded when p is larger than 800 nm.

Based on the discussion for the coupling among the two resonances, another important property is that the reflection is quasi-periodic with p variation. Figure 4.6(c) is extracted from the map (a) for the reflection with varied p at $\lambda = 1.55$ μm , which shows a quasi-periodic profile with p . At $p = 780$ nm and $p = 1540$ nm, the reflection is maximum, meaning minimum light injection into the cavity. From the SP excitation by Eq. 4.3, we can obtain $p = 767$ nm and 1534 nm for $m = 1, 2$, respectively. The agreement supports the discussion that SP plays a negative role on light injection to the cavity. For the relative minimum reflection at $p = 640$ nm and 1420 nm, they locate just before the SP resonance. The increased reflection from 0.022 at $p = 640$ nm to 0.678 at 1420 nm is due to the reduced fill factor of the opening so that more light is reflected back by the Au surface.

In a word, the device property is periodicity dependent mainly through the coupling between the SP resonance and the waveguide mode resonance. Physically, the incident light is scattered by the aperture edges and surface waves on the $\text{Si}_3\text{N}_4/\text{Au}$ interface are excited. When the forward and backward scattered waves between adjacent apertures edges constructively interfere with each other, the SP wave is enhanced and a small amount of light is injected to the aperture. Conversely, the destructive interference among scattered surface waves will improve light injection to the aperture. Once the waveguide mode resonance in the cavity is satisfied, light is continuously injected by the surface wave. As a result, the amount of light confined in the cavity is in excess of the fill factor of the opening. Of course, the injected light is fill factor dependent.

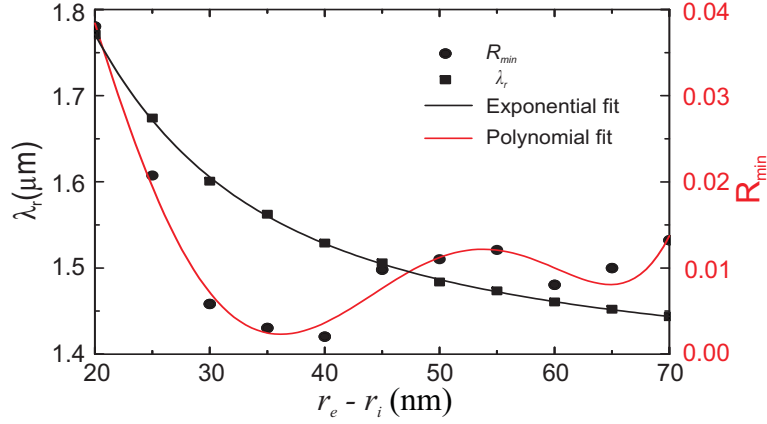


Figure 4.8: Calculated resonance position λ_r (squares) and R_{min} at λ_r (circles) for varied $r_e - r_i$. Other device parameters are the same as in Fig. 4.2.

When the fill factor decreases, the light injection enhancement by scattered waves is reduced. This occurs for any light interaction with subwavelength apertures. The periodic distribution of apertures shows a collective phenomenon and apparently leads to a resonant spectrum. p is chosen to be 600 nm when R_{min} is 0.002, which shows almost perfect coupling to the cavity.

4.3.2 Radii difference

In this section, p is fixed to be 600 nm and $r_e + r_i = 320$ nm. λ_r and R_{min} show their relationship with the aperture width $r_e - r_i$ in Fig. 4.8. The dip position is exponentially decaying with the aperture width, and the R_{min} value varies within the range of 0 to 0.04.

Note that, within the investigated wavelength range, λ_r remains far from the surface plasmon resonance ($\lambda_{sp}^C = 1.228 \mu\text{m}$). Thus λ_r is dominated by the guided mode resonance in the cavity, for which the phase condition is described in Eq. 4.2. Equation 4.1 supports the case that the effective refractive index n_{eff} of the TM mode depends on the slit width w ($r_e - r_i$ here). The calculated relation between n_{eff} and w is shown in Fig. 4.9 at $1.55 \mu\text{m}$. The exponential decrease of n_{eff} with the width $r_e - r_i$ is in good agreement with the decrease of λ_r with $r_e - r_i$ in Fig. 4.8. From $r_e - r_i = 20$ nm to 70 nm, n_{eff} drops by 30.5% while λ_r decreases by 18.5% for the corresponding $r_e - r_i$ range. The reduced decrease of λ_r can be interpreted from two aspects: the cavity length in the phase condition and the dispersive property of the MIM mode. In Fig. 4.4, the length $l = 2r_e - d_0$ of the cavity is elongated with increased $r_e - r_i$. A second possible reason is the slight reduction of n_{eff} with λ (Fig. 4.5).

R_{min} is maximum at $r_e - r_i = 20$ nm. The opening ($2\sqrt{2r_e d_0 - d_0^2}$) at the entrance of the aperture is minimum at $r_e - r_i = 20$ nm. Thus the minimum fill factor of the

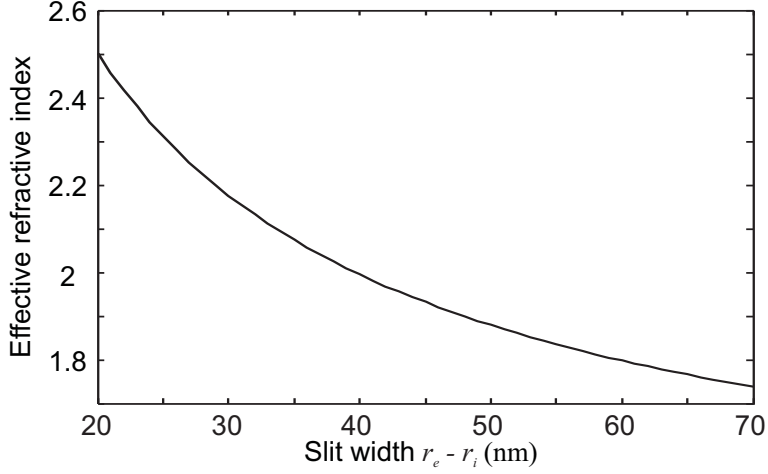


Figure 4.9: Calculated mode effective refractive index n_{eff} with different slit width w at $1.55 \mu\text{m}$ from Eq. 4.1.

opening results in minimum light injection to the cavity. The R_{min} is optimized at $r_e - r_i = 40 \text{ nm}$. To maximize the amplitude of the reflection dip, the $r_e - r_i$ is finally chosen to be 40 nm for the device design.

4.3.3 Radii sum

The radii sum $r_e + r_i$ is investigated in Fig. 4.10 considering a constant radii difference $r_e - r_i = 40 \text{ nm}$. The linear fit of λ_r covers the spectral range from $1.33 \mu\text{m}$ to $1.67 \mu\text{m}$, which is within the accurate fitting range for the Au permittivity. The mode resonance in the cavity (Eq. 4.2) explains the linear relation between λ_r and the cavity length $l = 2r_e - d_0$, which is linearly increasing with $r_e + r_i$. In the simplified model (Fig. 4.4), the width $w = r_e - r_i$ is constant during the $r_e + r_i$ variation. Since the light is well confined in the slit, the variation of the slit separation in the annular aperture influences the n_{eff} in a negligible way.

For R_{min} , at $r_e + r_i = 260 \text{ nm}$, the short separation of $\lambda_r = 1.33 \mu\text{m}$ and the SP resonance $\lambda_{sp}^C = 1.228 \mu\text{m}$ induces a large R_{min} value by negative coupling. When λ_r moves further away from the SP resonance, R_{min} decreases. A minimum value is reached for $r_e + r_i = 360 \text{ nm}$.

In conclusion, $r_e + r_i$, which is linked to the cavity length, is useful in tuning the resonance position in the expected spectrum range.

4.3.4 Cut distance

Attention has been paid to the condition $d_0 > 0$. When $d_0 < 0$, a thin metal layer in front of the cavity can effectively block light injection into the cavity. At the same time,

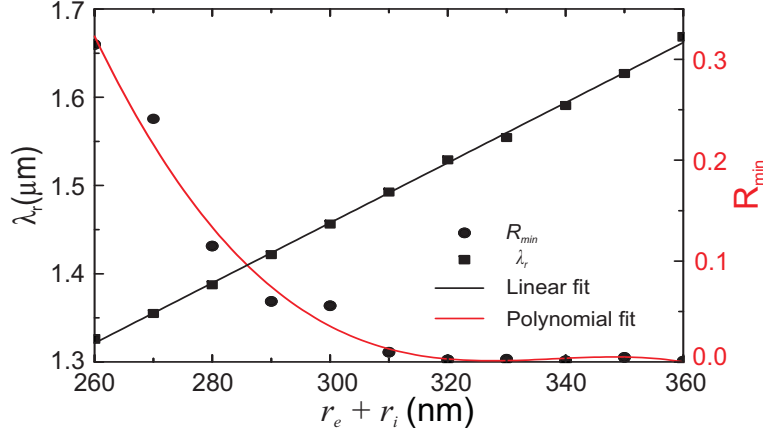


Figure 4.10: Calculated resonance position λ_r (squares) and R_{min} at λ_r (circles) for varied $r_e + r_i$. Other device parameters are the same as in Fig. 4.2.

light scattering with apertures is different from the case for $d_0 > 0$. Their reflection spectra will not be discussed.

Figure 4.11 shows the exponential decrease of λ_r with d_0 . When d_0 is increased from 10 nm to 80 nm, λ_r falls from 1.53 μm to 1.23 μm . Conversely, the R_{min} value increases from 0 to 0.53. The exponential decrease of λ_r can be explained by the cavity length and the phase at the entrance. Note that d_0 linearly influences the cavity length ($2r_e - d_0$). The λ_r position should be linearly decreasing with decreased length ($2r_e - d_0$). Additionally, the phase shift at the opening of the aperture plays an important part in the phase summation (Eq. 4.2). For $d_0 < 40$ nm, this phase is determined by $\phi = \int_{d_0}^{r_e - r_i} \mathbf{k} \cdot d\mathbf{l} = \int_{d_0}^{r_e - r_i} k_0 n_{eff}(z) dz$, in which the n_{eff} exponentially shrinks with the increase of the aperture width. As a result, the phase is large with a small d_0 . ϕ decreases more from $d_0 = 10$ nm to 20 nm than the change of ϕ from $d_0 = 20$ nm to 30 nm. ϕ is maximum at the $d_0 = 10$ nm and it decreases more slowly when d_0 is enlarged. After $d_0 = 40$ nm, the reduction of λ_r is mainly due to the decrease in cavity length. Above all, the d_0 is important in λ_r determination, especially when d_0 is small.

For R_{min} , its value is almost 0 when $d_0 \leq 40$ nm and it distinctively increases after $d > 40$ nm. The large R_{min} value is due to the interference coupling between the SP resonance and the waveguide mode resonance since λ_r moves close to the SP resonance at $\lambda_{sp}^C = 1.228 \mu\text{m}$.

4.3.5 Summary

According to the above discussion, normal incident light on the periodic annular aperture array may incur two types of resonances. One is the surface plasmon resonance at the $\text{Si}_3\text{N}_4/\text{Au}$ interface. The other is the waveguide mode resonance inside the cavity,

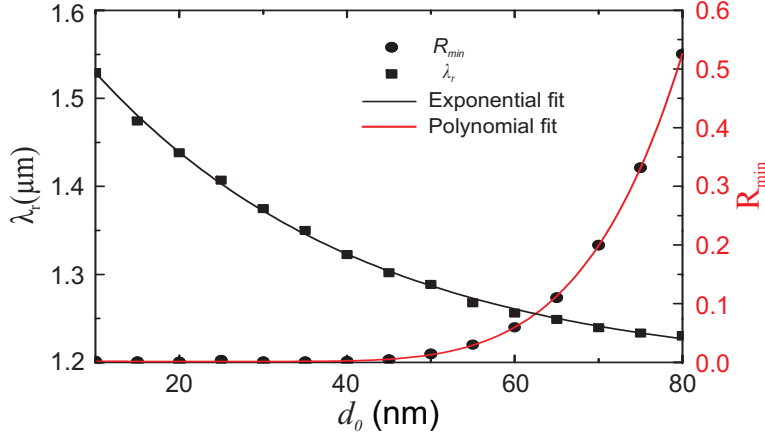


Figure 4.11: Calculated resonance position λ_r (squares) and R_{min} at λ_r (circles) for varied d_0 . Other device parameters are the same as in Fig. 4.2.

which is Fabry-Pérot like. The two resonances may result in dips in the reflection spectrum. As the device is aimed at sensing applications, the waveguide mode resonance is desirable for high field confinement in the aperture of the cavity, where the analyte will be placed. The surface plasmon is sharper and seems to be ideal for sensing. But it principally localizes most of the field in the Si_3N_4 waveguide. It is then impossible or not efficient to be applied for sensing. However, the coupling between the two resonances will induce reduction of the reflection dip amplitude, because the SPR prohibits light from injection into the cavity. As a result, the mode resonance is deteriorated by the SP excitation when they are close enough and/or overlap with each other. In the device design, the two effects should be separated far enough to achieve a desired amplitude for the reflection dip.

The periodicity p of the device is the first parameter to be considered for resonance separation. Since the SP resonance is caused by the wavevector matching from the aperture diffracted orders, the reflection spectrum critically depends on p . In addition to p , the other dimensions of the cavity including the width ($r_e - r_i$), the length ($r_e + r_i$), and the cut distance (d_0) have shown their influences on the resonance position and the coupling efficiency determination. They affect the waveguide mode resonance by altering the phase matching condition (Eq. 4.2). Either the mode effective index or the cavity length has been changed through geometry modification. The final parameters are $p = 600$ nm, $r_e = 180$ nm, $r_i = 140$ nm, $d_0 = 10$ nm. With this configuration, the spectral response of the device is a reflection dip at $\lambda_r = 1.53$ μm , with a minimal reflection $R_{min} = 0.002$ and a surface plasmon resonance at $\lambda_{sp}^C = 1.228$ μm .

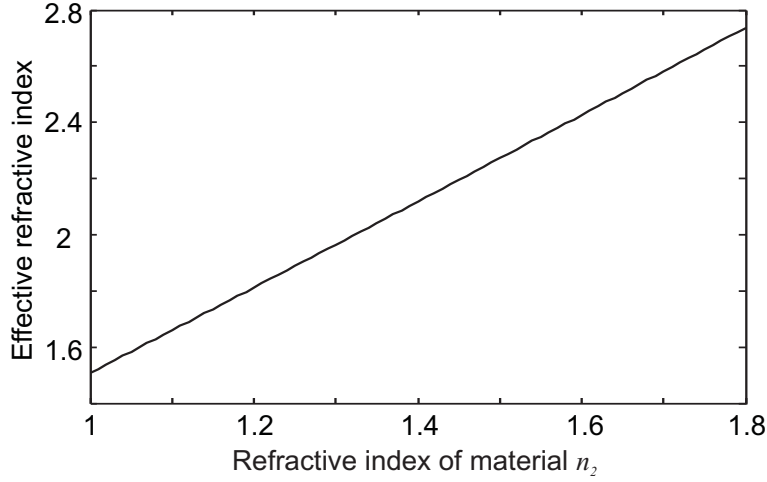


Figure 4.12: The effective refractive index n_{eff} of the TM mode supported in MIM structure in relation with the refractive index of the insulator filling the slit.

4.4 Sensing

With regard to application, the strong field confinement in the aperture of the cavity (Fig. 4.2(b)) proves the greatest interest for sensing, as light-matter interaction is enhanced by the field overlap. Thereby the analyte is intended to fill the aperture. From the parameters study, the waveguide mode resonance inside the cavity is FP-like and the phase matching condition in Eq. 4.2 presents the dependence of the resonance position on the effective refractive index n_{eff} and the cavity length. At the same time, Eq. 4.1 shows the importance of the relative permittivity of the material ε_2 in determination of n_{eff} . We can observe a linear relation between n_{eff} and the insulator refractive index $n_2 = \sqrt{\varepsilon_2}$ in Fig. 4.12.

In this case, n_{eff} of the waveguide mode critically depends on the refractive index (RI) of the analyte and thus the resonance position λ_r is shifted with the RI variation. Simulation shows that the λ_r position changes proportionally with n_2 , described in Fig. 4.13. The linear fit determines a sensitivity of 764 nm/RIU (refractive index unit). R_{min} , the reflection at the dip position, for $n_2 = 1.0$ is high due to the SP resonance ($\lambda_{sp}^C = 1.228 \mu\text{m}$) interference on the waveguide mode resonance. Then R_{min} decreases with further separation from SPR, which means the light localization and absorption in the cavity have been improved.

4.5 3D Simulation for Fabrication Consideration

The above calculations have been made for a two dimensional (2D) structure, which is infinite in the y direction. From 2D to real device fabrication, the annular aperture

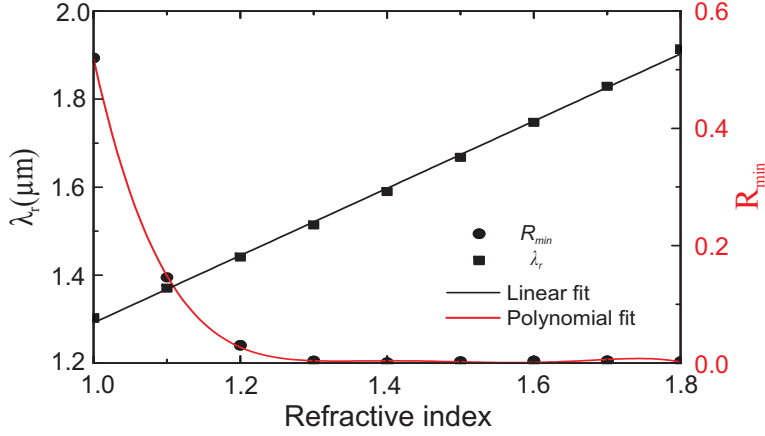


Figure 4.13: Optical property variation with different material refractive index filling in the annular aperture. The resonance position λ_r is linearly related with the material index. R_{min} is the reflection at the resonance dip.

array should have a finite thickness. Three dimensional (3D) simulations are made on the structure with the transverse view through the cavity center shown in Fig. 4.14. From the fabrication point of view, the Au deposition and Si_3N_4 etching are crucial and not trivial. The first idea was to have a gold thickness equal to the height of the waveguide. Experimental attempts have shown that: first the surface state of the metal layer is rough and second the lift-off process is not efficient and the structure is easily destroyed during this fabrication step. Consequently, we propose to fabricate a thinner gold layer. In this case, a compromise has to be found between the thickness of the structure (which has to be minimum), the overlap of the optical mode with the cavity, and finally the position (in the z direction) of the cavity. We define h_1 as the thickness of the gold film and h_2 as the residual Si_3N_4 layer. Water fills the aperture and the surface of the device. Light is injected to the Si_3N_4 waveguide and propagates through to reach the Au cavity. Since light must be well confined in the Si_3N_4 waveguide and considering fabrication difficulties in deep Si_3N_4 etching and Au deposition, its thickness is important. The thickness of the Si_3N_4 waveguide is set to be 340 nm, which is close to the value of $\lambda/2n_{\text{Si}_3\text{N}_4}$ for light confinement.

From 2D to 3D configuration, incidence is no longer homogeneously distributed in the y direction. The calculated electric field profile in such a waveguide is outlined in Fig. 4.14. The optical response results from light interaction with different materials at the cavity region.

In the ideal case, $h_1 = 340$ nm, $h_2 = 0$. The geometrical parameters are those obtained thanks to the 2D simulations presented above: $p = 600$ nm, $d_0 = 10$ nm, $r_i = 140$ nm, $r_e = 180$ nm, $d_1 = 150$ nm. The reflection spectrum is given in Fig. 4.15. One can remark that the surface plasmon resonance remains, even if it is slightly blue shifted

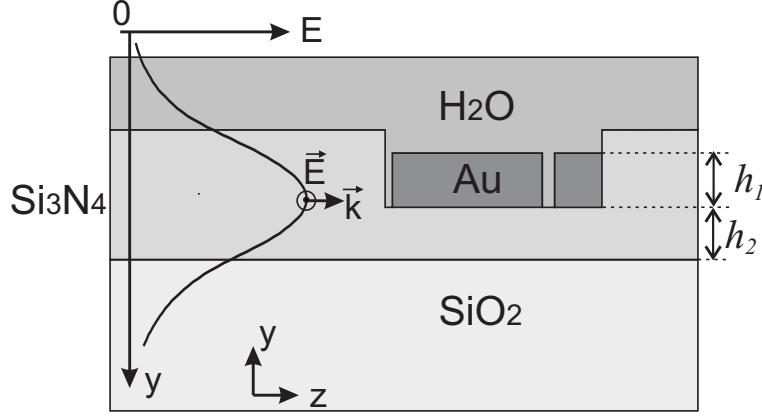


Figure 4.14: Transverse view of the 3D AAA structure. The electric field profile in the Si_3N_4 waveguide is schemed by the solid curve. Light propagates in the z direction.

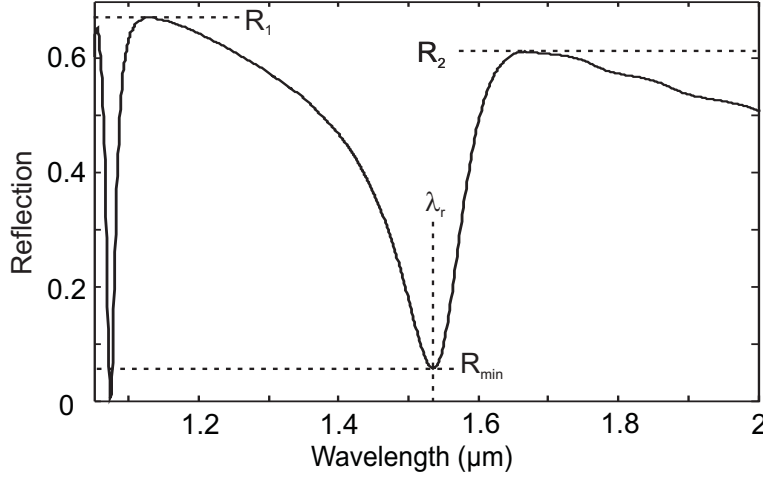


Figure 4.15: Calculated reflection spectrum for 3D structure shown in Fig. 4.14.

compared to the 2D simulation. The shape of the reflection corresponding to the guided mode resonance is now asymmetric and the minimal reflection R_{min} has increased from 0.002 to 0.057. The overall amplitude of the spectrum is lower. Moreover, the resonance is slightly red shifted (from $1.53 \mu\text{m}$ to $1.535 \mu\text{m}$). To characterize the amplitude of the reflection dip, we introduce two new values, R_1 and R_2 , corresponding respectively to the basis of the dip on the left and right side. The amplitude of the dip A_{dip} is then defined as the minimum value between the differences $(R_1 - R_{min})$ and $(R_2 - R_{min})$.

For different h_1 and h_2 conditions, λ_r , and A_{dip} are listed in tables 4.1, respectively. The field overlap between the incident mode and the Au cavity is also given in the table at a constant wavelength $\lambda = 1.55 \mu\text{m}$. The discrete selected h_1 and h_2 satisfy the condition $h_1 + h_2 \leq 340 \text{ nm}$.

4. ANNULAR APERTURE ARRAY

Table 4.1: Simulation results for 3D AAA structures with discrete values of h_1 and h_2 .

(a) Reflection dip position λ_r (Unit: μm)						
	h_2 (nm)					
h_1 (nm)	0	20	60	100	140	180
140	1.49	1.561	1.594	1.612	1.59	1.585
180	1.518	1.577	1.599	1.615	1.592	
220	1.529	1.578	1.601	1.608		
260	1.539	1.585	1.599			
300	1.543	1.579				
340	1.535					

(b) Reflection dip amplitude A_{dip}						
	h_2 (nm)					
h_1 (nm)	0	20	60	100	140	180
140	0.054	0.081	0.095	0.127	0.05	0.035
180	0.15	0.184	0.186	0.186	0.134	
220	0.294	0.326	0.289	0.238		
260	0.416	0.416	0.367			
300	0.493	0.494				
340	0.555					

(c) Field overlap calculation at $1.55 \mu\text{m}$						
	h_2 (nm)					
h_1 (nm)	0	20	60	100	140	180
140	0.273	0.292	0.321	0.330	0.321	0.293
180	0.368	0.388	0.412	0.412	0.388	
220	0.462	0.479	0.493	0.479		
260	0.549	0.561	0.561			
300	0.624	0.628				
340	0.684					

Note that the results for deposited Au thickness $h_1 < 140$ nm are not shown in the table, as the dip is not significant. Indeed, for $h_1 = 20$ nm and 60 nm, there is no reflection dip at all. When $h_1 = 100$ nm, the maximum A_{dip} is still less than 0.04, which can be ignored for device realization. By comparing the λ_r , A_{dip} and field overlap variation in the table, the influence of the geometrical dimensions of the structure can be discussed.

First, the relative position of the Au cavity in the waveguide is varied while the Au cavity maintains a fixed layer depth h_1 . λ_r is varied by the residual Si_3N_4 layer h_2 . For example, with $h_1 = 180$ nm, h_2 is increased from 0 to 140 nm. From $h_2 = 0$ to 20 nm, λ_r shows a red shift of 59 nm, which is the maximum shift compared with the increase of h_2 from 20 nm to larger values. This phenomenon exists for the other values of Au thickness h_1 in the table. The big change of λ_r , varying from $h_2 = 0$ to 20 nm, is due to the fact that the residual Si_3N_4 layer increases the n_{eff} of the supported TM mode in the MIM slit. With a finite-thick MIM slit on a substrate, the substrate refractive index is yet another vital parameter which determines the n_{eff} of the confined mode in the slit. This effect is verified by the discussion of the effect of the SiO_2 substrate on slot mode in Chapter 3. As a result, λ_r increases with h_2 until $h_2 = 100$ nm, for which the value of n_{eff} saturates.

Second, A_{dip} shows the impact of h_2 on the amount of light injected to the cavity. For $h_1 = 140$ nm, A_{dip} is maximum at $h_2 = 100$ nm. This is because of the non-homogeneous distribution of the incident field over the Si_3N_4 waveguide. As predicted, A_{dip} is apparently larger when Au is centered on the Si_3N_4 waveguide mode. Indeed, the field overlap between the incident field and the cavity is maximum.

Third, comparisons of A_{dip} and λ_r are made for h_1 variation with fixed h_2 . A_{dip} shows a large dependence on Au thickness. By comparing A_{dip} and the field overlap in the table, A_{dip} is clearly proportional to the field overlap between the incident mode and the Au cavity and thereby their values apparently increase with h_1 in the table. For the resonance position, the λ_r shift is maximum from $h_1 = 140$ nm to 180 nm with $h_2 = 0$, meaning that the n_{eff} of the MIM slot mode is influenced to a maximum when h_1 is small. In the case of MIM deposition on a substrate, n_{eff} is approaching specific values with increasing Au thickness, depending on the refractive index of the substrate.

In conclusion, one can remark that both the resonance position λ_r and the reflection dip amplitude A_{dip} are strongly dependent on the Au thickness and the relative position between the mode of the Si_3N_4 waveguide and the cavity. λ_r is shifted as a result of the modification of the mode distribution in the substrate and A_{dip} is proportional to the amount of light injected into the cavity. In practise, the structure geometry shall be chosen to optimize A_{dip} and the field amount for sensing:

- $h_1 \geq 220$ nm, the deposited Au layer must be sufficiently thick to guarantee the amplitude of the reflection dip to be characterizable ($A_{dip} \geq 30\%$).

- In order to maximize A_{dip} , centering the Au cavity with the Si_3N_4 waveguide mode in the y direction is essential to obtain a better coupling of light into the cavity.

4.6 Conclusion

In this chapter, the annular aperture array in Au film has been embedded in a Si_3N_4 waveguide for a planar configuration. Its resonant working mechanism is studied as well as the influence of dimensional deviations. There exist two main resonances: the SP resonance at the $\text{Si}_3\text{N}_4/\text{Au}$ interface and the waveguide mode resonance in the aperture. Herein the interference coupling among the two resonances is the result of a scattered surface wave interference. The SP excitation blocks light injection into the aperture array, thus decreasing the waveguide mode resonance.

As for applications, the waveguide mode resonance is applicable for material sensing. The sensing mechanism benefits from the field localization in the aperture to enhance local light-matter interaction. The theoretical sensitivity is 764 nm/RIU, along with advantages of small sensing area and device compatibility with other planar devices. Clearly, the sensitivity is comparable with other resonance based sensors, which have been described in chapter 2. Another important characteristic of sensors: resolution is not considered for the theoretical study, because the resolution depends on the measurement system and the post-processing methods. Details have been discussed in chapter 3.

Even a rectangular cavity (Fig. 4.4) can realize the same function as the annular aperture. However, the choice of the annular aperture is due to the flexibility of an expanded parameter variations. Second, one of the most interesting aspects of the annular aperture is the strong field localization at the entrance of the cavity. By controlling the cut distance, the field can be further enhanced which is interesting for local and minute volume detection.

Finally, the realization issues of the device are considered in three dimensional computation. It provides some insights into the limits of the device geometry to preserve the desired optical properties.

Chapter 5

Conclusion

Following developments in biotechnology and medicine, optical sensing promises to be undoubtedly important in various applications such as pharmaceutical discovery, environmental monitoring, and others. While fluorescence based sensors demand laborious labeling processes, refractive index (RI) based label-free sensing is straightforward to monitor or analyze the physical and chemical properties of substances. Among the diverse structures used to realize RI based sensors, nano-structured metallic devices are an interesting platform as device miniaturization and sensor multiplexing can be achieved on the same substrate. In this thesis, subwavelength dimensional metallic structures are studied for RI sensing.

Subwavelength size metallic nanostructures have the ability to confine and enhance the electromagnetic field in volumes smaller than the diffraction limit. We have studied the optical properties of periodically structured Au films and explored their application for local RI sensing. The structured Au film is then integrated with a dielectric waveguide using one of two methods. In the first case, the slot waveguide cavity (SWC) device, the cavity is fabricated above a Si waveguide for the purpose of coupling via the evanescent field. In the second case, the annular aperture array (AAA) device, the cavity is directly embedded in a Si_3N_4 waveguide.

The planar configuration provides additional possibilities for sensor multiplexing and compact system development. Theoretical modeling, fabrication and characterization of the SWC devices have been carried out and the AAA structure is studied using theoretical computation.

The SWC is a gold film structured with a subwavelength periodic slot array, for which the dimensions are: slot width 30 nm, thickness of the Au layer 20 nm, and cavity length 700 nm. The slot is able to localize the electromagnetic field by abrupt variation of the permittivity at the Au/dielectric interface. The Au cavity is deposited on a Si waveguide where the evanescent field overlap correlates the optical response of the cavity with that of the Si waveguide. When the coupling is enhanced by the

5. CONCLUSION

Fabry-Pérot (FP) like resonance of the cavity, the transmission spectrum of the Si waveguide displays a dip. With the given design parameters, 14.6% of the incident light is theoretically coupled from the Si waveguide to the cavity in air. Note that the coupling can be improved with an enhanced field overlap in the slot. With water infiltration in the cavity, the coupling is improved to 31.6%. The sensing mechanism is based on the sensitivity of the FP resonance to the environment of the slot array and thus the variation of the resonance condition is directly linked to the RI of the analyte. The resonator achieves a sensitivity of 726 nm/RIU (refractive index unit) in the liquid environment. After device fabrication, which was carried out by Armando Cosentino (OPT Laboratory, EPFL), experimental characterization demonstrated that the transmission spectrum of the Si waveguide shifts with the RI of different liquids. The experimental sensitivity, 730 ± 10 nm/RIU, is in good agreement with the theory. The resolution of the RI measurement is estimated to be 5.8×10^{-4} RIU from the experimental results. Moreover, improvement of the resolution has been discussed by sequential post-processing steps on the experimental spectrum: Fourier transform (FT) filtering, 1st order derivative implementation, and measurement averaging. The post-processing methods are important to enhance the signal-to-noise ratio (SNR) and reduce the measurement error in the spectral tracking. Finally, an optimum resolution of 5.8×10^{-5} RIU is anticipated for the RI detection.

The AAA structured Au film is embedded in a Si₃N₄ waveguide. With an in-plane incidence, the FP-like resonance of the Au cavity results in a reflection resonance. Thus the resonance enables the device to be implemented for RI sensing using resonance shifts. Within a wide RI range, the theoretical sensitivity is 764 nm/RIU around $\lambda = 1.55$ μ m. Furthermore, the theoretical study establishes the requirements of the device geometry when device fabrication is considered. Due to fabrication difficulties in partial Si₃N₄ etching control and Au cavity deposition, experimental demonstration has not yet been undertaken.

The two devices investigated present similar sensitivities as Fabry-Pérot cavity based sensors. In comparison to a resonator based dielectric sensor, for example, a ring resonator or a photonic crystal based sensor, the SWC and AAA devices have comparable sensitivities. However, the strong absorption of the metal leads to a much lower quality factor of the resonance. Thus the resolution, in principle, is not comparable to a microcavity. Nevertheless, the metallic cavities exhibit field confinement in the nano scale, which makes the nano-structured device interesting for local detection. When the SWC and AAA devices are compared with plasmonic nanoparticles, the sensitivities are similar or even superior. The integration with dielectric waveguides enables detection in configurations or positions which may not be accessible for nanoparticle sensors.

This thesis is dedicated to investigating a sensing platform which combines nano-patterned metallic cavities and dielectric waveguides. In a planar configuration, the optical functionality of the cavity is coupled to the dielectric waveguide for a simple method of detection. Moreover, the work presented in this thesis intends to bridge the dimension difference between photonic devices and plasmonic structures for future developments of complex optical systems.

From the development point of view, the cavities presented here, especially the SWC device, permit several possibilities for future enhancement. First, the characterization setup could be optimized to simplify the post-processing steps which are performed on the experimental transmission spectrum. Several methods have been considered: (1) using lensed fibers for enhanced light injection and collection; (2) improving polarization control in the system; (3) replacing the fiber injection and collection with grating couplers so that the influence of FP resonances in the waveguide is minimized. It is also essential to optimize the signal-to-noise ratio (SNR) of the measurement and the measurement error. Once the resonance shift can be directly determined without lengthy post-processing steps, the real-time tracking of analytes can enable widespread applications in bio/chemical monitoring, such as concentration detection of molecules. Second, cascaded cavities are a potential approach for sensor multiplexing with a single waveguide. The placement of different cavities on one waveguide results in multiple transmission resonances, which can be implemented for different analytes. Third, a periodic array can be reduced to a single slot or a single aperture cavity for single molecule detection or sample analysis with a minute volume. The minute cavity volume enables a local variation of RI in many applications, such as nanoscale imaging.

Nanopatterned metallic structures are capable of manipulating light on nanoscale dimensions. For example, metallic nanostructures can be used to confine light to very small volumes, which could have a wide range of potential applications. One such application is RI sensing, as discussed in this thesis. Other example applications include enhancement of Raman scattering, nano lithography, and nanoscale optical microscopy. Future exploration of useful devices requires mastery of modeling tools and the device development processes to engineer the optical field in a sufficiently elaborate manner. Through field engineering, the resulting effective optical properties may exceed the intrinsic properties of the constituent materials. For example, metamaterials (negative refractive index materials, *etc.*) and optical nonlinearity enhancement are attractive application spaces for developing novel devices. Finally, device integration is another essential aspect in the development of optical systems. Device development based on Si technology permits compatibility with CMOS fabrication. Furthermore, the integration of different Si based components suggests the possibility of realizing complex optical systems, for example, photonic circuits. As for sensors, parallel sensing using compatible sensors on the same substrate is important for the realization of portable

5. CONCLUSION

and low-cost sensor systems. Above all, the design of optical devices based on engineering the interaction of light with metallic nanostructures can be a significant challenge. However, as the RI sensing results presented in this thesis suggest, these challenges can be overcome with the development of appropriate modeling and device design tools, producing innovative, useful optical devices with an extremely broad range of potential applications.

Appendix A

Standard deviation of amplitude noise

In this thesis, the standard deviation of the amplitude noise σ_{amp} is approximated from a statistical analysis by Ref. [9]. Herein σ_{amp} applies for the extremum position tracking and it is related to the quality factor (Q) and signal-to-noise ratio (SNR) of the peak by:

$$\sigma_{amp} \approx \frac{\lambda}{4.5Q(SNR^{0.25})} \quad (A.1)$$

The approximation process of σ_{amp} is given in the following:

1. Assuming a Lorentzian shaped resonance with a maximum value at λ_0 .
2. Random amplitude noise from a white Gaussian distribution is added to the resonance profile.
3. Monte Carlo simulation calculates the maximum position for the resulting profile at λ_c .
4. The deviation δ of the maximum position from the actual maximum center is governed by $\delta = \lambda_c - \lambda$.
5. Steps 2, 3 and 4 are repeated to get a set of data for deviations δ .
6. The standard deviation σ is decided based on the data set from step 5.
7. Q and SNR conditions are varied to check the change of the standard deviation.
8. The extracted standard deviations are used to approximate its relationship with Q of the resonance and SNR of the signal, shown by Eq. A.1.

Note that Eq. A.1 is applicable to RI sensors where the measured extremum value is used to identify the spectral location of the resonant mode. In particular, this approximation is helpful for resonant RI sensors having a high Q . For a low Q system, post-processing of the achieved spectrum will improve the standard deviation a lot.

A. STANDARD DEVIATION OF AMPLITUDE NOISE

Appendix B

Drude model verification

In the thesis, the dispersion property of Au is modeled by the Drude model. In the Drude model: $\varepsilon_{Au} = 1.0 - \omega_p^2 / (\omega^2 - i\omega\gamma)$, ω is the angular frequency, the bulk plasma frequency is $\omega_p = 1.2 \times 10^{16} \text{ s}^{-1}$, and the damping rate is $\gamma = 1.25 \times 10^{14} \text{ s}^{-1}$. The aim of this appendix is to verify that the selected Drude model preserves calculation accuracy with respect to the Au dispersion property.

Firstly, the real and imaginary part of the Au relative permittivity are shown in Fig. B.1 from the Drude model in comparison with the experimental values from Palik [103]. The chosen coefficients allow a fit to be in good agreement with the experimental values of the material in the wavelength range of interest (1.3 μm to 2.4 μm).

Next, the discrepancy of the relative permittivity is proven not to affect the major property of the SWC device. By point-by-point calculation at the discrete experimental values of ε_{Au} , the transmission spectrum obtained is compared with the single Drude model used in this thesis. Fig. B.2 shows the result for the device in Fig. 3.2. Clearly, the use of the simplified Drude model does not modify the response of the structure drastically.

B. DRUDE MODEL VERIFICATION

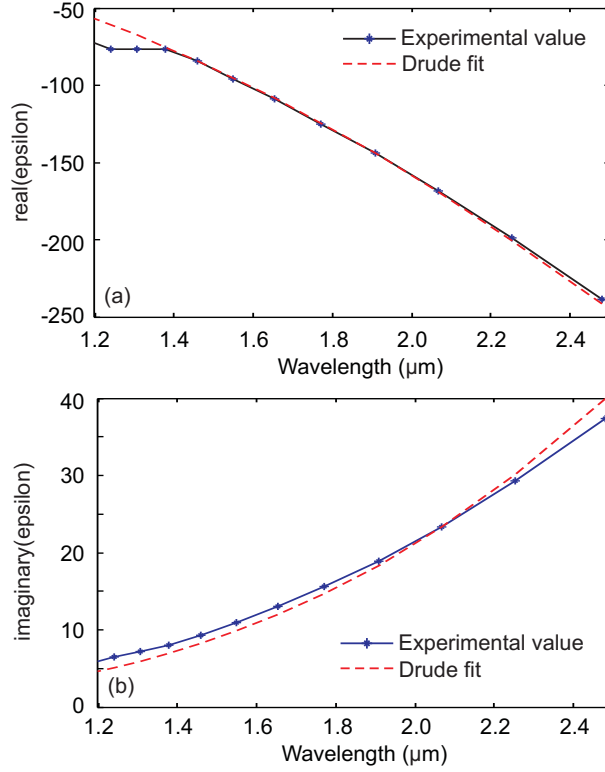


Figure B.1: Drude fitting of Au relative permittivity in comparison with the experimental values from Ref. [103]: (a) Real part of the relative permittivity; (b) imaginary part of the relative permittivity.

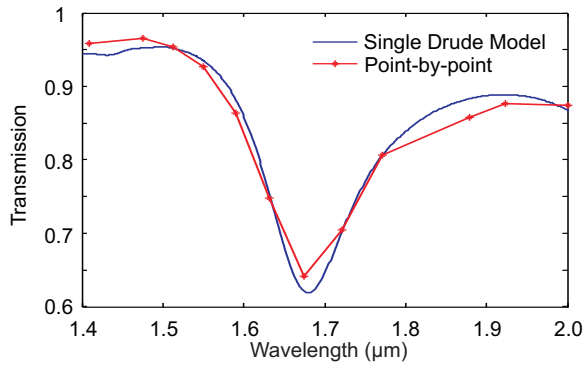


Figure B.2: Calculated transmission spectrum comparison between single Drude model fitting and point-by-point simulations for the experimental values of ϵ_{Au} (device in Fig. 3.2).

Bibliography

- [1] J. Haus, *Optical Sensors: Basics and Applications*. Wiley-VCH Verlag Gmbh & Co. KGaA, Weinheim, 2010. 1, 6
- [2] W. E. Moerner, “New directions in single-molecule imaging and analysis,” *Proceedings of the National Academy of Sciences of the United States of America*, vol. 104, no. 31, pp. 12596–12602, 2007. 1, 23
- [3] K. Kneipp, Y. Wang, H. Kneipp, L. T. Perelman, I. Itzkan, R. R. Dasari, and M. S. Feld, “Single molecule detection using surface-enhanced Raman scattering (SERS),” *Physical Review Letters*, vol. 78, pp. 1667–1670, 1997. 1, 23
- [4] X. D. Fan, I. M. White, S. I. Shopova, H. Y. Zhu, J. D. Suter, and Y. Z. Sun, “Sensitive optical biosensors for unlabeled targets: A review,” *Analytica Chimica Acta*, vol. 620, no. 1-2, pp. 8–26, 2008. 1, 11, 18, 19, 20, 23, 31
- [5] J. Fraden, *Handbook of Modern Sensors: Physics, Designs, and Applications*. Springer-Verlag, Inc., 3rd ed., 2004. 2, 6
- [6] J. Homola, “Surface plasmon resonance sensors for detection of chemical and biological species,” *Chemical Reviews*, vol. 108, no. 2, pp. 462–493, 2008. 2, 9, 12, 23
- [7] G. Gauglitz, “Direct optical detection in bioanalysis: an update,” *Analytical and Bioanalytical Chemistry*, vol. 398, pp. 2363–2372, 2010. 2, 11
- [8] T. Vo-Dinh, ed., *Biomedical Photonics Handbook*, vol. 3. CRC Press LLC, 2003. 5, 6, 11
- [9] I. M. White and X. Fan, “On the performance quantification of resonant refractive index sensors,” *Optics Express*, vol. 16, no. 2, pp. 1020–1028, 2008. 10, 67, 99
- [10] D. Erickson, S. Mandal, A. Yang, and B. Cordovez, “Nanobiosensors: optofluidic, electrical and mechanical approaches to biomolecular detection at the nanoscale,” *Microfluidics and Nanofluidics*, vol. 4, pp. 33–52, 2008. 11

BIBLIOGRAPHY

- [11] M. A. Cooper, “Optical biosensors: where next and how soon?,” *Drug Discovery Today*, vol. 11, no. 23-24, pp. 1061–1067, 2006. 11
- [12] C. Nylander, B. Liedberg, and T. Lind, “Gas detection by means of surface plasmon resonance,” *Sensors and Actuators*, vol. 3, pp. 79 – 88, 1982-1983. 12
- [13] J. Homola, S. S. Yee, and G. Gauglitz, “Surface plasmon resonance sensors: review,” *Sensors and Actuators B: Chemical*, vol. 54, no. 1-2, pp. 3–15, 1999. 12, 31
- [14] J. Homola, “Present and future of surface plasmon resonance biosensors,” *Analytical and Bioanalytical Chemistry*, vol. 377, no. 3, pp. 528–539, 2003. 12, 31
- [15] R. Slavik, J. Homola, J. Ctyroky, and E. Brynda, “Novel spectral fiber optic sensor based on surface plasmon resonance,” *Sensors and Actuators B: Chemical*, vol. 74, no. 1-3, pp. 106–111, 2001. 13, 15
- [16] J. Homola, I. Koudela, and S. S. Yee, “Surface plasmon resonance sensors based on diffraction gratings and prism couplers: sensitivity comparison,” *Sensors and Actuators B: Chemical*, vol. 54, no. 1-2, pp. 16 – 24, 1999. 14
- [17] Website, “<http://www.biacore.com/lifesciences/index.html>.” 14, 71
- [18] A. V. Kabashin, S. Patskovsky, and A. N. Grigorenko, “Phase and amplitude sensitivities in surface plasmon resonance bio and chemical sensing,” *Optics Express*, vol. 17, no. 23, pp. 21191–21204, 2009. 14
- [19] Y. C. Li, Y. F. Chang, L. C. Su, and C. Chou, “Differential-phase surface plasmon resonance biosensor,” *Analytical Chemistry*, vol. 80, no. 14, pp. 5590–5595, 2008. 14
- [20] Y. H. Huang, H. P. Ho, S. Y. Wu, S. K. Kong, W. W. Wong, and P. Shum, “Phase sensitive SPR sensor for wide dynamic range detection,” *Optics Letters*, vol. 36, no. 20, pp. 4092–4094, 2011. 14
- [21] M. Piliarik and J. Homola, “Surface plasmon resonance (SPR) sensors: approaching their limits?,” *Optics Express*, vol. 17, no. 19, pp. 16505–16517, 2009. 14
- [22] V. Kodoyianni, “Label-free analysis of biomolecular interactions using SPR imaging,” *Biotechniques*, vol. 50, no. 1, pp. 32–40, 2011. 14
- [23] M. Piliarik, M. Vala, I. Tichy, and J. Homola, “Compact and low-cost biosensor based on novel approach to spectroscopy of surface plasmons,” *Biosensors and Bioelectronics*, vol. 24, no. 12, pp. 3430–3435, 2009. 14

- [24] M. Vala, K. Chadt, M. Piliarik, and J. Homola, "High-performance compact SPR sensor for multi-analyte sensing," *Sensors and Actuators B: Chemical*, vol. 148, no. 2, pp. 544–549, 2010. 14
- [25] A. K. Sharma, R. Jha, and B. D. Gupta, "Fiber-optic sensors based on surface plasmon resonance: A comprehensive review," *IEEE Sensors Journal*, vol. 7, no. 7-8, pp. 1118–1129, 2007. 15
- [26] Y. Shevchenko, T. J. Francis, D. A. D. Blair, R. Walsh, M. C. DeRosa, and J. Albert, "In situ biosensing with a surface plasmon resonance fiber grating aptasensor," *Analytical Chemistry*, vol. 83, no. 18, pp. 7027–7034, 2011. 15
- [27] R. Slavik and J. Homola, "Ultrahigh resolution long range surface plasmon-based sensor," *Sensors and Actuators B: Chemical*, vol. 123, no. 1, pp. 10 – 12, 2007. 15, 31
- [28] M. Vala, S. Etheridge, J. Roach, and J. Homola, "Long-range surface plasmons for sensitive detection of bacterial analytes," *Sensors and Actuators B: Chemical*, vol. 139, no. 1, pp. 59 – 63, 2009. 15
- [29] F. Giorgis, E. Descrovi, C. Summonte, L. Dominici, and F. Michelotti, "Experimental determination of the sensitivity of Bloch surface waves based sensors," *Optics Express*, vol. 18, no. 8, pp. 8087–8093, 2010. 15, 16
- [30] V. Paeder, V. Musi, L. Hvozdar, S. Herminjard, and H. P. Herzig, "Detection of protein aggregation with a Bloch surface wave based sensor," *Sensors and Actuators B: Chemical*, vol. 157, no. 1, pp. 260–264, 2011. 15
- [31] R. Cush, J. M. Cronin, W. J. Stewart, C. H. Maule, J. Molloy, and N. J. Goddard, "The resonant mirror - a novel optical biosensor for direct sensing of biomolecular interactions 1. principle of operation and associated instrumentation," *Biosensors and Bioelectronics*, vol. 8, no. 7-8, pp. 347–353, 1993. 16
- [32] N. J. Goddard, D. Pollard-Knight, and C. H. Maule, "Real-time biomolecular interaction analysis using the resonant mirror sensor," *Analyst*, vol. 119, no. 4, pp. 583–588, 1994. 16
- [33] J. Hulme, C. Malins, K. Singh, P. R. Fielden, and N. J. Goddard, "Internally-referenced resonant mirror for chemical and biochemical sensing," *Analyst*, vol. 127, no. 9, pp. 1233–1236, 2002. 16
- [34] M. Zourob, S. Mohr, B. J. T. Brown, P. R. Fielden, M. B. McDonnell, and N. J. Goddard, "An integrated metal clad leaky waveguide sensor for detection of bacteria," *Analytical Chemistry*, vol. 77, no. 1, pp. 232–242, 2005. 16

BIBLIOGRAPHY

- [35] N. Skivesen, R. Horvath, S. Thinggaard, N. B. Larsen, and H. C. Pedersen, “Deep-probe metal-clad waveguide biosensors,” *Biosensors and Bioelectronics*, vol. 22, no. 7, pp. 1282–1288, 2007. 16
- [36] Z. H. He, F. Tian, Y. N. A. Zhu, N. Lavlinskaia, and H. Du, “Long-period gratings in photonic crystal fiber as an optofluidic label-free biosensor,” *Biosensors and Bioelectronics*, vol. 26, no. 12, pp. 4774–4778, 2011. 17, 18
- [37] K. M. Zhou, X. F. Chen, L. Zhang, and I. Bennion, “Implementation of optical chemsensors based on HF-etched fibre Bragg grating structures,” *Measurement Science & Technology*, vol. 17, no. 5, pp. 1140–1145, 2006. 17
- [38] K. Schroeder, W. Ecke, R. Mueller, R. Willsch, and A. Andreev, “A fibre Bragg grating refractometer,” *Measurement Science & Technology*, vol. 12, no. 7, pp. 757–764, 2001. 17, 31
- [39] A. M. Vengsarkar, P. J. Lemaire, J. B. Judkins, V. Bhatia, T. Erdogan, and J. E. Sipe, “Long-period fiber gratings as band-rejection filters,” *Journal of Lightwave Technology*, vol. 14, no. 1, pp. 58–65, 1996. 17
- [40] X. Shu, L. Zhang, and I. Bennion, “Sensitivity characteristics of long-period fiber gratings,” *Journal of Lightwave Technology*, vol. 20, no. 2, p. 255, 2002. 17
- [41] X. F. Chen, K. M. Zhou, L. Zhang, and I. Bennion, “Dual-peak long-period fiber gratings with enhanced refractive index sensitivity by finely tailored mode dispersion that uses the light cladding etching technique,” *Applied Optics*, vol. 46, no. 4, pp. 451–455, 2007. 18
- [42] X. F. Chen, L. Zhang, K. M. Zhou, E. Davies, K. Sugden, I. Bennion, M. Hughes, and A. Hine, “Real-time detection of DNA interactions with long-period fiber-grating-based biosensor,” *Optics Letters*, vol. 32, no. 17, pp. 2541–2543, 2007. 18
- [43] P. Pilla, P. F. Manzillo, V. Malachovska, A. Buosciolo, S. Campopiano, A. Cutolo, L. Ambrosio, M. Giordano, and A. Cusano, “Long period grating working in transition mode as promising technological platform for label-free biosensing,” *Optics Express*, vol. 17, no. 22, pp. 20039–20050, 2009. 18
- [44] L. Rindorf, J. B. Jensen, M. Dufva, L. H. Pedersen, P. E. Hoiby, and O. Bang, “Photonic crystal fiber long-period gratings for biochemical sensing,” *Optics Express*, vol. 14, no. 18, pp. 8224–8231, 2006. 18

- [45] Z. H. He, Y. N. Zhu, and H. Du, “Long-period gratings inscribed in air- and water-filled photonic crystal fiber for refractometric sensing of aqueous solution,” *Applied Physics Letters*, vol. 92, no. 4, p. 044105, 2008. 18
- [46] P. Wang, G. Brambilla, M. Ding, Y. Semenova, Q. Wu, and G. Farrell, “High-sensitivity, evanescent field refractometric sensor based on a tapered, multimode fiber interference,” *Optics Letters*, vol. 36, no. 12, pp. 2233–2235, 2011. 18
- [47] F. Xu, P. Horak, and G. Brambilla, “Optical microfiber coil resonator refractometric sensor: erratum,” *Optics Express*, vol. 15, no. 15, pp. 9385–9385, 2007. 18
- [48] F. Xu, P. Horak, and G. Brambilla, “Optical microfiber coil resonator refractometric sensor,” *Optics Express*, vol. 15, no. 12, pp. 7888–7893, 2007. 18
- [49] X. Guo and L. M. Tong, “Supported microfiber loops for optical sensing,” *Optics Express*, vol. 16, no. 19, pp. 14429–14434, 2008. 18
- [50] H. K. Hunt and A. M. Armani, “Label-free biological and chemical sensors,” *Nanoscale*, vol. 2, no. 9, pp. 1544–1559, 2010. 19, 22
- [51] A. M. Armani and K. J. Vahala, “Heavy water detection using ultra-high-Q microcavities,” *Optics Letters*, vol. 31, no. 12, pp. 1896–1898, 2006. 20
- [52] H. Li and X. Fan, “Characterization of sensing capability of optofluidic ring resonator biosensors,” *Applied Physics Letters*, vol. 97, no. 1, p. 011105, 2010. 20
- [53] F. Vollmer and S. Arnold, “Whispering-gallery-mode biosensing: label-free detection down to single molecules,” *Nature Methods*, vol. 5, no. 7, pp. 591–596, 2008. 19
- [54] Y. Z. Sun and X. D. Fan, “Optical ring resonators for biochemical and chemical sensing,” *Analytical and Bioanalytical Chemistry*, vol. 399, no. 1, pp. 205–211, 2011. 19
- [55] T. Yoshie, L. L. Tang, and S. Y. Su, “Optical microcavity: Sensing down to single molecules and atoms,” *Sensors*, vol. 11, no. 2, pp. 1972–1991, 2011. 19
- [56] K. De Vos, J. Girones, T. Claes, Y. De Koninck, S. Popelka, E. Schacht, R. Baets, and P. Bienstman, “Multiplexed antibody detection with an array of silicon-on-insulator microring resonators,” *IEEE Photonics Journal*, vol. 1, no. 4, pp. 225–235, 2009. 19

BIBLIOGRAPHY

- [57] D.-X. Xu, M. Vachon, A. Densmore, R. Ma, A. Del  ge, S. Janz, J. Lapointe, Y. Li, G. Lopinski, D. Zhang, Q. Y. Liu, P. Cheben, and J. H. Schmid, “Label-free biosensor array based on silicon-on-insulator ring resonators addressed using a WDM approach,” *Optics Letters*, vol. 35, no. 16, pp. 2771–2773, 2010. 19
- [58] V. R. Almeida, Q. Xu, C. A. Barrios, and M. Lipson, “Guiding and confining light in void nanostructure,” *Optics Letters*, vol. 29, no. 11, pp. 1209–1211, 2004. 19
- [59] C. A. Barrios, M. J. Banuls, V. Gonzalez-Pedro, K. B. Gylfason, B. Sanchez, A. Griol, A. Maquieira, H. Sohlstrom, M. Holgado, and R. Casquel, “Label-free optical biosensing with slot-waveguides,” *Optics Letters*, vol. 33, no. 7, pp. 708–710, 2008. 19
- [60] C. F. Carlborg, K. B. Gylfason, A. Kazmierczak, F. Dortu, M. J. B. Polo, A. M. Catala, G. M. Kresbach, H. Sohlstrom, T. Moh, L. Vivien, J. Popplewell, G. Roman, C. A. Barrios, G. Stemme, and W. van der Wijngaart, “A packaged optical slot-waveguide ring resonator sensor array for multiplex label-free assays in lab-on-chips,” *Lab on a Chip*, vol. 10, no. 3, pp. 281–290, 2010. 19
- [61] R. G. Heideman and P. V. Lambeck, “Remote opto-chemical sensing with extreme sensitivity: design, fabrication and performance of a pigtailed integrated optical phase-modulated Mach-Zehnder interferometer system,” *Sensors and Actuators B: Chemical*, vol. 61, no. 1-3, pp. 100–127, 1999. 21, 31
- [62] M. I. Lapsley, I. K. Chiang, Y. B. Zheng, X. Y. Ding, X. L. Mao, and T. J. Huang, “A single-layer, planar, optofluidic Mach-Zehnder interferometer for label-free detection,” *Lab on a Chip*, vol. 11, no. 10, pp. 1795–1800, 2011. 21
- [63] A. Ymeti, J. Greve, P. V. Lambeck, T. Wink, S. W. F. M. van Hovell, T. A. M. Beumer, R. R. Wijn, R. G. Heideman, V. Subramaniam, and J. S. Kanger, “Fast, ultrasensitive virus detection using a Young interferometer sensor,” *Nano Letters*, vol. 7, no. 2, pp. 394–397, 2007. 21
- [64] K. E. Zinoviev, A. B. Gonzalez-Guerrero, C. Dominguez, and L. M. Lechuga, “Integrated bimodal waveguide interferometric biosensor for label-free analysis,” *Journal of Lightwave Technology*, vol. 29, no. 13, pp. 1926–1930, 2011. 21
- [65] A. Densmore, M. Vachon, D. X. Xu, S. Janz, R. Ma, Y. H. Li, G. Lopinski, A. Delage, J. Lapointe, C. C. Luebbert, Q. Y. Liu, P. Cheben, and J. H. Schmid, “Silicon photonic wire biosensor array for multiplexed real-time and label-free molecular detection,” *Optics Letters*, vol. 34, no. 23, pp. 3598–3600, 2009. 21

- [66] P. Debackere, S. Scheerlinck, P. Bienstman, and R. Baets, “Surface plasmon interferometer in silicon-on-insulator: novel concept for an integrated biosensor,” *Optics Express*, vol. 14, no. 16, pp. 7063–7072, 2006. 21
- [67] P. Debackere, R. Baets, and P. Bienstman, “Bulk sensing experiments using a surface-plasmon interferometer,” *Optics Letters*, vol. 34, no. 18, pp. 2858–2860, 2009. 21
- [68] J. G. Castello, V. Toccafondo, P. Perez-Millan, N. S. Losilla, J. L. Cruz, M. V. Andres, and J. Garcia-Ruperez, “Real-time and low-cost sensing technique based on photonic bandgap structures,” *Optics Letters*, vol. 36, no. 14, pp. 2707–2709, 2011. 22
- [69] M. R. Lee and P. M. Fauchet, “Nanoscale microcavity sensor for single particle detection,” *Optics Letters*, vol. 32, no. 22, pp. 3284–3286, 2007. 22
- [70] S. Mandal, J. M. Goddard, and D. Erickson, “A multiplexed optofluidic biomolecular sensor for low mass detection,” *Lab on a Chip*, vol. 9, no. 20, pp. 2924–2932, 2009. 22
- [71] S. Pal, E. Guillermain, R. Sriram, B. L. Miller, and P. M. Fauchet, “Silicon photonic crystal nanocavity-coupled waveguides for error-corrected optical biosensing,” *Biosensors and Bioelectronics*, vol. 26, no. 10, pp. 4024–4031, 2011. 22
- [72] A. L. Washburn and R. C. Bailey, “Photonics-on-a-chip: recent advances in integrated waveguides as enabling detection elements for real-world, lab-on-a-chip biosensing applications,” *Analyst*, vol. 136, no. 2, pp. 227–236, 2011. 22
- [73] X. D. Fan and I. M. White, “Optofluidic microsystems for chemical and biological analysis,” *Nature Photonics*, vol. 5, no. 10, pp. 591–597, 2011. 22
- [74] C. Genet and T. W. Ebbesen, “Light in tiny holes,” *Nature*, vol. 445, no. 7123, pp. 39–46, 2007. 24, 73
- [75] J. Weiner, “The physics of light transmission through subwavelength apertures and aperture arrays,” *Reports on Progress in Physics*, vol. 72, no. 6, p. 064401, 2009. 24, 83
- [76] S. Roh, T. Chung, and B. Lee, “Overview of the characteristics of micro- and nano-structured surface plasmon resonance sensors,” *Sensors*, vol. 11, no. 2, pp. 1565–1588, 2011. 24, 32, 74
- [77] K. Mayer and J. Hafner, “Localized surface plasmon resonance sensors,” *Chemical Reviews*, vol. 111, no. 6, pp. 3828–3857, 2011. 24, 32

BIBLIOGRAPHY

- [78] T. W. Ebbesen, H. J. Lezec, H. F. Ghaemi, T. Thio, and P. A. Wolff, "Extraordinary optical transmission through sub-wavelength hole arrays," *Nature*, vol. 391, no. 6668, pp. 667–669, 1998. 24, 73
- [79] F. I. Baida and D. Van Labeke, "Light transmission by subwavelength annular aperture arrays in metallic films," *Optics Communications*, vol. 209, no. 1-3, pp. 17–22, 2002. 24, 73
- [80] R. Gordon, D. Sinton, K. L. Kavanagh, and A. G. Brolo, "A new generation of sensors based on extraordinary optical transmission," *Accounts of Chemical Research*, vol. 41, no. 8, pp. 1049–1057, 2008. 24, 73
- [81] A. G. Brolo, R. Gordon, B. Leathem, and K. L. Kavanagh, "Surface plasmon sensor based on the enhanced light transmission through arrays of nanoholes in gold films," *Langmuir*, vol. 20, no. 12, pp. 4813–4815, 2004. 24, 73
- [82] K. A. Tetz, L. Pang, and Y. Fainman, "High-resolution surface plasmon resonance sensor based on linewidth-optimized nanohole array transmittance," *Optics Letters*, vol. 31, no. 10, pp. 1528–1530, 2006. 24
- [83] L. Pang, G. Hwang, B. Slutsky, and Y. Fainman, "Spectral sensitivity of two-dimensional nanohole array surface plasmon polariton resonance sensor," *Applied Physics Letters*, vol. 91, no. 12, 2007. 24
- [84] J. C. Yang, J. Ji, J. M. Hogle, and D. N. Larson, "Metallic nanohole arrays on fluoropolymer substrates as small label-free real-time bioprobes," *Nano Letters*, vol. 8, no. 9, pp. 2718–2724, 2008. 25, 74
- [85] H. Im, A. Lesuffleur, N. Lindquist, and S.-H. Oh, "Plasmonic nanoholes in a multichannel microarray format for parallel kinetic assays and differential sensing," *Analytical Chemistry*, vol. 81, no. 8, pp. 2854–2859, 2009. 25
- [86] C. Escobedo, A. G. Brolo, R. Gordon, and D. Sinton, "Flow-through vs flow-over: Analysis of transport and binding in nanohole array plasmonic biosensors," *Analytical Chemistry*, vol. 82, no. 24, pp. 10015–10020, 2010. 25, 74
- [87] C. A. Balanis, *Advanced Engineering Electromagnetics*. John Wiley & Sons, Inc., 1989. 25
- [88] M. N. O. Sadiku, *Numerical Techniques in Electromagnetics (Second Edition)*. CRS Press LLC, Boca Raton, 2001. 26
- [89] R. B. P. Bienstmann, L. Vanholme, "CAMFR cavity modelling framework, <http://camfr.sourceforge.net/>." 27

- [90] P. Bienstman and R. Baets, “Optical modelling of photonic crystals and VCSELs using eigenmode expansion and perfectly matched layers,” *Optical and Quantum Electronics*, vol. 33, pp. 327–341, 2001. 27
- [91] K. Yee, “Numerical solution of initial boundary value problems involving Maxwell’s equations in isotropic media,” *IEEE Transactions on Antennas and Propagation*, vol. 14, no. 3, pp. 302 –307, 1966. 28
- [92] A. Taflove and S. C. Hagness, *Computational Electrodynamics: The Finite-Difference Time-Domain Method, Third Edition*. Artech House Publishers, 2005. 28, 29, 74
- [93] T. Weiland, “Time domain electromagnetic field computation with finite difference methods,” *International Journal of Numerical Modelling: Electronic Networks, Devices and Fields*, vol. 9, no. 4, pp. 295–319, 1996. 29, 74
- [94] Website, “<http://www.cst.com/>.” 29, 32
- [95] E. Chow, A. Grot, L. W. Mirkarimi, M. Sigalas, and G. Girolami, “Ultracompact biochemical sensor built with two-dimensional photonic crystal microcavity,” *Optics Letters*, vol. 29, no. 10, pp. 1093–1095, 2004. 31
- [96] J. Dostlek, J. Homola, and M. Miler, “Rich information format surface plasmon resonance biosensor based on array of diffraction gratings,” *Sensors and Actuators B: Chemical*, vol. 107, no. 1, pp. 154 – 161, 2005. 31
- [97] S. Herminjard, L. Sirigu, H. P. Herzig, E. Studemann, A. Crottini, J. P. Pellaux, T. Gresch, M. Fischer, and J. Faist, “Surface plasmon resonance sensor showing enhanced sensitivity for CO₂ detection in the mid-infrared range,” *Optics Express*, vol. 17, no. 1, pp. 293–303, 2009. 31
- [98] K. A. Willets and R. P. Van Duyne, “Localized surface plasmon resonance spectroscopy and sensing,” *Annual Review of Physical Chemistry*, vol. 58, pp. 267–297, 2007. 32
- [99] G. Veronis and S. H. Fan, “Guided subwavelength plasmonic mode supported by a slot in a thin metal film,” *Optics Letters*, vol. 30, no. 24, pp. 3359–3361, 2005. 32, 36, 74
- [100] J. A. Dionne, L. A. Sweatlock, H. A. Atwater, and A. Polman, “Plasmon slot waveguides: Towards chip-scale propagation with subwavelength-scale localization,” *Physical Review B*, vol. 73, no. 3, p. 035407, 2006. 32, 74

BIBLIOGRAPHY

- [101] L. Chen, J. Shakya, and M. Lipson, “Subwavelength confinement in an integrated metal slot waveguide on silicon,” *Optics Letters*, vol. 31, no. 14, pp. 2133–2135, 2006. 32
- [102] C. Delacour, S. Blaize, P. Grosse, J. M. Fedeli, A. Bruyant, R. Salas-Montiel, G. Lerondel, and A. Chelnokov, “Efficient directional coupling between silicon and copper plasmonic nanoslot waveguides: toward metal-oxide-silicon nanophotonics,” *Nano Letters*, vol. 10, no. 8, pp. 2922–2926, 2010. 32
- [103] E. D. Palik and G. Ghosh, *Handbook of Optical Constants of Solids*. Academic press, 1985. 33, 101, 102
- [104] G. Veronis and S. Fan, “Modes of subwavelength plasmonic slot waveguides,” *Journal of Lightwave Technology*, vol. 25, no. 9, pp. 2511–2521, 2007. 36, 44
- [105] R. W. Boyd and J. E. Heebner, “Sensitive disk resonator photonic biosensor,” *Applied Optics*, vol. 40, no. 31, pp. 5742–5747, 2001. 36
- [106] B. E. A. Saleh and M. C. Teich, *Fundamentals of Photonics*. John Wiley & Sons, Inc., 1991. 37
- [107] Q. Cao and P. Lalanne, “Negative role of surface plasmons in the transmission of metallic gratings with very narrow slits,” *Physical Review Letters*, vol. 88, p. 057403, 2002. 55, 73, 84
- [108] A. Pleschinger, J. Lutz, F. Kuchar, H. Noll, and M. Pippan, “Study of polycrystalline and amorphous LPCVD silicon films by atomic force microscopy,” *Surface and Interface Analysis*, vol. 25, no. 7-8, pp. 529–532, 1997. 57
- [109] A. Perentes, I. Utke, B. Dwir, M. Leutenegger, T. Lasser, P. Hoffmann, F. Baida, M. P. Bernal, M. Roussey, J. Salvi, and D. Van Labeke, “Fabrication of arrays of sub-wavelength nano-apertures in an optically thick gold layer on glass slides for optical studies,” *Nanotechnology*, vol. 16, no. 5, pp. S273–S277, 2005. 57
- [110] K. Kurihara, K. Iwadate, H. Namatsu, M. Nagase, H. Takenaka, and K. Murase, “An electron beam nanolithography system and its application to Si nanofabrication,” *Japanese Journal of Applied Physics Part 1-Regular Papers Short Notes & Review Papers*, vol. 34, no. 12B, pp. 6940–6946, 1995. 58
- [111] <http://www.thorlabs.com>. 59
- [112] N. Mortensen, S. Xiao, and J. Pedersen, “Liquid-infiltrated photonic crystals: enhanced light-matter interactions for lab-on-a-chip applications,” *Microfluidics and Nanofluidics*, vol. 4, pp. 117–127, 2008. 62

- [113] H. Y. Zhu, I. M. White, J. D. Suter, P. S. Dale, and X. D. Fan, “Analysis of biomolecule detection with optofluidic ring resonator sensors,” *Optics Express*, vol. 15, no. 15, pp. 9139–9146, 2007. 62
- [114] H. Su and X. G. Huang, “Fresnel-reflection-based fiber sensor for on-line measurement of solute concentration in solutions,” *Sensors and Actuators B: Chemical*, vol. 126, no. 2, pp. 579 – 582, 2007. 64
- [115] H. A. Bethe, “Theory of diffraction by small holes,” *Physical Review*, vol. 66, no. 7/8, pp. 163–182, 1944. 73
- [116] L. Martin-Moreno, F. J. Garcia-Vidal, H. J. Lezec, K. M. Pellerin, T. Thio, J. B. Pendry, and T. W. Ebbesen, “Theory of extraordinary optical transmission through subwavelength hole arrays,” *Physical Review Letters*, vol. 86, no. 6, pp. 1114–1117, 2001. 73
- [117] F. I. Baida, D. Van Labeke, G. Granet, A. Moreau, and A. Belkhir, “Origin of the super-enhanced light transmission through a 2-D metallic annular aperture array: a study of photonic bands,” *Applied Physics B: Lasers and Optics*, vol. 79, no. 1, pp. 1–8, 2004. 73
- [118] Y. Poujet, M. Roussey, J. Salvi, F. I. Baida, D. Van Labeke, A. Perentes, C. Santschi, and P. Hoffmann, “Super-transmission of light through subwavelength annular aperture arrays in metallic films: Spectral analysis and near-field optical images in the visible range,” *Photonics and Nanostructures-Fundamentals and Applications*, vol. 4, no. 1, pp. 47–53, 2006. 73
- [119] Y. Poujet, J. Salvi, and F. I. Baida, “90% extraordinary optical transmission in the visible range through annular aperture metallic arrays,” *Optics Letters*, vol. 32, no. 20, pp. 2942–2944, 2007. 73
- [120] A. G. Brolo, E. Arctander, R. Gordon, B. Leathem, and K. L. Kavanagh, “Nanohole-enhanced Raman scattering,” *Nano Letters*, vol. 4, no. 10, pp. 2015–2018, 2004. 73
- [121] E. H. Barakat, M. P. Bernal, and F. I. Baida, “Second harmonic generation enhancement by use of annular aperture arrays embedded into silver and filled by lithium niobate,” *Optics Express*, vol. 18, no. 7, pp. 6530–6536, 2010. 73
- [122] K. J. K. Koerkamp, S. Enoch, F. B. Segerink, N. F. van Hulst, and L. Kuipers, “Strong influence of hole shape on extraordinary transmission through periodic arrays of subwavelength holes,” *Physical Review Letters*, vol. 92, no. 18, p. 183901, 2004. 73

BIBLIOGRAPHY

- [123] F. J. G. de Abajo, “Colloquium: Light scattering by particle and hole arrays,” *Reviews of Modern Physics*, vol. 79, pp. 1267–1290, Oct. 2007. 73
- [124] U. Schröter and D. Heitmann, “Surface-plasmon-enhanced transmission through metallic gratings,” *Physical Review B*, vol. 58, pp. 15419–15421, Dec 1998. 73
- [125] F. Eftekhari, C. Escobedo, J. Ferreira, X. B. Duan, E. M. Girotto, A. G. Brolo, R. Gordon, and D. Sinton, “Nanoholes as nanochannels: Flow-through plasmonic sensing,” *Analytical Chemistry*, vol. 81, no. 11, pp. 4308–4311, 2009. 74
- [126] A. Yanik, M. Huang, A. Artar, T.-Y. Chang, and H. Altug, “Integrated nanoplasmonic-nanofluidic biosensors with targeted delivery of analytes,” *Applied Physics Letters*, vol. 96, no. 2, p. 021101, 2010. 74
- [127] J. T. Kirk, G. E. Fridley, J. W. Chamberlain, E. D. Christensen, M. Hochberg, and D. M. Ratner, “Multiplexed inkjet functionalization of silicon photonic biosensors,” *Lab on a Chip*, vol. 11, no. 7, pp. 1372–1377, 2011. 74
- [128] R. Gordon and A. G. Brolo, “Increased cut-off wavelength for a subwavelength hole in a real metal,” *Optics Express*, vol. 13, no. 6, pp. 1933–1938, 2005. 77
- [129] Y. Xie, A. Zakharian, J. Moloney, and M. Mansuripur, “Transmission of light through a periodic array of slits in a thick metallic film,” *Optics Express*, vol. 13, no. 12, pp. 4485–4491, 2005. 84
- [130] K. G. Lee and Q.-H. Park, “Coupling of surface plasmon polaritons and light in metallic nanoslits,” *Physical Review Letters*, vol. 95, p. 103902, 2005. 84

Acknowledgements

I would like to express my great gratitude to a group of people, whose supervision, critical discussions, collaboration, and support help me to overcome all the difficulties and accomplish my PhD studies.

First of all, I want to thank my thesis director Professor Hans Peter Herzig, who offered me the opportunity to work in his laboratory. During my study, I have been enjoying the friendly atmosphere and benefiting from various research fields in the lab. Professor Herzig provides me brilliant insights to look into the field of optics.

I want to give my special thanks to the jury members: Professor Pierre-André Farine, Professor Olivier Martin, Doctor Eamonn Murphy, and Professor Wataru Nakagawa, for their critical reviews on my thesis and interesting discussions during the oral exam.

I wish to thank Doctor Matthieu Roussey, for his supervision on the project, for the crucial discussions on work details and life plan, for his complete assistance and encouragement, for all the help he has contributed to me.

Many thanks to Armando Cosentino, who collaborates on the fabrication and characterization part of the project, for his optimism and humor during difficult time.

I would like to thank Professor Wataru Nakagawa and Doctor Vincent Paeder, who guided me to understand the electromagnetic wave theory and offer me help whenever I need.

I appreciate Doctor Eamonn Murphy's help on the correction of my non-scientific English in the thesis and thank him for the pleasant stay in ESTEC of European Space Agency.

I wish to thank my present and former colleagues: Doctor Toralf Scharf, Doctor Pierre-Yves Baroni, Doctor Valeria Musi, Doctor José Dintinger, Doctor Myun-Sik Kim, Yu-Chi Chang, Libo Yu, Marcel Groccia, and others of the group.

I would like to forward my thanks to Joelle Banjac, Brigitte Khan, Mary-Claude Gauteaub, Sandrine Piffaretti for their help on the administrative affairs during my

Acknowledgements

stay in Switzerland.

I also want to express my thanks to my Chinese friends living in Neuchâtel. Great thanks for their friendship and the wonderful time we shared.

Finally, I want to give a big thanks to my family in China for their support on my long term education. Particularly, I want to thank my husband Yazhou. He is always on my side to support and encourage me to conquer problems.

The work is financially supported by Swiss National Science Foundation (SNSF) and the European Space Agency (ESA).

Curriculum vitae

Personal details

First name/Surname	Qing Tan
Gender	Female
Place and date of birth	Hunan China, February 22, 1983
Address	Faubourg de l'Hôpital 56 2000 Neuchâtel Switzerland
Nationality	Chinese
Phone number	+ 41 (0) 78 935 45 37
E-mail	qing.tan@epfl.ch

Education

2008. 02 - 2012	Doctoral thesis work on subwavelength metallic structures for sensing: Modeling & characterization, Optics & Photonics Technology (OPT) Laboratory, Ecole Polytechnique Fédérale de Lausanne (EPFL), Switzerland
2006. 10 - 2008. 01	Master of Science in Micro- and Nano-technology, Institute of Microtechnology (IMT), University of Neuchâtel, Switzerland
2005. 09 - 2006. 09	Graduate program on Microelectronics, College of Information Technical Science, Nankai University, China
2001. 09 - 2005. 06	Bachelor's Degree in Microelectronics, College of Information Technical Science, Nankai University, China

Languages

Chinese :	mother tongue
English :	fluent
French :	basic communication

Interests

Sports : Badminton, skiing and Yoga
Others : traveling, history

Publications in peer review

- P.-Y. Baroni, Q. Tan, V. Paeder, A. Cosentino, M. Roussey, T. Scharf, H. P. Herzig, W. Nakagawa, "Switchable photonic crystal cavity by liquid crystal infiltration," *J. Eur. Opt. Soc.-RP* **5**, 10057 (2010).
- Q. Tan, A. Cosentino, M. Roussey, H. P. Herzig, "Theoretical and experimental study of a 30 nm metallic slot array," *J. Opt. Soc. Am. B* **28**, 1711-1715 (2011).
- Q. Tan, M. Roussey, A. Cosentino, H. P. Herzig, "In-plane illuminated metallic annular aperture array for sensing application," *Opt. Lett.* **37**, 635-637 (2012).

International conferences

- Q. Tan, V. Paeder, A. Cosentino, M. Roussey, W. Nakagawa, H. P. Herzig, "Plasmonic waveguide design for strong field localization," *Fourth International Conference on Surface Plasmon Photonics (SPP4)*, Amsterdam, The Netherlands, 21-26 June 2009, Abstract Book p. 228.
- Q. Tan, V. Paeder, A. Cosentino, M. Roussey, W. Nakagawa, H. P. Herzig, "Field Confinement in Periodic Metallic Slot Waveguide Cavities," *11th International Conference on Near-field Optics, Nanophotonics and Related Techniques*, Beijing, China, 29 August-2 September 2010.
- Q. Tan, M. Roussey, H. P. Herzig, "In-plane Illuminated Metallic Annular Aperture Array for Sensing," *11th International Conference on Near-field Optics, Nanophotonics and Related Techniques*, Beijing, China, 29 August-2 September 2010.
- M. Roussey, Q. Tan, A. Cosentino, H. P. Herzig, "Metallic optical nanostructures: a solution for planar integrated sensors on waveguides," *EOS Topical Meeting on Nanophotonics and Metamaterials*, Paris, France, 26-29 October 2010, **3453**.

- A. Cosentino, Q. Tan, M. Roussey, H. P. Herzig, “Fabrication of slot waveguide cavity for sensing application,” *EOS Topical Meeting on Nanophotonics and Metamaterials*, Paris, France, 26-29 October 2010, **3443-06**.
- M. Roussey, Q. Tan, A. Cosentino, H. P. Herzig, “Planar metallic nanostructures in a waveguide for sensing applications,” *Photonics West*, San Francisco, USA, 22-27 January 2011, **7946-45**.
- A. Cosentino, Q. Tan, M. Roussey, H. P. Herzig, “Planar Integrated Sensors on Waveguides for sensing application,” *the 5th International Conference on Surface Plasmon Photonics 2011 (SPP5)*, Busan, South Korea, 15-20 May 2011.
- Q. Tan, A. Cosentino, M. Roussey, H. P. Herzig, “30nm Metallic Slot Array for Sensing: Theoretical and Experimental Study,” *16th International Conference on Optical MEMS and Nanophotonics (OMN2011)*, Istanbul, Turkey, 8-11 August 2011, Abstract Book p. 27-28.